Maximizing Energy Recovery in Thermoelectric Generator Waste Heat Recovery Systems for Automotive Applications

MAXIMIZING ENERGY RECOVERY IN THERMOELECTRIC GENERATOR WASTE HEAT RECOVERY SYSTEMS FOR AUTOMOTIVE APPLICATIONS

BY

ROMINA RODRIGUEZ, B.Sc., M.Sc.(Mechanical Engineering)

University of California, Berkeley, USA

A THESIS

SUBMITTED TO THE DEPARTMENT OF MECHANICAL ENGINEERING

AND THE SCHOOL OF GRADUATE STUDIES

OF MCMASTER UNIVERSITY

IN PARTIAL FULFILMENT OF THE REQUIREMENTS

FOR THE DEGREE OF

DOCTORATE OF PHILOSOPHY

Doctorate of Philosophy (2019) McMaster University

(Mechanical Engineering) Hamilton, Ontario, Canada

TITLE:	Maximizing Energy Recovery in Thermoelectric Generator Waste Heat Recovery Systems for Automotive Applications
AUTHOR:	Romina Rodriguez B.Sc., M.Sc. (Mechanical Engineering) University of California, Berkeley, USA
SUPERVISOR:	Dr. Ali Emadi & Dr. James S. Cotton
NUMBER OF PAGES:	xxiii, 156

For me

May it be a constant reminder that you can achieve anything you set your mind to.

Abstract

Thermoelectric generators (TEGs) are solid state devices with the ability to convert heat directly to electrical energy. According to the Seebeck effect, if the junctions of a thermoelectric couple are held at a temperature difference, an electromotive force is induced which translates to power generation when an electrical load is connected. Due to their direct energy conversion, small volume, no use of working fluids, and reliability, thermoelectric generators have been investigated for various waste heat recovery applications. Additionally, TEGs can operate in transient environments without drawbacks such as turbo-lag (experienced by other waste heat recovery technologies), which has made TEGs an exceptional candidate for recovery in dynamic waste heat sources such as the exhaust system of a vehicle.

Greenhouse gas (GHG) emissions generated by the transportation sector account for 29% of global emissions, therefore exploring solutions to mitigate this problem is of most importance. Since light duty vehicles and freight trucks make up 78% of the transportation sector, it is crucial to investigate methods by which the efficiency of vehicles can be increased, thereby reducing losses. Although vehicle electrification will make an impact in reducing emissions, it is expected that over 40% of the future vehicle fleet will continue to use an internal combustion engine (ICE). Approximately 40-60% of the total fuel energy is lost through the exhaust system of an ICE vehicle,

therefore, waste heat recovery methods should be investigated, with TEGs having been proven to be a viable technology.

Waste heat recovery (WHR) through the use of TEGs in automotive applications has been investigated since the late 90's. However, the focus of the research has been on optimizing the TEG module for fixed temperature differences to maximize the power output of the module. This steady-state optimization approach has been applied when investigating the power output from a dynamic waste heat environment such as the vehicle exhaust system. When comparing the performance of TEG WHR systems in vehicles, the current metric is maximum power output. TEG WHR systems both modeled and experimentally tested, have been evaluated for the most part at maximum engine load which is not indicative of real driving scenarios. The few studies which have tested the system during real operating conditions such as a vehicle drive cycle, have experimentally achieved lower power than that produced at steady-state.

To further investigate the cause of this degradation in power during transient operation, this thesis developed a transient TEG WHR system model that considers heat capacity in all components. The model was validated at both steady-state and transient operating conditions. The transient model, coupled with a vehicle model that can predict the exhaust temperatures and mass flow rates for various drive cycles, was used to investigate the total energy produced by the system. By investigating the effect that system size has on power generation, it was found that an optimal system size exists since the additional TEG modules in the system degrade the power performance due to heat transfer through the heat exchanger bases. Therefore, the maximum power point does not coincide with the maximum energy design point. In addition to the development of a TEG WHR system design methodology through the

use of the developed models, a maximum power point tracking (MPPT) method was proposed that can achieve a tracking efficiency of 98%, validated through transient experiments. The proposed method can be implemented in current MPPT configurations without the need of additional sensors.

Acknowledgments

I would like to sincerely thank my advisors, Professor Ali Emadi and Professor James S. Cotton. Professor Emadi, thank you for your constant support and for providing me with extensive opportunities to grow both academically and professionally during my time at the McMaster Automotive Resource Centre (MARC). The multidisciplinary research space you have created at MARC has given me the opportunity to become well-versed in both the electrical and mechanical engineering disciplines. Professor Cotton, thank you for your technical feedback and for providing guidance throughout our Thermal Management Research Laboratory (TMRL) meetings. I hope to one day reach your level of intuition and knowledge regarding heat transfer, as well as be able to provide insightful advice regarding research direction. I would also like to thank Professor Chan Y. Ching for all his words of wisdom and encouragement.

To all my colleagues in both TMRL and MARC, who have helped me in one way or another with my graduate studies, thank you. To all the friendships that were created during my time in Canada, thank you for the great memories. I am grateful for all of it.

Finally, I would like to thank my family for their unconditional love. Thank you for allowing me to be myself and for supporting me throughout all my academic endeavors.

Contents

Abstract **iv**

Acknowledgments **vii**

Nomenclature **xx**

1 Introduction **1**

1.1 Motivation 1

1.1.1 Thermal Losses in Vehicles 4

1.2 Waste Heat Recovery Technologies 6

1.2.1 Rankine Cycle 7

1.2.2 Turbocharger 9

1.2.3 6-Stroke Internal Combustion Engine Cycle 10

1.2.4 Thermoelectric Generator 11

1.3 Research Objectives 13

1.3.1 Publications 14

1.4 Thesis Outline 16

2 Thermoelectric Generators **17**

2.1 Thermoelectric Phenomena 17
2.1.1 Seebeck Effect 18
2.1.2 Peltier Effect 19
2.1.3 Thomson Effect 20
2.1.4 Joule Effect 21
2.2 Figure of Merit 22
2.3 TEG Module 24

3 Waste Heat Recovery in Vehicles via TEGs 27

3.1 Motivation 27
3.2 Energy Sources in Vehicles 29
3.3 Thermoelectric Generator Technology 31
3.3.1 Electrical Characteristics 34
3.3.2 Thermal Characteristics 37
3.4 TEG Waste Heat Recovery System 37
3.4.1 Hot Side Heat Exchanger 38
3.4.2 Cold Side Heat Exchanger 40
3.4.3 Power Conditioning Unit 40
3.4.4 Additional Components/Considerations 41
3.5 Experimental Work 42
3.6 Future Trends 46
3.6.1 Advances in TE Materials/Modules 46
3.6.2 Higher System Integration 47
3.6.3 Transient System Design 48
3.6.4 Maximum Energy Recovery 50

4 TEG Modeling **52**

4.1 Literature Review 52

4.1.1 Electro-Thermal Modeling 53

4.2 Module Modeling 58

4.2.1 Validation- TEM Tester 60

4.3 System Modeling– Steady-State 63

4.3.1 Validation–TEG POWER 65

4.3.2 System Size Investigation 74

4.4 System Modeling- Transient Model 79

4.4.1 Model Validation 86

5 Maximum Power Point Tracking for TEGs **90**

5.1 Motivation 90

5.2 Review of MPPT Methods 92

5.3 Maximum Power Point Tracking 95

5.3.1 Proposed MPPT 97

5.3.2 Perturb & Observe 101

5.4 Experimental Validation 102

5.4.1 Electro-Thermal Characterization 102

5.4.2 MPPT Experimental Setup 103

5.5 Experimental Results 105

5.5.1 Steady-State Performance 105

5.5.2 Fast Transient Performance 107

5.5.3 Thermal Transient Performance 108

5.6 Summary 111

6 Vehicle Exhaust Model **113**

6.1 ADVISOR Vehicle Model 113

6.1.1 Vehicle Exhaust Model Verification 116

7 Maximizing TEG Energy Recovery **120**

7.1 Literature Review 120

7.2 Effect on Heat Transfer 121

7.3 Electrical Connection Effects 131

8 Conclusion **133**

List of Figures

1.1 U.S petroleum and other liquid fuels consumption per sector. 2

1.2 Canada petroleum and other liquid fuels consumption per sector. . . 3

1.3 Liquid fuel consumption in 2015 (a) U.S. (b) Canada. 3

1.4 Fuel losses in ICE vehicle (values from California Energy Commission). 5

1.5 Exhaust thermal power available for a 90kW engine over a UDDS drive cycle. 6

1.6 Rankine cycle with pre-heat configuration. 7

1.7 Turbocharger configuration with ICE. 9

1.8 (a) Schematic of pressure vs. volume for a 4-stroke engine cycle. (b) Schematic of pressure vs. volume for a 6-stroke engine cycle. 11

1.9 Schematic of thermoelectric generator module sandwiched between heat exchangers. 12

2.1 (a) Schematic of thermoelectric couple, one side is maintained at T_H and the other is at T_C (b) thermocouple behaving as a generator (c) thermocouple behaving as a cooler. 18

2.2 (a) Seebeck coefficient and (b) Thermal conductivity as a function of temperature [34]. 23

2.3 ZT of typical thermoelectric materials over time [34]. 24

2.4 (a) Thermocouple schematic (b) many thermocouples form a TEG module 25
3.1 ZT as a function of temperature for various TE materials (A. p-type PbTe endotaxially nanostructured with SrTe [54]),(B. Skutterudite $Co_{23.4}Sb_{69.1}Si_{1.5}Te_{6.0}$ [55]),(C. p-type FeNbSb half-Heusler [56]), (D. p-type polycrystalline $Sn_{.95}Se$ [57]). 32
3.2 (a) off-the-shelf flat TEG module (b) cylindrical TEG module concept [63]. 34
3.3 (a) Heat flows in electro-thermal TEG equivalent circuit (b) Electrical circuit. 35
3.4 Characterization of an off-the-shelf TEG module from TECTEG MFR. T_C is 35°C. 36
3.5 Schematic of TEG WHR system and thermal resistances in system. . 38
4.1 TEG WHR system. 53
4.2 TEG WHR thermal system model schematic. 54
4.3 Heat flows in electro-thermal TEG equivalent circuit including resistances of heat sinks. 55
4.4 P-N schematic and equivalent thermal circuit 58
4.5 Schematic of experimental setup for electro-thermal characterization (not drawn-to-scale). 61
4.6 Comparison of experimental results for V-I curve to prediction by module model for varying T_H with a fixed T_C=35°C. 63
4.7 (a) Schematic of typical TEG WHR system layout (b) Equivalent thermal network model for TEG WHR system. 64

4.8 (a) TEG POWER system installed on pizza oven (b) modular unit of TEG POWER system. (c) top view of TEG POWER unit 66
4.9 Electrical configuration of TEG POWER. Row 1 and Row 2 are connected in series and are then connected in parallel to the symmetric bottom part of TEGs. 67
4.10 Node network for TEG POWER system 67
4.11 Flow chart for steady-state thermal model solution scheme. 70
4.12 Steady-State power output model prediction compared to experimental power measured as function of exhaust mass flow rate. 71
4.13 Steady-state model prediction of TEG temperature, T_H and T_C, compared to experimental results. 72
4.14 Steady-state model prediction of Hot HEX exhaust exit temperature compared to experimental results. 73
4.15 Steady-state model prediction of Cold HEX coolant exit temperature compared to experimental results. 73
4.16 The power output by a TEG WHR system as more TEG modules are added in the direction of exhaust flow (x-direction) and perpendicular to the exhaust inlet (z-direction). 75
4.17 The specific power of each TEG module as more TEG modules are added to the system. 76
4.18 A degradation in power output is observed as more units are added to the system in the direction perpendicular to exhaust flow. 77

4.19 Comparison of power output: 1) Reference case with single MPPT for all rows, 2) MPPT is added per row, 3) axial conduction is turned-off 4) both axial conduction is off and an MPPT is added per row. . . . 78
4.20 Schematic of nodalization in TEG WHR system for transient analysis. 80
4.21 Transient model flow diagram explaining how solution is solved. . . . 85
4.22 Experimental data of the exhaust gases and exhaust temperature at inlet of hot side HEX during the NRTC drive cycle. 87
4.23 Test section for transient tests conducted on engine. The TEG modules are sandwiched between a hot side HEX and two cold side HEXs. . . 87
4.24 Comparison of experimental data from [103] compared to the developed model of the TEG module. 88
4.25 Nodalization of TEG WHR system model for validation in engine environment. 89
4.26 The error is reported as the absolute difference between the simulation and the experimental data, as can be observed the error is less than 1W. 89
5.1 TEG MPPT configuration. 96
5.2 High Frequency Injection MPPT scheme. 97
5.3 Perturb & Observe MPPT algorithm. 101
5.4 Experimental electrical characterization of commercial TEG module for T_C=35°C. 102
5.5 TEG power output model results for various T_H with T_C=35°C. . . . 103
5.6 MPPT experimental setup. 104

5.7 Steady-State performance from Table 5.3 represented in graphical form. (a) Voltage error (%) (b) Power error (%) for various temperature differences (ΔT) (c) Comparison of tracking efficiency for the P&O scheme and HFI scheme. 108
5.8 Transient Evaluation: TEG output voltage changes from V_{oc} to $V_{oc}/2$ when HFI MPPT scheme is turned on. Response time is 2.4ms. . . . 109
5.9 Thermal transient: (a) Scope screenshot of TEG voltage and current measurement during HFI tracking (b) Comparison of expected power output as a function of temperature difference (ΔT) of the TEG module versus HFI MPPT power. 110
5.10 Thermal transient: (a) Scope screenshot of TEG voltage and current measurement during P&O tracking (b) Comparison of expected power output as a function of temperature difference (ΔT) of the TEG module versus P&O MPPT power. 111
6.1 Exhaust temperature distribution for a 100kW SI engine [44]. 114
6.2 Vehicle speed over a UDDS drive cycle. 114
6.3 Exhaust gas temperature and mass flow rate over a UDDS drive cycle. 115
6.4 Vehicle speed over time for a US06 drive cycle. 116
6.5 Exhaust gas temperature and mass flow rate over a US06 drive cycle. 117
6.6 Comparison of exhaust temperature at exit of three-way catalytic converter predicted by vehicle model to experimental data from [58] over an NEDC drive cycle. 118
6.7 Comparison of exhaust mass flow rate predicted by vehicle model to experimental data from [58] over an NEDC drive cycle. 118

7.1 Overview of transient model to investigate power output over various drive cycles. 122
7.2 Power output of a TEG WHR system with 48 TEGs over a UDDS drive cycle. 123
7.3 Power output comparison of a TEG WHR system of two sizes: 48 TEG modules and 24 TEG modules. 124
7.4 Comparison of the TEG hot side temperature of the first row of TEG modules in two systems. 125
7.5 Temperature distribution of exhaust and TEG hot side for 1 and 2 Row system. 126
7.6 Total energy recovered over a UDDS drive cycle vs. the total number of TEG modules in a system. 127
7.7 Total energy recovered over a US06 drive cycle vs. the total number of TEG modules in a system. 128
7.8 TEG WHR modular unit, as the system size gets bigger TEG modules are added either (a) perpendicular to exhaust flow 'Column' or (b) in the direction of exhaust flow 'Rows'. 128
7.9 Total energy recovered and peak power output when the number of columns is fixed to 2 and 3 modular units, and the additional units are added only in the direction of exhaust flow. 129
7.10 Total energy recovered over a US06 drive cycle vs. the total number of TEG modules in a system. 130
7.11 Power output comparison utilizing Half-Heusler modules vs. Bismuth Telluride modules over two drive cycles. 131

7.12 The power output for 72 TEGs consisting of 3 TEG rows with a single MPPT and each row containing its own MPPT. 132

List of Tables

3.1 Approximate fluid temperatures of heat source 30

3.2 Approximate fluid mass flow rates of heat source 31

3.3 TEG module characterized properties 36

3.4 Experimental TEG WHR system power output reported in the literature 44

4.1 Boundary conditions for TEG WHR system model and comparison of model results to experimental data. 74

5.1 TEG module parameters 103

5.2 Converter efficiency. 104

5.3 Steady-state results: (1) Characterization results for various temperature differences, (2) Experimental MPPT Results for both schemes: V_{MP}, Voltage at max power (MP), P_{MP} power output at MP (3) MPPT performance error compared to characterization. 106

7.1 Review of transient models found in the literature. 121

Nomenclature

Symbols

A	cross-sectional area, m^2
B	amplitude
D	duty cycle
f	frequency, Hz
h	heat transfer coefficient, W/m^2-K
I	current, A
K	thermal conductance, W/K
k	thermal conductivity, W/m-K
L	length, m
M	mass, kg
P	electrical power, W
Q	heat rate, W
R	electrical resistance, Ω
T	temperature, K

V voltage, V

Greek Symbols

α Seebeck coefficient, V/K

Δ difference

η efficiency, %

Ω electrical resistance, ohm

ω angular frequency, rad/s

π Peltier coefficient, W/A

τ Thomson coefficient, V/K

N number of TEG modules

n number of TE couples

Abbreviations

BCs Boundary Conditions

BTU British thermal unit

CA Crank Angle

CC Catalytic Converter

CV Control Volume

EGR Exhaust Gas Recirculation

EIA U.S. Energy Information Agency

FTTP Full-Throttle Pedal Position

HEX Heat Exchanger

HFI High Frequency Injection

ICE Internal Combustion Engine

MP Maximum Power

MPPT Maximum Power Point Tracking

NEDC New European Driving Cycle

ORC Organic Rankine Cycle

P&O Perturb & Observe

SI Spark-ignition

TCC Three-Way Catalytic Converter

TE Thermoelectric

TEG Thermoelectric Generator

UDDS Urban Dynamometer Driving Schedule

WHR Waste Heat Recovery

Subscripts

C cold side

cer ceramic

ct contact

ctr contactor

e exhaust

f	fin
H	hot side
int	internal
l	load
max	maximum
o	out
oc	open circuit
sw	switching
TE	thermoelectric couple
w	coolant

Chapter 1

Introduction

1.1 Motivation

Due to society's dependence on fossil fuels, a limited source of energy, engineers must continually work on improving the efficiency of technologies which are powered by them. Increasing a system's efficiency equates to having the same or greater work output for a smaller input. According to the U.S. Energy Information Agency (EIA), in 2015 the U.S. consumed 27.1 quadrillion BTU of petroleum and other liquid fuels [1]. Other liquid fuels refers to natural gas plant liquids (NGPL), biofuels, gas-to-liquids (GTL), coal-to-liquids (CTL), and oil shale [2]. Meanwhile, Canada consumed 2.3 quadrillion BTU of petroleum and other liquid fuels in 2015, a number comparable to the U.S. considering fuel consumption per capita (84.4 million BTU/person in the U.S. and 64.4 million BTU/person in Canada). It is estimated that in 2050 the consumption of petroleum by all energy-consuming sectors will be similar to today in both the U.S. and Canada, as shown in Figure 1.1 and Figure 1.2, respectively.

The transportation sector is the greatest consumer of fuel both in the U.S. and

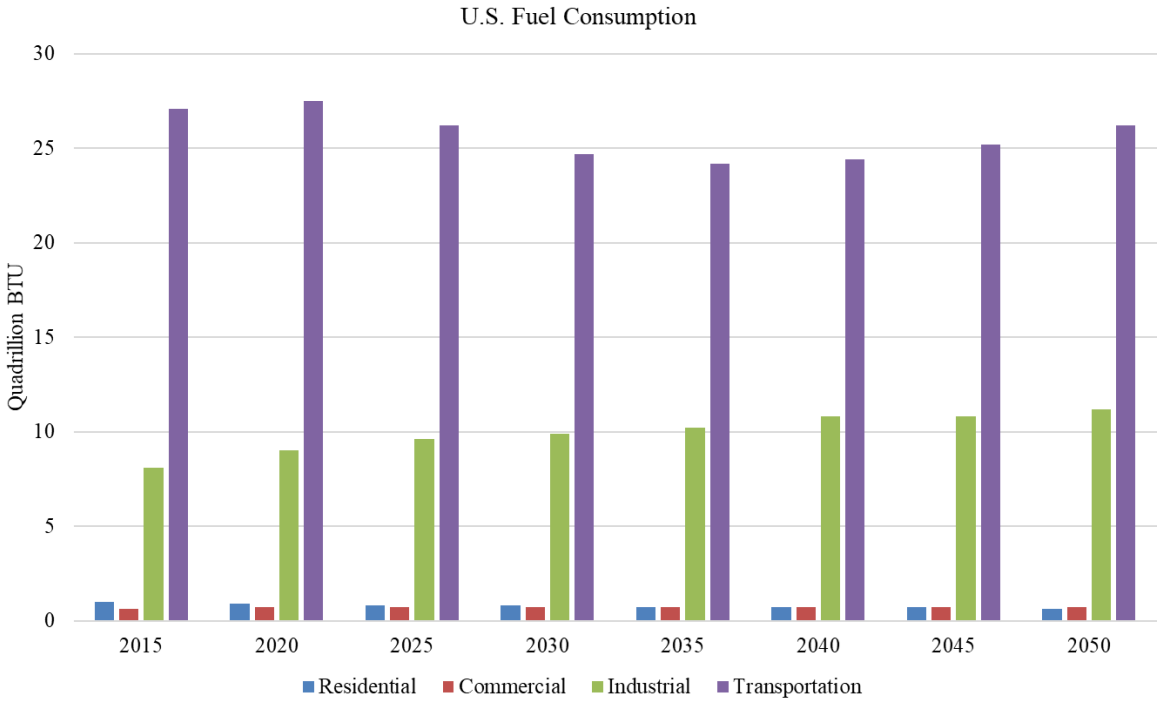

Figure 1.1: U.S petroleum and other liquid fuels consumption per sector.

Canada as observed in Figure 1.3. The U.S. EIA predicts that fuel consumption by the transportation sector will be reduced by only 3-4% in 2050 compared to 2015. Not only is this alarming from a limited-resource point-of-view, but also because the burning of fossil fuels results in greenhouse gases which contribute to climate change. Since the transportation sector has the most overwhelming contribution to fuel consumption, mitigating this problem through energy efficiency efforts should be of foremost importance.

Light duty vehicles make up 55% of the total energy use in the transportation section while commercial and freight trucks make up 23% [3]; thus if the overall efficiency of vehicles is increased, a reduction in the total global fuel consumption could be achieved. Although vehicle electrification may mitigate the fuel consumption problem, many hurdles remain before widespread electric vehicle dissemination. In 2016

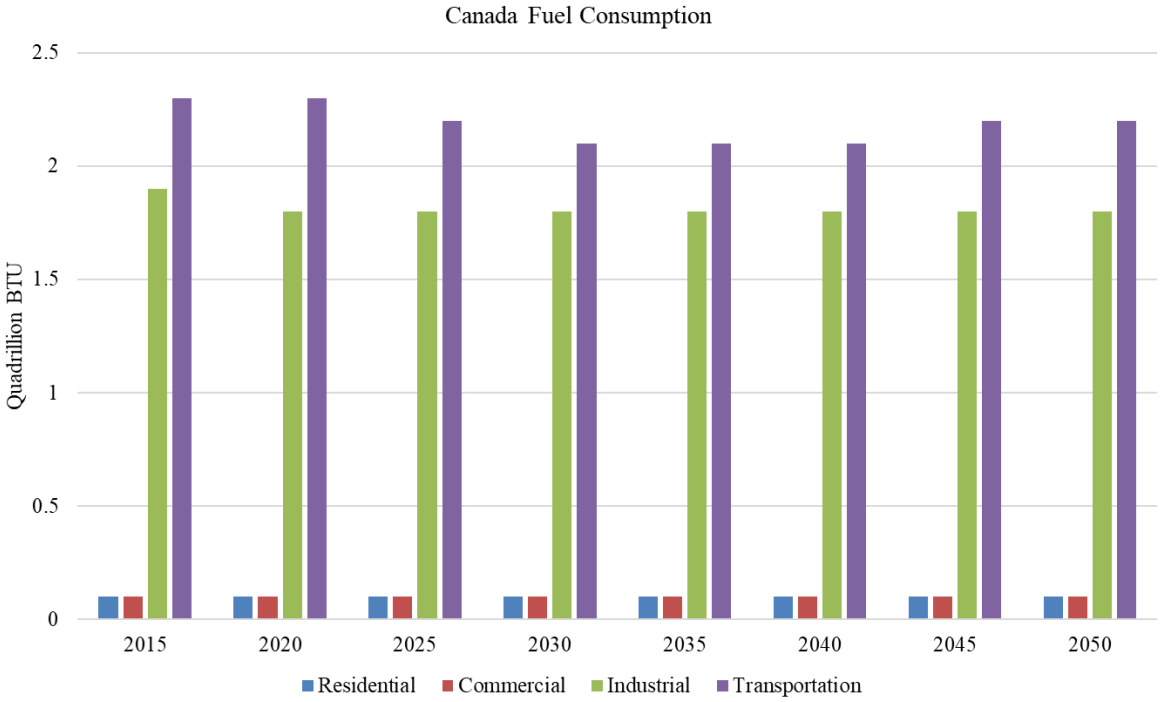

Figure 1.2: Canada petroleum and other liquid fuels consumption per sector.

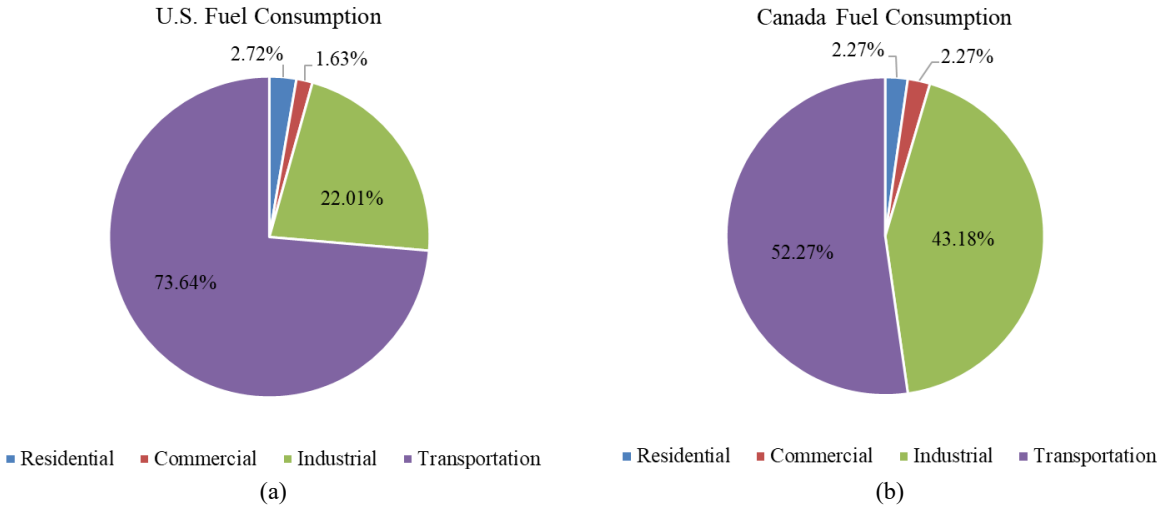

Figure 1.3: Liquid fuel consumption in 2015 (a) U.S. (b) Canada.

only 0.2% of the world's passenger vehicle fleet was electrified. However, Bloomberg New Energy Finance predicts that 33% of the vehicle fleet will be electric by 2040 [4] and the IEA greenhouse gas limitations recommends 60% of all vehicles to be electrified by 2060 to meet the Paris Agreement goal (maintain global temperature 2°C below pre-industrial levels). Electric vehicles (EV) include battery-electric vehicles (BEVs), plug-in hybrid vehicles (PHEVs) and fuel cell vehicles (FCEVs), which means that a fraction of these EVs will continue to include an internal combustion engine (ICE). Therefore, even though electrification will reduce the use of ICE's, 40% of the future vehicle fleet (this number may be larger as there is no implemented policy that mandates the electrification of vehicles worldwide) will operate only with ICE's and also a percentage of the 60% of electrified vehicles will include an ICE (such as PHEVs).

1.1.1 Thermal Losses in Vehicles

A concern with a large majority of the future vehicle fleet consisting of ICE's is their low tank-to-wheel efficiency. To better understand fuel efficiency in a vehicle, the loss distribution within an ICE vehicle is depicted in Figure 1.4. Only about 10-15% of the fuel energy goes into driving the vehicle while the rest is lost through different processes. ICE vehicles include both spark-ignition (SI) and diesel engines. Approximately 17-26% and 16-35% of the fuel energy is lost to the engine coolant for SI engines and diesel engines, respectively. While 34-45% and 22-35% of the fuel energy is lost to the exhaust gases for SI engines and diesel engines, respectively, at maximum power [5]. The magnitude of the thermal losses depend on the engine size and the driving conditions. As observed, the largest portion of fuel energy in a vehicle

is lost as thermal energy (heat) in the exhaust gases of an SI ICE. It is therefore of interest to investigate how to recover energy found in the exhaust system of cars. If this thermal energy could be converted to useful energy such as electricity for the vehicle, then the total amount of fuel consumed by the vehicle can be reduced, thus increasing the system efficiency.

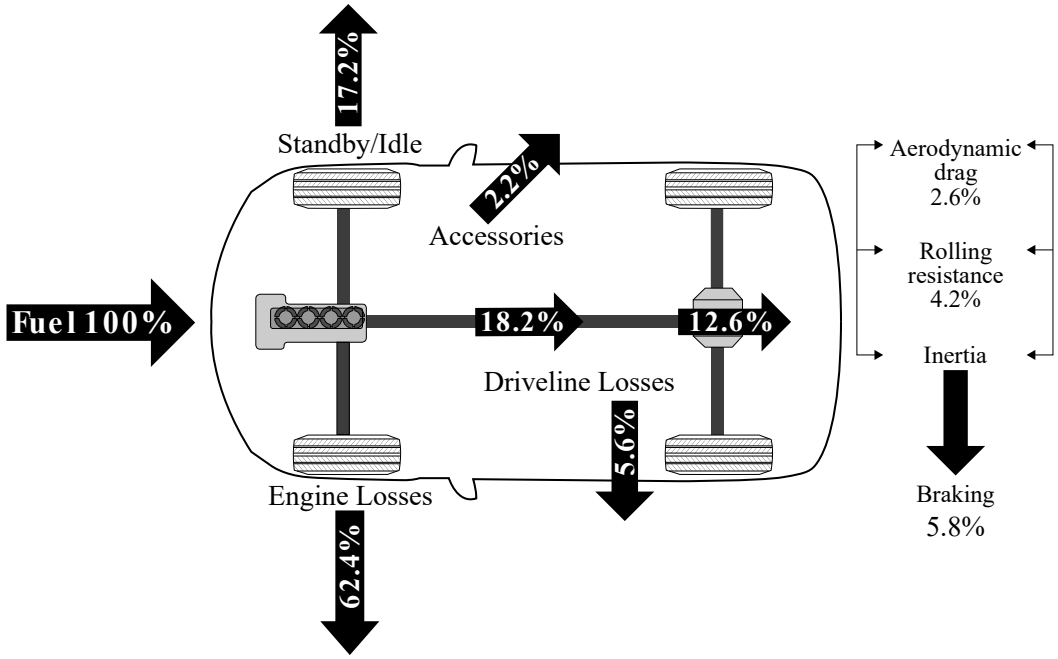

Figure 1.4: Fuel losses in ICE vehicle (values from California Energy Commission).

A particular challenge to recovering thermal energy from the exhaust system of a vehicle is that the losses are constantly changing during operation of the vehicle. The rate of energy, Q, available for recovery depends on the exhaust gases' temperature (T_{exh}) and mass flow rate ($\dot{m}_{exh}$) and can be calculated as

$$Q = \dot{m} Cp \left(T_{exh} - T_{ref}\right) \tag{1.1}$$

where C_P is the specific heat of the exhaust gases. The exhaust power available for

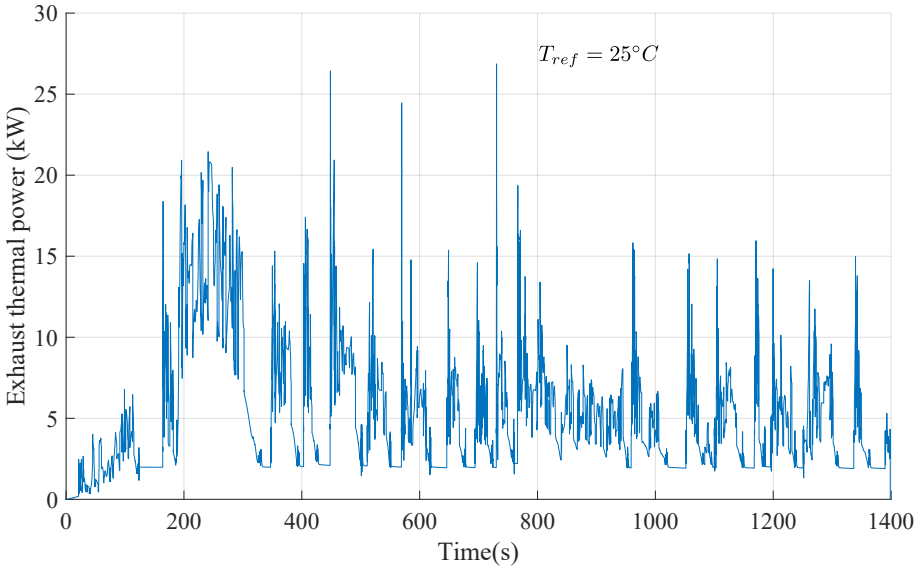

Figure 1.5: Exhaust thermal power available for a 90kW engine over a UDDS drive cycle.

recovery for a 90kW gasoline engine during a UDDS drive cycle is shown in Figure 1.5. As can be observed from the dynamic power available, a technology needs to be implemented that can adapt to the variable operating conditions of the exhaust gases.

1.2 Waste Heat Recovery Technologies

Waste heat recovery (WHR) is a method by which energy that would end up in the environment in the form of heat is recovered, and converted to useful energy such as electrical energy. Currently, there are several different technologies being investigated for WHR that utilize the exhaust gases of ICE vehicles. Much research has gone into understanding the feasibility and proposing system designs for each proposed technology. The following sections provide a general overview of the top candidates for WHR in automotive applications. In particular, the Rankine cycle,

turbocharger, 6-stroke ICE cycle, and thermoelectric generator are discussed.

1.2.1 Rankine Cycle

A Rankine cycle is a thermodynamic process that describes the conversion of steam energy to mechanical work. A typical Rankine cycle with pre-heat configuration for waste heat recovery in ICE is shown in Figure 1.6. The working fluid is pumped from process 1-2 to increase its pressure and is then pre-heated by the engine-coolant (process 2-3). The fluid then enters the evaporator from process 3-4 where it absorbs energy from the exhaust gases and is converted to saturated vapor. In process 4-5, the fluid enters the expander and power is generated. The lower temperature and pressure fluid now enters the condenser in process 5-1 to start the cycle once again.

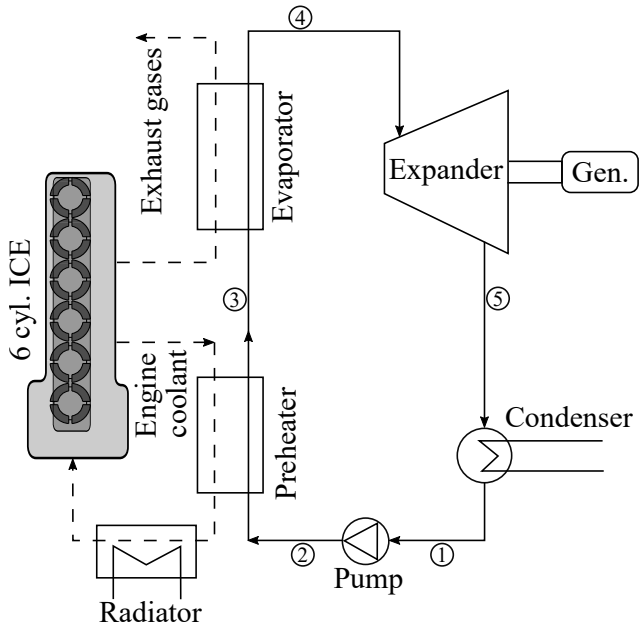

Figure 1.6: Rankine cycle with pre-heat configuration.

Due to the medium-grade energy available in the exhaust gases of an ICE, organic fluids have mostly been investigated for WHR. The fluids are referred to as organic

due to their organic nature and their ability to change phase from liquid to vapor at a lower temperature compared to water. Selecting the appropriate working fluid in the design of Organic Rankine Cycles (ORC) is crucial to achieve optimal heat transfer at the expected operating conditions. The expander, which generates power, is also important when sizing the system and typically turbines are chosen for engines with 1MW power output and volumetric expanders are selected for engines with power outputs of less than 100kW [6]. Both the selection of the working fluid and the expander technology has a significant effect on the efficiency of the system [7].

Implementing ORC into the exhaust system has the potential of improving a vehicle's fuel economy by $\sim$10% through the use of modern refrigerants and advanced expanders [8]. However, there are a few disadvantages to implementing these systems for WHR in a vehicle. ORC systems are bulky due to the number of components required for the cycle and their installation in the exhaust system of a vehicle would add packaging complexity. Another technical issue is concerning transient operating of ORC systems in dynamic environments. The engine undergoes transient operation in real driving conditions and hence the available thermal energy or operating conditions for the ORC change frequently with time, making transient operation difficult [9]. In general, ORC waste heat recovery systems are inherently highly dynamic and require multiple coupled actuators [10]. For example, the evaporator pressure is affected by the pump and the expander inlet and bypass valves; hence the actuator position will have an impact on the operation. Also, the mass flow rate of the working fluid is typically used to control the vapor temperature at the outlet of the evaporator (uses waste heat from engine). When the mass flow rate is adjusted by the pump, the evaporator pressure will change and hence, the expander inlet and bypass valves need to

respond appropriately to control the evaporation pressure. Therefore, ORC systems require many additional components and actuators that are difficult to control and even more so in a system where the operating conditions are frequently changing.

1.2.2 Turbocharger

Turbochargers force additional air into the engine cylinder and consequently more fuel into the combustion chamber to increase the engine's power output and volumetric efficiency. The hot exhaust gases exiting the engine exhaust port will drive the turbine of the turbocharger and in turn, the compressor side will draw in ambient air. Since the air is being compressed by the turbocharger, a charge air-cooler is needed to cool the gases before they enter the engine intake port. A typical configuration of a turbocharger for an SI ICE is shown in Figure 1.7. Today, turbochargers are widely implemented with diesel engines due to the increase in fuel efficiency.

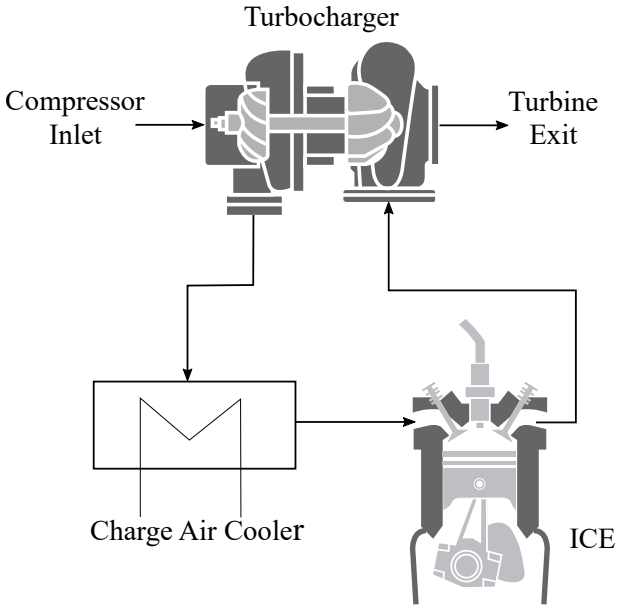

Figure 1.7: Turbocharger configuration with ICE.

Turbochargers, however are subject to turbo-lag (delayed transient response) during low speed acceleration [11]. Also exhaust backpressure is an issue at low engine speeds, which increases the pumping power of the engine [12]. In general turbomachinery suffers from turbo-lag and therefore, variable geometry turbochargers are being thoroughly investigated for potential engine downsizing and better operation under variable operating conditions [13].

1.2.3 6-Stroke Internal Combustion Engine Cycle

Another possible technology for WHR in vehicles is the six-stroke internal combustion engine cycle. The typical four-stroke combustion engine cycle consists of an 1) intake stroke, 2) compression stroke, 3) combustion stroke and 4) exhaust stroke. The six-stroke cycle adds two additional strokes to increase the work extracted from the fuel energy and to reduce emissions [11]. The additional two strokes involve trapping and compressing a portion of the exhaust gases from the exhaust stroke (4th stroke) as proposed by Conklin et al. [14]. Then, water is injected (pre-heated by engine coolant) and direct heat transfer occurs between the residual exhaust gases and water resulting in the liquid vaporization (pressure increase), thus resulting in another expansion stroke (5th stroke). After the exhaust-steam mixture expands, the cylinder piston moves up again for the final exhaust stroke (6th stroke). The additional two-strokes produce more power than a conventional engine, which can be seen in the pressure vs. cylinder volume curves for a 6-stroke engine in Figure 1.8 (b) compared to a 4-stroke engine in Figure 1.8 (a).

Many researchers have proposed variations or modifications to the six-stroke engine in patents [15–20]. However, the majority proposed a complete exhaust stroke

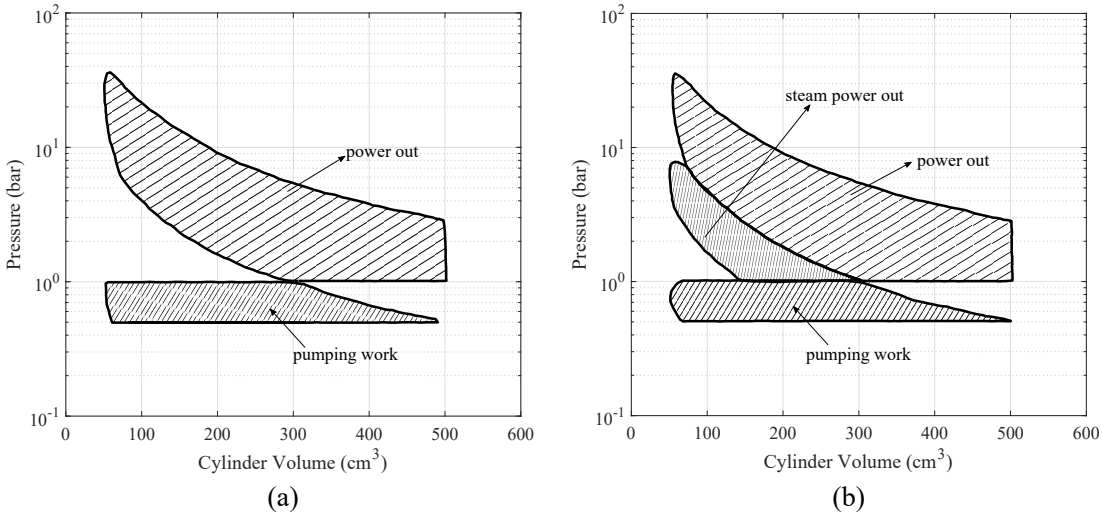

Figure 1.8: (a) Schematic of pressure vs. volume for a 4-stroke engine cycle. (b) Schematic of pressure vs. volume for a 6-stroke engine cycle.

before water is injected and therefore, impingement occurs at the combustion chamber walls (location of heat transfer). Conklin et al. [14] proposed a more efficient cycle by injecting water at 720 crank angle (CA), thus mixing the water directly with the exhaust gases and using the waste heat to vaporize the fluid rather than the cylinder surfaces. The modeling results of [14] show a 7.5%-25% potential increase in mean effective pressure (MEP) compared to the conventional 4-stroke engine as a result of the steam stroke. Even so, significant research is required to implement modifications to the exhaust valve timing to include the water injection at the specified CA, as well as integration of water injection mechanism.

1.2.4 Thermoelectric Generator

Thermoelectric generators (TEGs) are solid-state devices that convert heat directly to electrical energy. TEGs operate due to the Seebeck effect, which was observed

when two dissimilar conductors were connected and an electromotive force (emf) was generated. This effect occurred because one junction was maintained at a certain temperature while the other junction of the conductors was held at a different temperature. Today, TEGs are made of semiconductor materials rather than conductors due to the higher emf's generated. A temperature difference needs to be imposed on the TEG to produce a voltage potential and when an electrical load is connected, current is allowed to flow, thus generating power.

Many positively-doped and negatively-doped semiconductors are connected electrically in series to form a TEG *module*. A temperature difference is created across the module through the utilization of a hot-side heat exchanger and a cold-side heat exchanger. An electrical load is connected to the system to generate power as observed in Figure 1.9. In WHR applications for vehicles, the hot-side heat exchanger extracts energy from the hot exhaust gases and the cold-side heat exchanger typically uses the engine coolant.

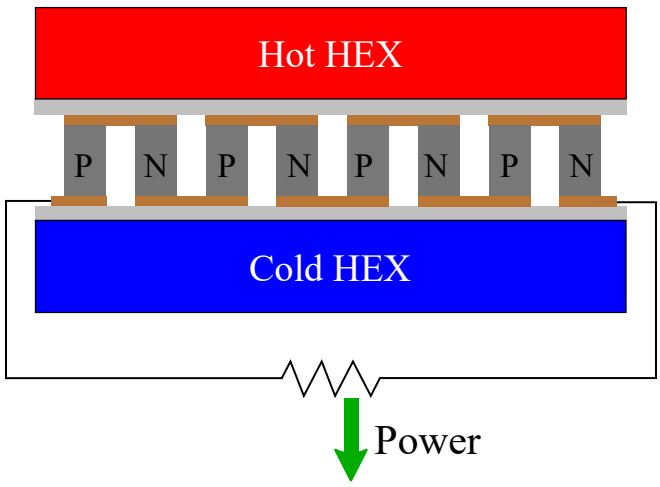

Figure 1.9: Schematic of thermoelectric generator module sandwiched between heat exchangers.

Although TEGs have the disadvantage of low energy conversion efficiency, they compensate by having several advantages. TEGs are capable of directly converting heat to electricity without any working fluids or moving parts. Therefore, they also operate quietly [21]. TEGs are small in volume and hence they would not take up a lot of space like ORC systems in vehicles. Minimum to no maintenance is required during the operation of TEGs and they are highly reliable. Finally, the greatest advantage is their ability to operate in transient conditions unlike the other aforementioned WHR technologies. Due to these advantages, specially TEGs' ability to operate in transient operation (the TEGs' electrical response is almost instantaneous [22, 23]), thermoelectric generators have been selected as the waste heat recovery technology to investigate in this work.

1.3 Research Objectives

Although much research has been undertaken in investigating thermoelectric generators as a feasible technology for WHR in the exhaust system of vehicles, several gaps can be identified in the literature. In particular, the majority of the research undertaken has been in the design of the WHR system to maximize the power under steady-state conditions. Maximum power output as a performance metric in TEG systems is explained in detail in Chapter 3. However, the operation of a vehicle is transient and the available energy for recovery changes with time and constantly.

Therefore, this thesis has taken a further look at WHR system design utilizing TEGs such that maximum energy is recovered, i.e. the integral of power with time, rather than optimizing for the instantaneous maximum power produced. In doing so, several effects are investigated such as 1) maximum power vs. maximum energy

recovered 2) utilizing high temperature TEG materials 3) maximum power point tracking efficiency and 4) trade-offs between the energy gains and system losses. In particular, the thesis attempts to tackle the following objectives:

1. Develop a transient electro-thermal model of the complete TEG WHR system
2. Investigate the effect of system size on the peak power generated by the TEG WHR system
3. Investigate the peak power output vs. total energy recovered for vehicle drive cycles
4. Development of a maximum power point tracking method that achieves a higher tracking efficiency compared to conventional tracking methods
5. Develop a design methodology for sizing TEG WHR systems for maximum energy recovery

1.3.1 Publications

During the time spent working on the thesis, I was also involved in other research projects that dealt with thermal management of power electronics. Below is a list of all the published journal papers and conferences as a result of my work during the PhD:

[J1] R. Rodriguez, J. Guo, M. Preindl, J. S. Cotton, and A. Emadi, "High frequency injection maximum power point tracking for thermoelectric generators," *Energy Conversion and Management*, vol. 198, pp. 1-9, October 2019. doi: 10.1016/j.enconman.2019.111832

[J2] R. Rodriguez, M. Preindl, J. S. Cotton and A. Emadi, "Review and Trends of Thermoelectric Generator Heat Recovery in Automotive Applications," in *IEEE Transactions on Vehicular Technology*, vol. 68, no. 6, pp. 5366-5378, June 2019. doi: 10.1109/TVT.2019.2908150

[J3] P. Azer, R. Rodriguez, J. Guo, J. Gareau, J. Bauman, B. Bilgin, and A. Emadi, "Time Efficient Integrated Electro-Thermal Model for a 60 kW 3-Phase Bidirectional Synchronous DC-DC Converter" in *IEEE Transactions on Industry Applications* doi:10.1109/TIA.2019.2948804

[J4] B. Bilgin, J. Liang, M.V. Terzic, J. Dong, R. Rodriguez, E. Trickett, and A. Emadi, "Modeling and Analysis of Electric Motors: State-of-the-Art Review," in *IEEE Transactions on Transportation Electrification.* doi: 10.1109/TTE.2019.2931123

[C1] R. Rodriguez, A. Emadi and J. Cotton, "Maximum power point tracking for thermoelectric generators with high frequency injection," IECON 2015 - 41st Annual Conference of the IEEE Industrial Electronics Society, Yokohama, 2015, pp. 004127-004132. doi: 10.1109/IECON.2015.7392744

[C2] R. Rodriguez, A. Emadi and J. Cotton, "Designing a Thermoelectric Generator Waste Heat Recovery System for Maximum Energy Recovery" in *International Conference on Thermoelectrics (ICT) 2019*, Gyeongju, Korea, July 2019.

[C3] R. Rodriguez, M. Alizadeh, J. Bauman, P. S. Ravi and A. Emadi, "Performance Evaluation of Thermal Management for a 3-Phase Interleaved DC-DC Boost Converter," *2018 IEEE Transportation Electrification Conference and Expo (ITEC)*, Long Beach, CA, 2018, pp. 488-493.

[C4] P. Azer, R. Rodriguez, H. Ge, J. Bauman, P. S. Ravi and A. Emadi, "Time

Efficient Integrated Electro-Thermal Model for Bidirectional Synchronous DC-DC Converter in Hybrid Electric Vehicles," *2018 IEEE Transportation Electrification Conference and Expo (ITEC)*, Long Beach, CA, 2018, pp. 55-62.

1.4 Thesis Outline

The thesis consists of eight chapters including the introduction chapter. The introduction chapter provides the motivation behind waste heat recovery in vehicles by showing that the transportation sector accounts for the greatest consumption of fossil fuels. If the efficiency of automotive vehicles can be increased, then a total fuel consumption reduction would result. Next, the working principles of thermoelectric generators is presented in Chapter 2 and a complete literature review on waste heat recovery via TEGs in automotive applications is presented in Chapter 3.

The modeling method for TEGs from the module level up to the system level is presented in Chapter 4. Experimental validations are presented for both the steady-state and transient models. Chapter 5 presents a new maximum power point tracking scheme and shows the experimental results which validate the technique as well as report the achieved efficiency. Since the exhaust system of a vehicle is the source of waste heat, Chapter 6 presents the vehicle modeling as well as a study of the thermal losses in a car depending on the type of ICE. The developed WHR TEG system model is used to investigate several effects to maximize the energy recovered by the system and design suggestions are presented in Chapter 7. Finally, Chapter 8 concludes the thesis by presenting a general overview of the thesis as well as the recommended future work for this research area.

Chapter 2

Thermoelectric Generators

2.1 Thermoelectric Phenomena

A potential technology for recovering waste heat in the exhaust system of a vehicle is a thermoelectric generator (TEG). Thermoelectrics are solid state devices that are capable of converting thermal energy, in the form of a temperature difference, directly to electricity and vice versa. If heat is converted to electricity then the thermoelectric device is considered a *generator* and if power is consumed by the thermoelectric to pump heat, then it's considered a *cooler*. A negative-doped (n-type) semiconductor is connected via a metal contactor to a positive-doped (p-type) semiconductor to create a thermoelectric (TE) junction, thus forming a p-n thermocouple as shown in Figure 2.1 (a)- the basis of a thermoelectric device. Imposing a temperature difference results in one side of the thermocouple being referred to as the hot side, T_H, and the opposite side as the cold side, T_C. The imposed temperature difference (ΔT) will result in a measurable electromotive force. Thermoelectric energy conversion exhibits three thermoelectric effects: the Seebeck, Peltier and Thomson effect.

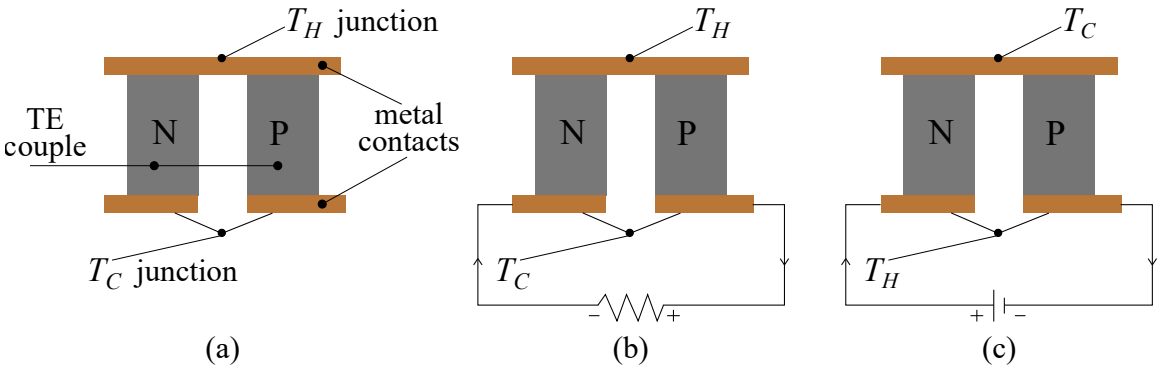

Figure 2.1: (a) Schematic of thermoelectric couple, one side is maintained at T_H and the other is at T_C (b) thermocouple behaving as a generator (c) thermocouple behaving as a cooler.

2.1.1 Seebeck Effect

The Seebeck effect was observed when two dissimilar conductors were connected and their junctions were maintained at a temperature difference. This temperature difference resulted in a potential difference being induced and is known as the Seebeck effect, named after Thomas Seebeck who recorded this phenomenon in 1821 [24]. The electric potential produced is proportional to the temperature difference by some constant, α [V/K], known as the Seebeck coefficient from the relationship

$$V_{oc} = \alpha \Delta T, \tag{2.1}$$

where V_{ocv} [V] is the open circuit voltage and ΔT [K] is the temperature difference across the junctions of the thermocouple. Therefore, the Seebeck coefficient can be calculated as

$$\alpha = \frac{V_{oc}}{\Delta T}. \tag{2.2}$$

The Seebeck coefficient for metals is in the range of few μV/K and remain unchanged with temperature, while for semiconductor materials it is in the range of hundreds of μV/K [25] and are highly dependent on temperature. The larger voltage potential is the reason for thermoelectric devices being constructed with p-type and n-type semiconductor materials. The temperature difference is created across the thermocouple junctions by placing them between a heat source and heat sink. If an electric load is connected to the thermocouple, the circuit is closed and electric current is allowed to flow as shown in Figure 2.1 (b). Therefore, this device is considered a thermoelectric generator since heat is converted to electricity.

2.1.2 Peltier Effect

When current flows through the thermocouple, heat will be absorbed at one junction and released at the opposite one depending on the direction of the current. The Peltier effect is considered the reverse of the Seebeck effect, where electrical power is converted to a temperature difference or heat. The Peltier coefficient, π [W/A], is defined as the ratio of heat, Q [W] to electrical current, I [A] such that

$$\pi = \frac{Q}{I}. \tag{2.3}$$

Using Kelvin's second relationship which states that

$$\pi = T\frac{dV}{dT} = \alpha T, \tag{2.4}$$

the Peltier heat, Q_P, can then be defined as

$$Q_P = \alpha IT. \tag{2.5}$$

When a voltage source is connected to the thermocouple as depicted in Figure 2.1 (c), heat will be pumped from the cold side to the hot side and the device is referred to a thermoelectric cooler. According to the Fourier's Law, heat is conducted from a high temperature to a low temperature. The Peltier heat flows in the direction of heat conduction for a thermoelectric generator and flows against the direction of heat conduction in a thermoelectric cooler. Therefore, the Peltier effect is considered a parasitic effect in power generation because it lowers the effective thermal resistance of the thermocouple (pumps heat from hot side to cold side).

2.1.3 Thomson Effect

As heat is conducted through the thermocouple from one junction to the opposite, a temperature gradient will result across the p-n conductors. Since the Seebeck coefficient is typically a function of temperature- as current flows through the conductors, reversible heat is generated which is known as the Thomson effect. The Thomson effect is intrinsic to a single conductor while the other two thermoelectric effects are characteristic of a junction of conductors. The Thomson heat, Q_T, that is absorbed or generated depending on the direction of the current flow is defined as

$$Q_T = \tau I \frac{dT}{dx}, \tag{2.6}$$

where τ [V/K] is the Thomson coefficient and dT/dx is the temperature gradient across the conductor. Kelvin's first relationship gives the relationship between the Thomson coefficient and the Seebeck coefficient as

$$\tau = T\frac{d\alpha}{dT}. \tag{2.7}$$

Typically, when modeling thermoelectric devices the Thomson heat is neglected [26–31]. This is valid if the Seebeck coefficient of the material does not vary with temperature or the temperature gradient across the p-n couple is small. However when the thermocouple is exposed to large temperature gradients, the Thomson effect is significant enough to not be neglected [32]. The most common approach is to calculate the Seebeck coefficient as the average of the junction temperatures such that

$$\alpha_{avg} = \alpha\Big|_{\frac{T_H+T_C}{2}}. \tag{2.8}$$

2.1.4 Joule Effect

The Joule effect is observed when electrical current travels through a conductor and is converted to heat, which is not exclusive to thermoelectrics. The Joule heat, Q_J, is equal to the internal electrical resistance of the thermocouple, R_E [Ohm], times the square of the current flowing through them

$$Q_J = I^2 R_E. \tag{2.9}$$

The Joule effect produces irreversible heat unlike the three aforementioned thermoelectric effects, which are all reversible. Also, unlike the Peltier effect the heat

produced does not depend on the direction of current flow.

2.2 Figure of Merit

Evaluating the potential of thermoelectric materials is important to predict the performance of thermoelectric devices. The dimensionless figure of merit, ZT, is defined as

$$ZT = \frac{\alpha^2 \sigma}{k} T \tag{2.10}$$

and is used to calculate the efficiency of thermoelectric materials. σ [S/m] is the electrical conductivity, k [W/m-K] is the thermal conductivity and T [K] is the absolute temperature of the material at which the properties are measured. Typically for TEGs a high power factor, PF, defined as

$$PF = \sigma \alpha^2 \tag{2.11}$$

is desirable as well as a low thermal conductivity. Since thermoelectric devices are made of positively doped (p) and negatively doped (n) semiconductors, a better formulation for the figure of merit considering the individual material properties is presented as

$$ZT = \frac{\left(|\alpha_n + \alpha_p|\right)^2 T}{\left[\left(k_n \rho_n\right)^2 + \left(k_p \rho_p\right)^2\right]^{1/2}}, \tag{2.12}$$

where ρ [Ω-m] is the electrical resistivity of the material.

In general, high ZT values are difficult to achieve because thermoelectric material properties are optimal at different temperature ranges as seen in Figure 2.2. For example, the maximum Seebeck coefficient occurs at 400K for p-type Bi_2Te_3, while it

occurs at 450K for n-type Bi_2Te_3 as observed Figure 2.2 (a). At those corresponding temperatures, a maximum in thermal conductivity is actually exhibited by Bi_2Te_3 rather than the preferred minimum as shown in Figure 2.2 (b). Therefore, TEGs have a low thermal efficiency (up to 7% [33]), defined as power output over heat input.

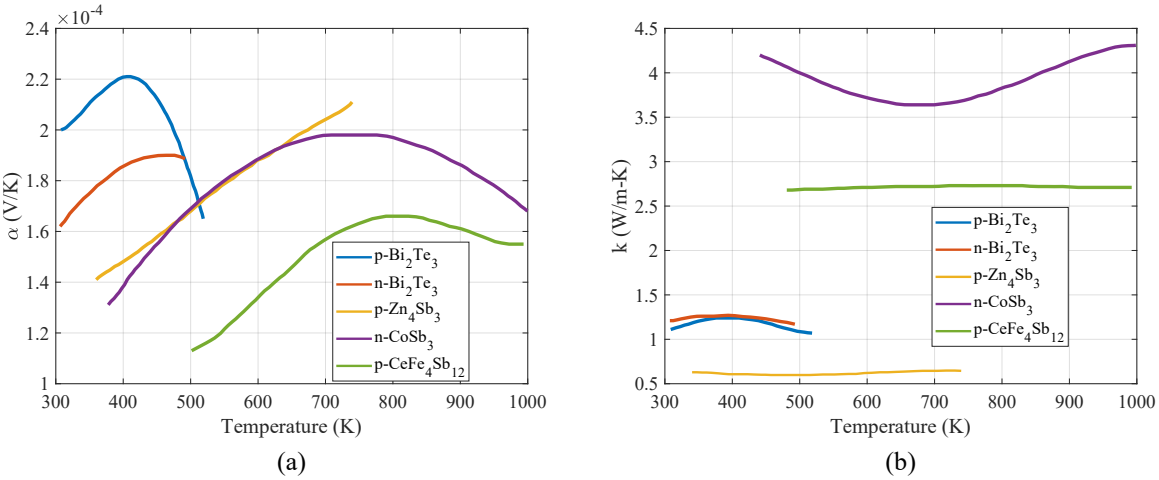

Figure 2.2: (a) Seebeck coefficient and (b) Thermal conductivity as a function of temperature [34].

Due to their acceptable ZT of about 1 [33], Bi_2Te_3 and PbTe have been the most commonly researched and implemented thermoelectric materials [35]. The highest reported ZT in the literature is about 3.5, achieved with quantum dots, as shown in Figure 2.3. It is also interesting to note that the improvement in ZT in the last decades has spurred higher interest in research of TEG materials and improving their thermoelectric properties.

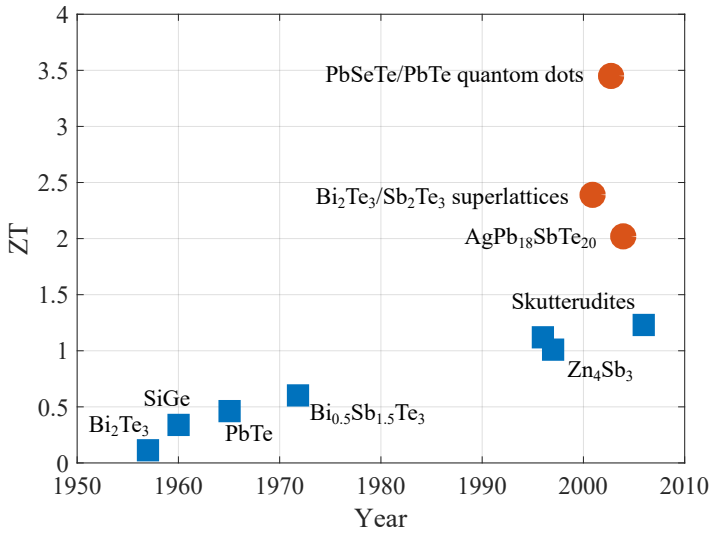

Figure 2.3: ZT of typical thermoelectric materials over time [34].

2.3 TEG Module

A TEG consists of many thermocouples, connected electrically in series and thermally in parallel as seen in Figure 2.4. Many thermocouples (couples) are connected with electrical contacts to increase the voltage output of a TEG *module*. Commercially available thermoelectric modules have a ceramic plate at the top and bottom of the thermocouple junctions to electrically isolate the module from the heat source, thus preventing a short circuit. One of the ceramic plates is labeled as the hot-side (T_H) and the opposite side is considered the cold-side (T_C). A *hot* heat exchanger (HEX) is used to transfer heat from the heat source to T_H, while the *cold* HEX cools T_C. As heat flows across the thermoelectric module, some of it is converted to electrical energy.

Considering the thermoelectric effects described earlier, by performing an energy

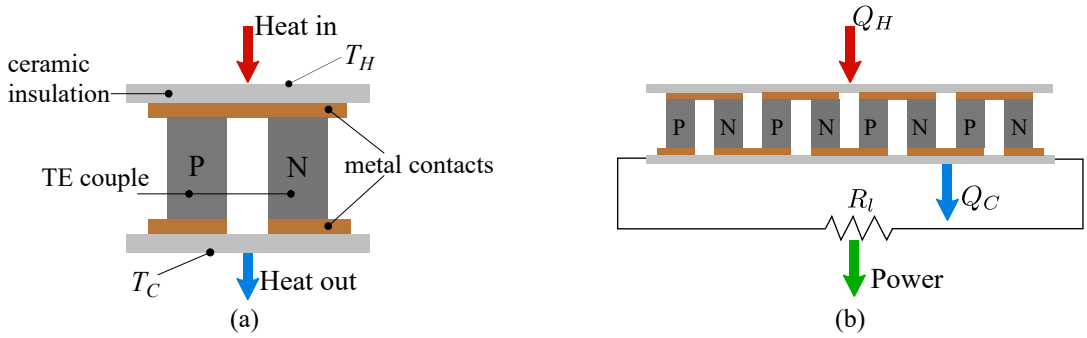

Figure 2.4: (a) Thermocouple schematic (b) many thermocouples form a TEG module

balance on the hot side of the TEG (Figure 2.4 (b)), the heat transferred through is

$$Q_H = \alpha T_H I + K_{TEG}\left(T_H - T_C\right) - \frac{1}{2} I^2 R_E, \tag{2.13}$$

where the first term represents the Peltier heat, the second term is heat conduction and the third term is due to Joule heating. K_{TEG} [W/K] is the thermal conductance of the TEG unit. Similarly, the heat rejected on the cold side is

$$Q_C = \alpha T_C I + K_{TEG}\left(T_H - T_C\right) + \frac{1}{2} I^2 R_E \tag{2.14}$$

by neglecting the Thomson effect.

According to conservation of energy $Q_H = Q_C$, however if some of the heat is converted to power then the electrical power, P, produced can then be calculated as

$$P = Q_H - Q_C \tag{2.15a}$$

$$P = \alpha\left(T_H - T_C\right) I - I^2 R_E \tag{2.15b}$$

The thermal efficiency, η, of a thermoelectric generator is defined as [36]

$$\eta = \frac{P}{Q_H} \tag{2.16a}$$

$$\eta = \frac{m\,(\Delta T/T_H)}{\frac{(1+m)^2}{T_H}\frac{1}{Z} + (1+m) - \frac{1}{2}\frac{\Delta T}{T_H}} \tag{2.16b}$$

where $\Delta T = T_H - T_C$ and m is the ratio of the electrical load resistance, R_l, to TEG internal resistance

$$m = \frac{R_l}{R_E}. \tag{2.17}$$

Chapter 3

Waste Heat Recovery in Vehicles via TEGs

3.1 Motivation

In response to alarming climate change and global warming, the Paris Agreement set a goal of maintaining the global average temperature to 2°C below pre-industrial revolution levels. To achieve this target, the International Energy Agency (IEA) suggests limiting the total greenhouse gas emissions to 1170 gigatonnes of equivalent carbon dioxide ($GtCO_2$) between 2015 to 2100 [37]. Considering the transportation sector accounts for 29% of the U.S.' greenhouse gas emissions and 14% of the world's, vehicle electrification is crucial [37]. In order to limit the number of greenhouse gases to achieve the Paris Agreement target, the IEA estimates that 60% of all vehicles need to be electrified by 2060. Electric vehicles (EV) include battery-electric vehicles (BEVs), plug-in hybrid vehicles (PHEVs) and fuel cell vehicles (FCEVs) which means

that a fraction of these EVs will include an internal combustion engine (ICE). Therefore, not only will 40% of the future vehicle fleet, operate only with ICE's but also a percentage of the 60% of electrified vehicles will include an ICE (such as PHEVs).

The trouble with the future vehicle fleet consisting of a large number of ICE's is their hindrance due to the Carnot efficiency- heat engine operating between two temperature points. There are inherent irreversibilities during the operation of ICE vehicles that prevent them from running at higher efficiencies; it is physically impossible to achieve the efficiencies of an electric motor. Approximately 20% of fuel energy in an ICE is converted to useful work while the rest is lost through friction, the cooling system and the exhaust gases as observed in Figure 1.4. Therefore, to increase the overall fuel economy of an ICE, waste heat recovery (WHR) is necessary.

In recent years, there has been increasing interest in research that investigates WHR in vehicles [38–41] through the use of thermoelectric generators (TEGs). Thermoelectric generators are solid state devices that convert thermal energy directly to electrical energy. Additional advantages are their small size, quiet operation and low maintenance requirements. Although different technologies have been investigated for waste heat recovery in vehicles, such as organic Rankine cycle or turbocharger, the challenge lies in the operation of these technologies. Vehicle operation is dynamic- the losses that are generated vary depending on driving conditions. A system which recovers energy that is lost throughout the vehicle needs to quickly respond to these variable operating conditions. Since thermoelectric generators have no moving parts, or working fluids such as refrigerants, they can handle these dynamics and still operate with minor impact to the operation of the vehicle.

3.2 Energy Sources in Vehicles

During vehicle operation, thermal losses are a result of fuel energy conversion to mechanical energy by an ICE due to system inefficiencies, as well as thermodynamic limits i.e. Carnot efficiency. The Carnot efficiency is the theoretical maximum efficiency a heat engine can achieve when operating between two temperatures and for ICE it is ∼70% [42]. These losses are potential sources of "free" energy for waste heat recovery- considered "free" since the energy would otherwise end up in the environment in the form of heat. There are different locations of waste heat that have the potential for recovery in a vehicle, whether it be an ICE or hybrid car. The maximum power available, Q_{max} [W], for recovery can be calculated as [43]

$$Q_{max} = \dot{m} C_p (T_f - T_c) \tag{3.1}$$

where $\dot{m}$ [kg/s] is the fluid mass flow rate, C_p [J/kg-K] is the fluid's specific heat, T_f [K] is the temperature of the fluid source, and T_c (typically ambient) is the reference temperature the fluid can be cooled down to.

ICE include both spark-ignition (SI) and diesel engines. Approximately 17-26% and 16-35% of the fuel energy is lost to the engine coolant for SI engines and diesel engines, respectively. While 34-45% and 22-35% of the fuel energy is lost to the exhaust gases for SI engines and diesel engines, respectively at maximum power [5]. The magnitude of the thermal losses depends on the engine size and operation of the vehicle during real driving scenarios. Table 3.1 provides approximate source temperatures for various locations in a vehicle where energy can be recovered. As can be observed, the exhaust system exhibits the highest temperatures in the vehicle

Table 3.1: Approximate fluid temperatures of heat source

Location	Temperature [°C]	Reference
Exhaust manifold [a]	550 - 790	[44]
Catalytic converter [a]	320 - 520	[44]
Radiator	90 - 120	[45]
EGR	540 - 770	[46]

[a]Diesel engines are 100-200 degrees lower

which make it the location most researched area for waste heat recovery in a car. As exhaust gases move downstream towards the tailpipe, losses occur to ambient and the temperature decreases. Typically, the location for waste heat recovery along the exhaust system is after the catalytic converter (CC) to avoid interfering with the minimum temperature required for the catalyst to reduce emissions. The radiator is another potential location for waste heat recovery; the hot coolant which maintains the engine block below critical temperatures, is cooled in the radiator. Although the radiator has the lowest temperatures, a benefit is that a heat exchanger unit already exists for extracting the energy from the coolant hence, converting this energy has minimal impact. The Exhaust Gas Recirculation (EGR) cooler is another option as well. The exhaust gases that are recirculated back to the cylinder for NOx emissions reduction, require cooling before injection into the cylinder, therefore the EGR cooler has the same benefits as the radiator.

The potential for waste heat recovery not only depends on the temperature of the fluid source but also its mass flow rate. Approximate mass flow rate values are found in Table 3.2. The mass flow rate of the exhaust gases varies rapidly during a drive cycle and more aggressive driving conditions result in higher mass flow rates. Typically, 20-50% of the exhaust gases are recirculated back to the engine cylinder in EGR

applications, depending on the engine size and cylinder charge temperature control strategy [47,48]. Compared to the coolant flow rates, the exhaust mass flow rates are a magnitude lower. According to [49], advanced engines require 1-1.7L/min/kW, which results in high mass flow rates for the coolant. Even if electrical pumps were used in all ICE vehicles instead of mechanical belt-driven pumps, 1L/min/kW is necessary to meet the cooling demands of the engine block.

Table 3.2: Approximate fluid mass flow rates of heat source

Fluid	Mass flow rate [kg/s]	Reference
Exhaust gas (gasoline)	0.01 - 0.045 [a] ; 0.01 - 0.11 [b]	[50]; [51]
Exhaust gas (diesel)	0.1 - 0.4 [c]	[26]
Coolant	1.84 - 3.13 [d]	[49]

[a] 190kW engine, FTP drive cycle
[b] 180kW engine, 120-140kmh highway driving
[c] 290kW engine, reduced Paris-Lille drive cycle
[d] Calculated for 100kW engine

When choosing the location for waste heat recovery, both temperature and mass flow rate of the system need to be considered since they determine the amount of energy available for recovery and the operating conditions for the WHR technology. Next, the thermoelectric technology that can be implemented in these various locations based on their optimal operating temperatures is presented.

3.3 Thermoelectric Generator Technology

As previously discussed in Section 2.2, the figure of merit, ZT, is used to compare the potential performance of different thermoelectric materials. Generally, large ZT values are desirable. Currently ZT values of common thermoelectric (TE) materials

are in the range of 1-2. It is estimated that a 10% fuel efficiency gain can be achieved if a TEG has a ZT value of 2 [52, 53]. It should be noted that in the literature, maximum ZT values are reported when researching TE materials, however, they vary with temperature. This is pointed out in Figure 3.1, where ZT values are plotted as a function of temperature for various materials. The operating temperature of TEGs is dynamic in waste heat recovery applications for vehicles, therefore the average ZT value over the temperature range is important when considering material selection for the module for a specific application. Also, the ZT of the p-type and n-type of the same material are not equal over the same operating temperature, hence this needs to also be considered when manufacturing a TEG module.

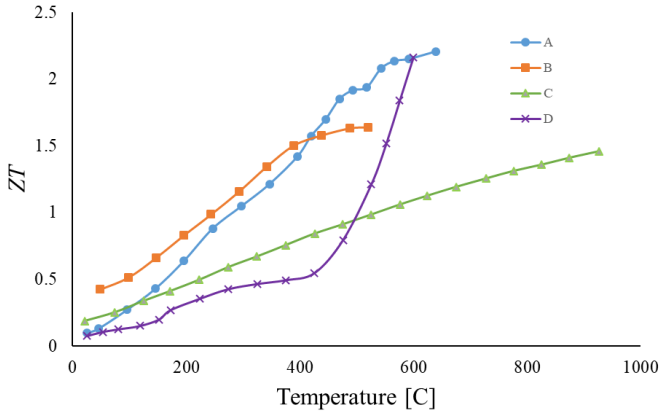

Figure 3.1: ZT as a function of temperature for various TE materials (A. p-type PbTe endotaxially nanostructured with SrTe [54]),(B. Skutterudite $Co_{23.4}Sb_{69.1}Si_{1.5}Te_{6.0}$ [55]),(C. p-type FeNbSb half-Heusler [56]), (D. p-type polycrystalline $Sn_{.95}Se$ [57]).

Commercially available TEGs have a $ZT \approx 1$ which results in a thermal to electrical conversion efficiency of $\sim$5%. The most commonly used material for TEGs is Bismuth Telluride (Bi_2Te_3), which has long been proven to work in low temperature settings (<250°C). Lead Telluride (PbTe) and Silicon Germanium (SiGe) alloys are

also commercially installed but are for higher temperature applications. Other prominent TE materials are TAGs (Te-Ag-Ge-Sb), half-Heusler and Skutterudites, which have been investigated materials for waste heat recovery in vehicles [38, 58, 59] and work best in the operation range of: PbTe (∼500-600°C), TAGs (200-500°C), Half-Heusler (400-600°C) and Skutterudite (500-800°C). For the most part, TEG modules are manufactured using multiple TE materials.

Modules are manufactured from ingots which are cut into cubes (legs) for each p and n material. Due to their geometry, the p-n legs are connected to form a flat TEG module. Flat TEG modules are commercially available and the vast majority of researchers use flat TEGs for waste heat recovery systems in vehicles. Although [60] manufactured TEGs that appear cylindrical, p-n legs were placed in a circular formation to create a better interface between the exhaust gas heat exchanger and the TEGs. However, some have investigated other shapes such as annular TEGs. Instead of using p-n legs, p-n disks are used and potential advantages are easier integration with tubular heat exchangers that can fit more compactly in vehicle exhaust systems [61–63]. Figure 3.2 (a) shows a typical off-the-shelf TEG and Figure 3.2 (b) a prototype of a cylindrical TEG module. Annular TEGs are still in the research phase, as it has been difficult to manufacture the TE disks.

As previously discussed, since the ZT value of the TE material varies with temperature, *segmented* TEGs have also been investigated. During operation of the TEG, the p-n legs will experience large temperature gradients, especially in vehicle applications. Therefore, using different TE materials in the direction of the heat flow (**Heat In** in Figure 2.4 (a)) of the TEG is advantageous, making each TEG leg of *segmented* material. The TE material along each TE leg is chosen for optimum performance at

the predicted temperature gradient. In [64, 65], the authors demonstrated through their computational modeling that TEG efficiency is enhanced through segmented TEGs, and can reach efficiencies higher than 10%. Crane et. al. [66] manufactured segmented TEGs for recovering waste heat in the exhaust system of vehicles, and had a 100% increase in efficiency compared to a TEG without segmentation.

(a) (b)

Figure 3.2: (a) off-the-shelf flat TEG module (b) cylindrical TEG module concept [63].

3.3.1 Electrical Characteristics

The equivalent heat flows in a TEG shown in Figure 2.4 (a) and discussed in Section 2.3 are portrayed in electrical form in Figure 3.3 (a). The electrical model for a TEG is seen in Figure 3.3 (b). The output voltage of the TEG, V_{TEG} [V], is calculated as [36]

$$V_{TEG} = V_{oc} - IR_E \tag{3.2a}$$

$$= \alpha\,(T_H - T_C) - IR_E \tag{3.2b}$$

where I [A] is the current flowing through the TEG and R_E [Ohm] is the electrical internal resistance of the TEG. Hence the power output, P [W], of the TEG is defined

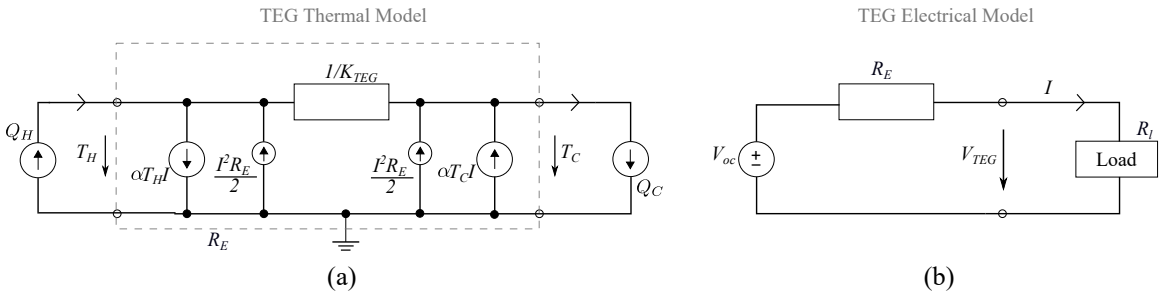

Figure 3.3: (a) Heat flows in electro-thermal TEG equivalent circuit (b) Electrical circuit.

as the product of voltage and current [36]

$$P = V_{TEG} I \tag{3.3a}$$

$$= \alpha \left(T_H - T_C\right) I - I^2 R_E \tag{3.3b}$$

For a fixed T_H and T_C, the maximum power output (P_{max}) will occur when $IR_E = V_{TEG}$, which means that it occurs when V_{TEG} is half the open-circuit voltage ($V_{oc}/2$), and $P_{max} = \frac{\alpha \Delta T}{2} I$. A characterization of a TEG module, TEG1-12610-5.1 from TECTEG MFR is performed by maintaining T_C at a constant 35°C and varying T_H between 100°C and 250°C; the results are shown in Figure 3.4. V_{TEG} and P are plotted versus current, and the maximum power occurs at $V_{oc}/2$ or half the short-circuit current, I_s. However, precaution should be taken when making this assumption when modeling the entire TEG waste heat recovery system, since taking into account the thermal resistance of the heat exchangers will shift I_s [67], i.e. I_s at the module level is not equal to I_s at the system level. An approximation for the maximum power is derived by noting that the max power occurs when $\frac{dP}{dI} = 0$ and (3.3b) becomes $\alpha \Delta T = 2 I R_E$ which results in $I_{max} = \frac{\alpha \Delta T}{2 R_E}$ hence $P_{max} = \frac{(\alpha \Delta T)^2}{4 R_E}$.

The Seebeck coefficient, open circuit voltage and R_E are all temperature-dependent.

This can be observed from Table 3.3, where the values were computed from the characterization performed at various temperature differences across the TEG module.

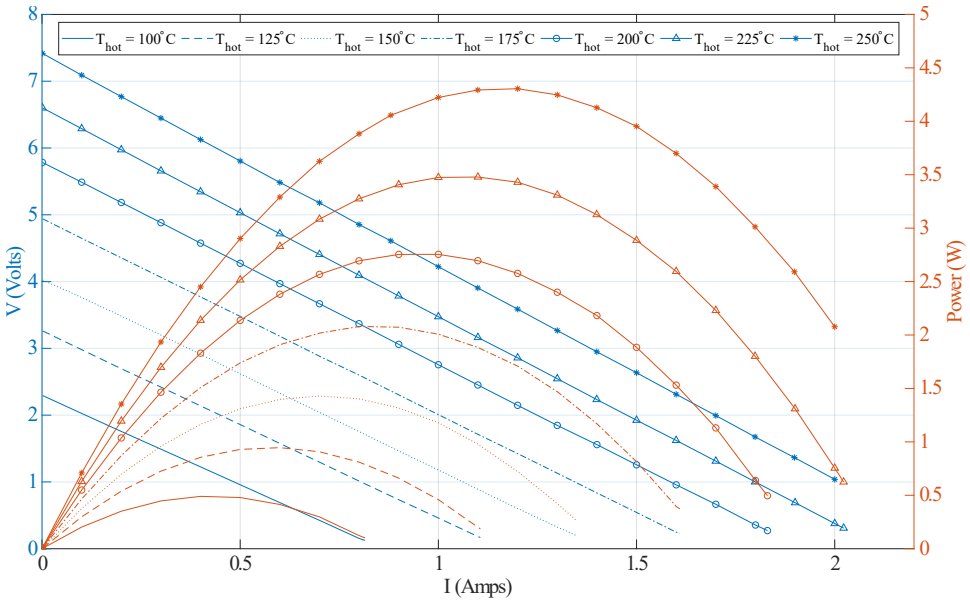

Figure 3.4: Characterization of an off-the-shelf TEG module from TECTEG MFR. T_C is 35°C.

Table 3.3: TEG module characterized properties

ΔT	α [V/K]	V_{oc} [V]	R_E [Ohm]
65	0.035	2.29	2.70
90	0.036	3.26	2.80
115	0.035	4.02	2.86
140	0.035	4.94	2.93
165	0.035	5.78	3.02
190	0.034	6.59	3.11
215	0.034	7.41	3.18

3.3.2 Thermal Characteristics

The thermal response of the TEG not only depends on the temperature difference applied across the thermoelectric junction but also on the Peltier and Joule heat. In general, since V_{oc} ((2.1)) depends on the temperature difference, a large ΔT is desirable, hence the thermal resistance of the TEG should be large to achieve this. However, the Peltier effect negatively affects the TEG because the effective thermal resistance of the TEG decreases as current is increased through the TEG, i.e. ΔT decreases as current is increased. Due to the Peltier effect, heat is absorbed in the hot junction and emitted in the cold side. Joule heating as well, reduces the total power produced by the system if (3.3b) is observed. Hence in general, TEG modules with lower operating currents are desirable. More detail regarding modeling of the physical phenomena of TEGs is presented in the modeling Section 4.1.1.1.

3.4 TEG Waste Heat Recovery System

Waste heat recovery (WHR) is the process of recovering energy that would be lost to the environment in the form of low-grade heat and converting it to high-grade electrical energy. Waste heat recovery can be implemented via TEGs by creating a temperature difference across the TEG module. In the previous section, the thermoelectric module technology was discussed but the other components necessary for a TEG WHR system are heat exchangers (HEXs). Heat exchangers are devices that transfer heat from one medium to another medium. The *hot* HEX extracts energy from the waste heat source and transfers it to T_H and the *cold* HEX completes the thermal circuit by cooling T_C. A schematic of a TEG WHR system is shown in

Figure 3.5 with the equivalent thermal resistances. Once a temperature difference is maintained across the TEG modules, a power conditioning unit is necessary to connect the output power of the TEG system to the vehicle.

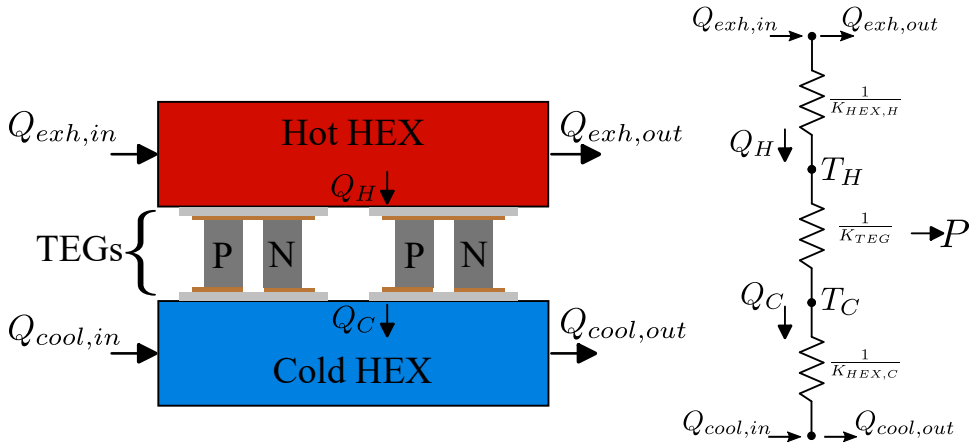

Figure 3.5: Schematic of TEG WHR system and thermal resistances in system.

3.4.1 Hot Side Heat Exchanger

Hot HEX's are necessary to extract thermal energy from the waste heat source in a vehicle and transfer it to a TEG. Preferably, T_H of the TEG should be as close as possible to the exhaust gas temperature to achieve a higher power output as expected from (3.3b). However, there is a temperature drop from the exhaust gas temperature to the temperature of the hot side of the TEG due to the thermal resistance of the hot HEX. The thermal resistance of a heat exchanger can be decreased by either increasing the surface area or the heat transfer coefficient of the HEX. The heat transfer coefficient, h (W/m^2K) is proportional to the Reynolds number (Re) which is dependent on the velocity of the gases. Since the majority of the research for TEG WHR systems in vehicles focuses on the exhaust system, low mass flow rates

in the exhaust gases (Section 3.2) hinder the achievement of a high heat transfer conductance. Wang et al. [41] showed that enhancing the hot TEG side heat transfer significantly increases the power output and efficiency of a TEG. Therefore, heat transfer enhancement techniques have mostly been studied for the hot HEX [68–72]. Passive enhancement techniques involve different geometries of fins, spiral inserts, baffles, etc. and their orientation placement in the heat exchanger have also been investigated. Niu et al. [71] suggested making the baffle angle adjustable for an automotive exhaust HEX to accommodate for various engine operation conditions thus increasing the power output of the TEG.

Typically, rectangular-duct HEX geometries have been investigated for harvesting the energy from the exhaust since they can fit compactly in the exhaust system [73]. Liu et al. [74] found that placing the HEX between the CC and the muffler resulted in the lowest pressure drop and uniform temperature distribution of the HEX surface (location of TEGs). Pressure drop in the HEX is important to consider since the HEX is placed in the flow path of the exhaust gases and this creates a backpressure on the engine. In general heat transfer enhancement and pressure drop are related, so a trade-off is made when choosing the optimum heat exchanger design. For this reason, plate-fin heat exchangers are commonly used in the literature since they provide good heat transfer enhancement with acceptable pressure drop [26, 75]. Wang et al. [76] tested a plate-fin HEX filled with metal foam for enhancing TEG waste heat recovery and calculated a HEX efficiency of 83.56% with a total pumping power of .84W, for a total heat recovery of 285.3W.

3.4.2 Cold Side Heat Exchanger

The cold side HEX has the lowest thermal resistance (liquid-cooling) in the TEG WHR system and therefore is not a limiting factor in terms of heat transfer for the system. The majority of researchers have focused on liquid-cooling for the cold HEX due to the possibility of tapping into the cooling system of the vehicle. Variations of cold-plate designs have been implemented to cool the cold side of the TEG. Therefore, there is not much research in enhancement techniques for the cold HEX. Hendricks et al. found that the cold HEX thermal resistance needs to be 10-30 times less than that of the hot HEX to optimize the power output of the system [77]. Currently, there is limited research on the effect of the additional cooling load on the vehicle due to the cold HEX used by a TEG system. However, for hybrid vehicles, this can be advantageous since there are heating loads that can no longer be met entirely by the engine during vehicle warm-up [78].

3.4.3 Power Conditioning Unit

Once the TEGs are exposed to a temperature difference, an electrical load is connected to the TEGs for power generation. The TEG WHR system will include several TEG modules and a decision is required regarding their electrical connection. The TEG modules can either be connected in series, in parallel or some combination of both depending on the desired output voltage. Studies have been conducted to understand how the electrical configuration affects the power output and as explained previously, the maximum power output of the TEG is of interest since the energy recovered is considered “free”. Montecucco et al. [79] connected TEGs at different temperatures differences in series and also in parallel, to study the total power produced. As

expected, the total power output was lower than the sum of the max power of each individual TEG, but the parallel TEG connection resulted in lower power produced than the series connection. Just like batteries, if a TEG is connected to another TEG with a dissimilar temperature difference (i.e. different, V_{oc}), the TEG with the lower ΔT consumes power from the other TEG.

When TEGs with different temperature differences are connected electrically in series, there is a current mismatch at the maximum power point and when they are connected in parallel, the mismatch exists at the voltage. Ideally, each TEG would have its own power converter to ensure the maximum power is transferred to the vehicle battery, but there is a trade-off between gain in power and added complexity. Hence a decision is required on the number of converters installed for rows or groups of TEGs. If TEGs are connected in parallel an advantage is that if one module fails, the rest continue to be operational but in general a larger current input is needed. At high current, larger diameter electrical leads for the TEG are necessary and Joule losses are higher. Therefore, TEGs are usually connected in series in the literature.

As explained previously and observed in Figure 3.4, the power output from the TEG will change due to the operating conditions, hence maximum power point tracking (MPPT) is crucial to ensure the maximum available power is produced instantaneously. A review of MPPT schemes found in the literature are presented in Chapter 5.

3.4.4 Additional Components/Considerations

Interface materials are essential for mounting the TEGs on the HEXs, thus reducing the thermal contact resistance and allowing better heat transfer. Thermal interface

materials (TIMs) take the form of pastes, greases or sheets and these are placed between the TEG and the surface of the HEX. Thermal pastes harden at high temperatures; therefore, phase-change thermal pads may be considered for the hot side of the TEG as well as carbon-based TIMs [35]. Another factor that determines the contact resistance between the TEGs and HEXs is the applied pressure. The TEG WHR system assembly needs to be mechanically compressed to ensure maximum power output from the system. Wang et al. [80] experimentally showed that the output power increased by 61% when using thermal grease and the power increased by 33% when the pressure applied to the TEG was increased from 109kPa to 765kPa.

3.5 Experimental Work

The first TEG WHR system experimentally investigated in the exhaust system of a vehicle was by Birkholz et al. in 1988. The TEG WHR system produced 58W when tested on a 944 Porsche, at maximum engine load [81]. Since then, other researchers as well as major automotive manufacturers have investigated waste heat recovery in vehicles through the use of thermoelectric generators. Funded by the U.S. Department of Energy (DOE), BMW and Ford designed a fully integrated TEG WHR system whose ultimate goal was to achieve a 10% gain in fuel efficiency for passenger vehicles [60]. Although they began with flat TEG modules, their design evolved to arranging the TEG couples in a cylindrical form. BMW also built an integrated TEG WHR system in the EGR cooler of a diesel vehicle with PbTe TEGs that produced a max power of $\sim$250W [82]. General Motors was funded separately by the DOE and explored Skutterudite flat TEGs [83]. Honda and Hyundai have investigated TEG WHR systems for hybrid electric vehicle applications [84], [85].

The mentioned automotive companies had similar designs which included the exhaust gas HEX (rectangle, hexagon, etc.) in the center, TEGs attached to the outer surface of the exhaust HEX and coolant tubes or blocks on the outside of the system. Eventually BMW's thermoelectric manufacturing partner, Gentherm, changed their TEG WHR design to include the coolant HEX in the center, the TEGs on the perimeter of the coolant HEX and the exhaust gases flowed through the outside. The outcome of their second design, TEG "cartridges", had net zero fuel efficiency gains for a BMW X3 (2L turbocharged engine) for a US06 drive cycle due to the added weight of the system and because it was installed in the center muffler (exposed to lower temperatures). However, when a larger TEG system was installed immediately after the CC on a F350 (6.2L, V8) a fuel efficiency gain of 1.2% was achieved [86].

Table 3.4: Experimental TEG WHR system power output reported in the literature

Location	Engine	TEG Max Power [W]	Driving Conditions	Hot HEX	TEG Material/ Module	Cold HEX	Ref
Exhaust manifold	944 Porsche 2.7L	58	max engine load	square channel	$FeSi_2$	coolant block	[81]
Turbocharger exit	Cummins NTC350 14L	1068	300HP 1700 RPM	octagonal fins	HZ-13	coolant block	[87]
Exhaust manifold	3L	35.6	constant speed (60km/h, hill climb)	flat plate fins	SiGe	coolant block	[88]
After CC	1999 Sierra GMC 5.3L V8	130/255	constant speed (112.6km/h)/7.2% incline	offset strip fin	HZ-20	coolant block	[89]
Radiator	$\sim$ 2L	75	constant speed (80km/h)	tube block	Bi_2Te_3	heat pipes/fins	[90]
After CC	BMW 530i 3L 6cyl	605/450	constant speed (110kmh)/US06 drive cycle	fins in cylinder	half-Heusler /Bi_2Te_3	coolant tubes	[60]
After CC	2L	600	constant speed (125km/h)	"fishbone" finned	- -[a]	water block	[91]
After CC	Chevy Suburban 5.3L	57	US06 drive cycle	- -	Skutterudite	coolant block	[83]
Exhaust pipe	Caterpillar diesel	1000	constant mass flow (.48kg/s)	flat plate fins	half-Heusler	cold plate	[59]
Exhaust manifold	turbocharged diesel 4L 6cyl	119	constant 2000RPM (.6MPa BMEP)	flat plate fins	Bi_2Te_3	cold plate (finned structure)	[92]
After CC	Golf 1.4L TSI 4cyl	111/30	2000RPM, 85%FTTP /NEDC drive cycle	square channel	TEG1-12611-6.0	cold plate	[39]
Exhaust manifold	2L 4cyl SI for hybrid	98.8	constant 3000RPM .6MPa BMEP	hexagonal fins	1261G-7L31-05CQ	hexagonal fins	[85]

[a] p-n material properties given

Table 3.4 summarizes other achievements for TEG WHR systems in the literature. The work presented, is by researchers who experimentally evaluated the performance of their systems on engines and provided the maximum power generated. Engines were mostly tested under steady-state conditions and engine loads that resulted in high exhaust mass flow rates and temperatures from the engine. It should also be noted that different engine sizes result in different quantities of thermal losses available and large heavy-duty engines such as [59] can produce higher power output from a TEG WHR since the engines exhibit higher exhaust mass flow rates. Bass et al. [87] successfully recovered over 1kW of electrical power from a diesel truck engine after discovering that heat transfer enhancement was needed for their hot HEX design. Thacher et al. [89] quantified the parasitic losses of the TEG WHR system on an engine truck, by taking into account the rolling resistance due to the added weight and the back pressure of the HEX. At high speeds, the pressure drop across the hot HEX was actually lower than the system without the HEX due to lower exhaust mass flow rates caused by the increase in fuel efficiency. Almost 2% fuel efficiency gains were achieved at 120 km/h.

Although the majority of the research has focused on waste heat recovery from the exhaust gases, other locations have also been experimentally investigated. Kim et al. [90] took advantage of the fact that the radiator is already a HEX in the vehicle and installed heat pipes to transfer energy from the hot coolant to TEG modules. They calculated the electrical power efficiency to be 0.3% at a vehicle speed of 80kmh. Massaguer et al. [39] tested a small TEG WHR system on a Golf TSI engine and found that the TEGs produced lower power than expected during an NEDC drive cycle, but this was due to designing for the maximum expected temperature. However, once the

system was redesigned for the most common temperature range in the NEDC drive cycle, different TEG modules were used and fins were added to their hot HEX design. The redesign is expected to achieve over 200W in the NEDC drive cycle.

3.6 Future Trends

3.6.1 Advances in TE Materials/Modules

In the last decade, research on improving thermoelectric materials has made great strides [93]. Observing (2.10), low thermal conductivity (k) and high power factor ($\alpha^2\sigma$) is desirable for achieving high ZT values of TE materials. Techniques such as suppressing the mean-free path of phonons and optimizing carrier concentration has succeeded in doubling or tripling the ZT of some materials. The highest ZT value reported in the literature is 2.6 for an SnSe single crystal [94]. Other promising materials include BiCuSeO due to its low thermal conductivity, low cost, non-toxicity and thermal stability [93]. High temperature TE materials have also gained increasing interest [95, 96], since they are more suitable in the vehicle exhaust environment compared to the commonly used Bismuth Telluride modules. However, translating the added benefits of high temperature thermoelectrics from the material level to the module level has proven to be challenging. Stobart et al. [95] observed up to a 23% reduction in Seebeck coefficient as well as higher electrical and lower thermal resistance than expected, as a result of the fabrication process. Bonding techniques continue to be an area of research as inefficient joining of the electrical contacts results in higher electrical resistance than desired. However, improvements continue to

be made, recently a Bismuth Telluride/Skutterudite segmented module was manufactured and tested with 12% efficiency [97]. Improving thermoelectric materials and manufacturing techniques for thermoelectric modules is a highly intensive ongoing research topic and more in-depth reviews are found in [98, 99].

3.6.2 Higher System Integration

TEG WHR system performance not only depends on the available TE materials but also on the high integration with HEX design to optimize the power produced by the system. Currently, flat TEG modules are mounted on heat exchangers with thermal interface materials to reduce the contact thermal resistance between surfaces. These contact resistances contribute to losses in the overall system, thus a lower efficiency is achieved. Advances in additive manufacturing could potentially reduce or eliminate these losses. The researchers in [100], 3D printed Bismuth Telluride half rings and mounted them on a pipe (heat exchanger) with silver paste to demonstrate the potential of conformal-shape printed TEGs. As advances are made in the field of additive manufacturing, the potential of printing the TE p-n legs directly on the surface of a heat exchanger would eliminate the contact resistances and shape-conforming TEGs would allow for more compact HEX designs, thus increasing the overall performance of a TEG WHR system in a vehicle.

Achieving a lower thermal resistance of the hot side HEX is also crucial for increasing the power output of the system. Although different heat transfer enhancement techniques have successfully been reported in the literature as were mentioned in Section 3.4.1, recently heat pipes are being investigated for increasing the heat transfer rate from the exhaust gases to the hot side of the TEG. Cao et al. [101] designed a

system that utilized heat pipes and studied the heat transfer enhancement for varying heat pipe insertion depths and heat pipe angle with respect to the exhaust flow. They found that an insertion depth of 60mm and angle of 15° were optimal for enhancing the power output of the TEGs by 10.2%.

Li et al. [40] also employed heat pipes, but used them for both the hot side and cold side HEX. Their multiphysics model investigated a cylindrical TEG WHR system where heat pipes were placed in the radial direction and concentric TEG modules were used. Two configurations were studied, one with the exhaust flow through the center of the system (coolant flow through the outside) and the second with coolant through the center (exhaust flow through the outside). Their modeling results demonstrated that the system with exhaust flowing through the outside generated higher power since this increases the heat transfer area for the exhaust gas, which has a lower convective heat transfer than water. It should be noted that the studies with heat pipes for the hot HEX have limited the operating range to ∼250-270°C and further research is required for obtaining higher operating temperatures for heat pipes. However, this temperature limit is not a problem for the cold side HEX. Lv et al. [102] found that using heat pipes for cooling the cold side of the TEG resulted in a higher power output and lower cost compared to a finned-heat sink and a water-cooled block, through their experimental study.

3.6.3 Transient System Design

A shift has been observed in analyzing TEG WHR systems for vehicle applications from a steady-state point-of-view to a transient design approach. As indicated in Table 3.4, the majority of the research has previously focused on testing TEG WHR

systems at steady-state points of operation and when the systems are tested under transient conditions, the power output is lower than expected [39, 60]. However, by developing transient models the system may be analyzed for different driving conditions such as drive cycles.

A recent study by Massaguer et al. [39] demonstrated that if a TEG WHR recovery system is designed for the maximum power conditions, the system does not perform well under dynamic driving conditions. The reason being that maximum engine loads are not indicative of what occurs in real drive cycles. Their system was originally designed for the steady-state engine condition of 2000 RPM and 85% full-throttle pedal position (FTTP) and produced 111 W under these conditions. However, when the system was tested under the NEDC drive cycle, the maximum power produced was only 30 W due to lower exhaust gas temperatures encountered in the drive cycle. Also, Lead Telluride TEG modules implemented in their system have a lower performance at low temperatures. The system was redesigned for the most common temperature range of 260-380°C and more appropriate TEG modules made of Bismuth Telluride were used instead, where a bypass design concept was introduced to ensure the TEGs would not overheat at times in the drive cycle when this temperature was exceeded.

A dynamic model and experimental validation were presented by Lan et al. [103] for a 4-module TEG WHR system tested in the exhaust of a heavy-duty diesel truck engine. The goal was to create a model that could predict the performance of the TEG modules under transient conditions, as well as to develop temperature control strategies by accurately predicting the exhaust exit temperature from the hot HEX. A model was created of a 20 TEG module system that was installed upstream of the Diesel Particulate Filter (DPF) and the hot HEX exit temperature had a requirement

of 548K for the DPF to work appropriately, resulting in an average power output of 170-224 W. The authors also suggested a bypass solution to ensure the TEG modules would not exceed their temperature limit and to ensure the DPF performance was not degraded. A controller was implemented for the exhaust bypass valve, and based on the measured exhaust inlet temperature, the dynamic model could predict the exhaust HEX exit temperature (inlet to the DPF).

3.6.4 Maximum Energy Recovery

Although researchers have previously focused on maximum power produced by the TEG WHR system as a performance metric, recently there has been a trend towards evaluating the energy recovered by the system. Kim et al. [104] integrated the power produced by a TEG WHR system with 60 TEG modules for 4 different vehicle drive cycles to understand the performance of the system for each drive cycle. Taking into account the pumping losses for the cold side HEX, the integral of the net power generated over the integrated engine power during the drive cycle was used to calculate the energy % gain. The energy gains ranged from 1.54% (WLTC drive cycle) to 1.68% (FTP-75 drive cycle).

In [105], the authors proposed a method for evaluating the potential fuel economy gains as a function of the generated power of the TEG WHR system and the back-pressure created by the system. They proposed either experimentally or numerically testing a TEG WHR system design at various engine operation points to derive a mathematical relationship between the power generated and backpressure imposed on the engine. This is done to determine a region where fuel economy is positive and to test if the proposed TEG WHR system will operate in this positive fuel economy

region for most of the operating conditions of the engine. It is interesting to note that the maximum fuel economy point does not coincide with the maximum net power generation of the TEG WHR system. Yang et. al [106] have proposed a multi-objective optimization based on their transient TEG WHR system model. The objective is to minimize the number of TEG modules in the system while constraining the allowable pressure drop of the hot heat exchanger, in order to investigate the potential for fuel economy improvement.

Finally, there have been researchers not only investigating the feasibility of TEG WHR systems in passenger vehicles but also researching large heavy-duty truck applications. Since these vehicles have larger engines that produce higher thermal losses and exhibit high exhaust mass flow rates, studies have been conducted into the feasibility of TEG WHR in these vehicles [38, 107].

Chapter 4

TEG Modeling

4.1 Literature Review

Accurate models are necessary to predict the operating conditions of a TEG WHR system and hence the power output potential. As previously discussed in Section 3.3.2, the temperature difference across a TEG is also dependent on the electrical load applied. Therefore, to predict the operating temperatures of TEGs in a vehicle system, both the thermal and electrical characteristics must be modeled. The operating temperatures dictate the type of TEG module to choose for a system and the expected voltage generated (hence the power conditioning unit). Since the power output of a TEG varies with the electrical current (Figure 3.4), MPPT schemes must be employed to ensure the maximum power is produced by the TEG at all operating points, thus increasing the overall energy recovered (integration of power with time) and system efficiency. A schematic for the complete TEG WHR system is shown in Figure 4.1. To further understand how the power produced by the TEG depends on both thermal and electrical boundary conditions, a review of the thermal models

found in the literature is presented and the TEG WHR electro-thermal governing equations are shown. Sections 4.2 through 4.4 go over the models developed in this thesis to study the effects of TEG system design on power output, as well as their respective experimental validations.

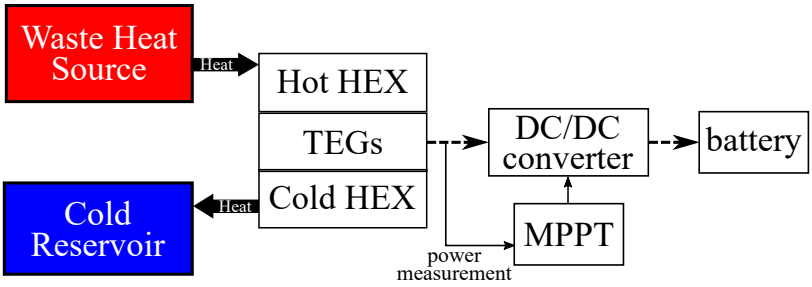

Figure 4.1: TEG WHR system.

4.1.1 Electro-Thermal Modeling

The majority of the research that explores modeling of thermoelectric generators focuses on how the boundary conditions (working conditions) affect TEG power generation and efficiency. Models simulate a single p-n couple (or a few) and parametric studies are performed by varying the length, area of the p-n pair, packing ratio, material properties etc. to observe its effect on power generation and efficiency. In general, the models can be categorized by the following assumptions: 1) fixed T_H and T_C temperature [108–110], 2) fixed heat source temperature and considers thermal resistance of the heat exchanger [111–113]. These models are important for providing guidelines for TEG module design that maximizes the power output of the module for specific applications (heat source temperature). The third, 3) considers exhaust flow direction [26, 41, 114–116] and is crucial to evaluate TEG performance in a real

system. As the exhaust gas flows through the heat exchanger, energy will be transferred to the TEGs nearest to the inlet first and less energy is available for the TEGs downstream.

Waste heat recovery in vehicles is a dynamic operation and transient effects have also been considered by several researchers. Meng et al. [23] developed a 3D transient model of a TEG to capture the coupled energy and electrical potential phenomena. By varying T_H and T_C, the transient effects on power generation were investigated and it was concluded that the output power changes synchronously with load current but the thermal response is much slower. Guo et al. [28] presented a dynamic model of TEGs with finned heat exchangers for both the hot and cold side and investigated the effects of varying heat source temperatures and mass flow rates. They observed that when the heat source temperature changes rapidly, a power spike is produced by the TEG, hence rapid variations should be avoided to protect the electrical equipment.

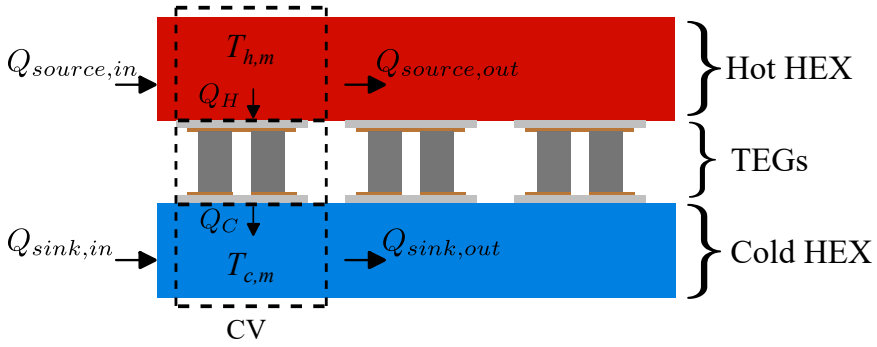

Figure 4.2: TEG WHR thermal system model schematic.

4.1.1.1 Electro-Thermal Model Description

Consider the schematic of the TEG WHR system in Figure 4.2. As exhaust gases enter the hot HEX, heat is transferred through the TEGs to the cold-side HEX.

The model can be discretized in the flow direction to form a control volume (CV) around each TEG or p-n couple (see Figure 4.2). Performing an energy balance on the CV, the rate of heat transfer for the exhaust gases (ΔQ_{source}) and the cooling fluid (ΔQ_{sink}) at steady-state are defined as

$$\Delta Q_{source} = \dot{m}_e C_{p,e} \left(T_e - T_{out}\right) = Q_H \tag{4.1a}$$

$$\Delta Q_{sink} = \dot{m}_w C_{p,w} \left(T_{w,out} - T_w\right) = Q_C \tag{4.1b}$$

where $\dot{m}_e$, $C_{p,e}$, T_{exh}, and T_{out} are the mass flow rate, specific heat, inlet and outlet temperatures of the exhaust gas, respectively. The same is defined for the cooling fluid (T_w). Q_H is the heat rate entering the TEGs and Q_C is the heat rate exiting the TEGs, with no power generation (or thermal losses) resulting in $Q_H = Q_C$.

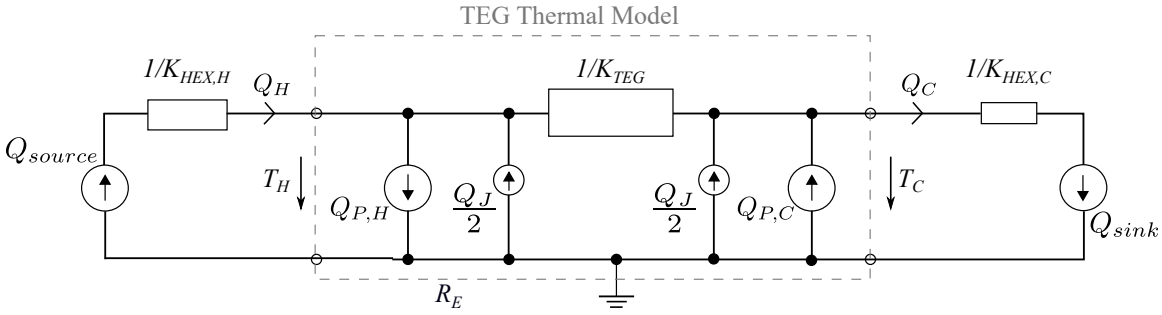

Figure 4.3: Heat flows in electro-thermal TEG equivalent circuit including resistances of heat sinks.

The equivalent electro-thermal circuit of the TEG WHR system is shown in Figure 4.3. There is an inherent temperature drop from the exhaust gases to the hot side temperature of the TEG (T_H) due to the heat exchanger thermal resistance. The

heat transferred from the heat exchangers to the TEGs is calculated as

$$Q_H = K_{HEX,H}\left(T_{h,m} - T_H\right) \tag{4.2a}$$

$$Q_C = K_{HEX,C}\left(T_C - T_{c,m}\right) \tag{4.2b}$$

where $T_{h,m}$ is calculated as the average temperature of the inlet and outlet exhaust temperatures of the CV. $T_{c,m}$ is similarly defined and is the average temperature of the cooling fluid inlet and outlet. $K_{HEX,H}$ and $K_{HEX,C}$ are the thermal conductance of the hot HEX and cold HEX, respectively, over the CV.

Considering constant cross-sectional area of the p-n legs and material temperature-independent properties, the heat transferred through the TEG is calculated at each junction as [36]

$$Q_H = \alpha T_H I N + K_{TEG}\left(T_H - T_C\right)N - \frac{1}{2}I^2 R_E N \tag{4.3a}$$

$$Q_C = \alpha T_C I N + K_{TEG}\left(T_H - T_C\right)N + \frac{1}{2}I^2 R_E N \tag{4.3b}$$

The Peltier heat is defined as $Q_{P,H} = \alpha T_H I$ at the hot side, $Q_{P,C} = \alpha T_C I$ at the cold side and Joule heating, $Q_J = I^2 R_E$ reduces the temperature difference at the hot side and increases the temperature difference at the cold side [36]. These equations represent a lumped model of the spatially distributed effects within the TEG. K_{TEG} is the thermal conductance of the TEG module when there is no current flow and N is the number of TEGs in each CV. From these equations, it is observed that the current flowing through the TEG affects the temperature difference across the TEG

(Figure 4.3). Subtracting Q_C from Q_H the power output, P is derived as

$$P = \alpha(T_H - T_C)I - I^2 R_E. \tag{4.4}$$

If the TEGs are connected electrically in series, then the output voltage of each TEG is summed to calculate the power as

$$P = I \sum (V_{oc} - IR_E). \tag{4.5}$$

A transient model may be created by adding heat capacity to each component (HEXs, exhaust gas, cooling fluid) for each equation described above and solving [43]

$$MC_p \frac{dT}{dt} = Q_{in} - Q_{out} \tag{4.6}$$

where M [kg] is the mass of the component in the CV, $\frac{dT}{dt}$ is the temperature rate of change in the CV, Q_{in} and Q_{out} are the heat transfer rate into and out of the CV, respectively. Transient models for TEG WHR have been implemented by [50, 103]. The TEG can assume negligible heat capacity since its electrical response time is magnitudes faster than the thermal response of the system and considered relatively instantaneous [22, 23]. Hussain et. al [117] developed a 1-D lumped mass transient model to investigate the potential of TEGs in a hybrid vehicle. Their simulation results indicated a 300-400W power generation for a 2.5L hybrid vehicle under a highway drive cycle.

4.2 Module Modeling

A model was developed to predict the performance of TEG modules depending on the properties of the p-n thermoelectric materials and the geometry of the module, i.e. height and area of the legs. A schematic of the equivalent thermal network for a TEG module is shown in Figure 4.4. The hot side temperature for the module is $T_{cer,H}$ and the cold side temperature is $T_{cer,C}$ which are the temperatures of the ceramic plates. However, if the module is placed between two surfaces such as heat exchangers, a temperature drop will occur from T_H to $T_{cer,H}$ due to the contact resistance (ct) between the surfaces; the same effect is observed for the cold side.

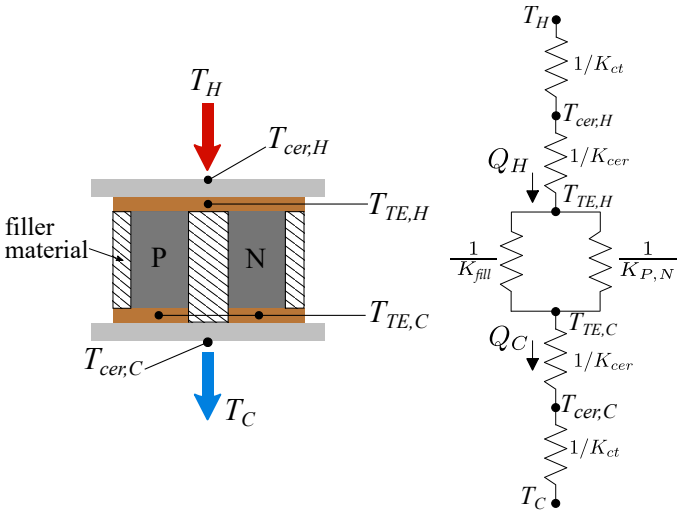

Figure 4.4: P-N schematic and equivalent thermal circuit

Heat is transferred from the hot side to the cold side and considering negligible thermal resistance due to the electrical contacts an energy balance will result in

$$K_{ct}\left(T_H - T_{cer,H}\right) = K_{cer}\left(T_{cer,H} - T_{TE,H}\right) = Q_H, \tag{4.7}$$

considering the Peltier heat and Joule losses the heat through the hot side, Q_H is defined as

$$Q_H = \alpha T_{TE,H} I n + K_{TEG} \left(T_{TE,H} - T_{TE,C}\right) n - \frac{1}{2} I^2 R_E n \tag{4.8}$$

where n is the number of thermocouples in the module and $T_{TE,H}$ is the temperature of the hot side TE junction; it is equivalently defined for the cold side. The Seebeck coefficient, α_m, is defined at the mean temperature of the thermoelectric elements: $\frac{(T_{TE,H} - T_{TE,C})}{2}$. K_{TEG} represents the equivalent thermal conductance of both the p and n legs as well as the conductance of the gap between them which are thermally in parallel, which can either be air or a filler material. Therefore K_{TEG} is calculated as

$$K_{P,N} = K_P + K_N \tag{4.9a}$$

$$K_{TEG} = K_{P,N} + K_{fill} \tag{4.9b}$$

Heat through the cold side is then similarly defined as

$$Q_C = \alpha T_{TE,C} I n + K_{TEG} \left(T_{TE,H} - T_{TE,C}\right) n + \frac{1}{2} I^2 R_E n \tag{4.10}$$

and completing the energy balance

$$K_{cer} \left(T_{TE,C} - T_{cer,C}\right) = K_{ct} \left(T_{cer,C} - T_C\right) = Q_C. \tag{4.11}$$

The internal electrical resistance, R_E is the sum of the electrical resistances within the module which consist of: the electrical resistance of the p and n legs ($R_{P,N}$), the electrical resistance of the contactors (R_{ctr}), and the contact electrical resistance (R_{ct})

which are all defined as

$$R_{P,N} = \frac{L_P}{\sigma_P A_P} + \frac{L_N}{\sigma_N A_N} \tag{4.12a}$$

$$R_{ctr} = \frac{2L_{ctr}}{\sigma_{ctr} A_{ctr}} \tag{4.12b}$$

$$R_{ct} = 2R_e \left(\frac{1}{A_{ct,P}} + \frac{1}{A_{ct,N}} \right) \tag{4.12c}$$

$$R_E = R_{P,N} + R_{ctr} + R_{ct}. \tag{4.12d}$$

4.2.1 Validation- TEM Tester

Validation of the TEG module model was performed by characterizing a low temperature Bismuth Telluride TEG module. To complete the characterization, a temperature difference must be imposed across the TEG and an electrical load connected to observe the power generated as a function of current. The TEG Module (TEM) experimental test rig used for characterization is seen in Figure 4.5. A TEG module is compressed between two copper blocks with equal cross-sectional area. The hot block has heaters that are controlled to maintain the TEG hot side at a specified temperature. Fins are machined into the cold block and are cooled by a chiller. A force is applied to a bolt that is screwed into the cold block to maintain a fixed pressure on the TEG module. A load cell is used to measure the pressure applied to the TEG module. All the tests are completed at 530kPa which is recommended by the TEG module datasheet.

The TEG module and copper blocks, which sandwich the module, are placed in a vacuum chamber to ensure there are no convective heat losses from the blocks to the environment. Since the hot block experiences high temperatures, a radiation shield is

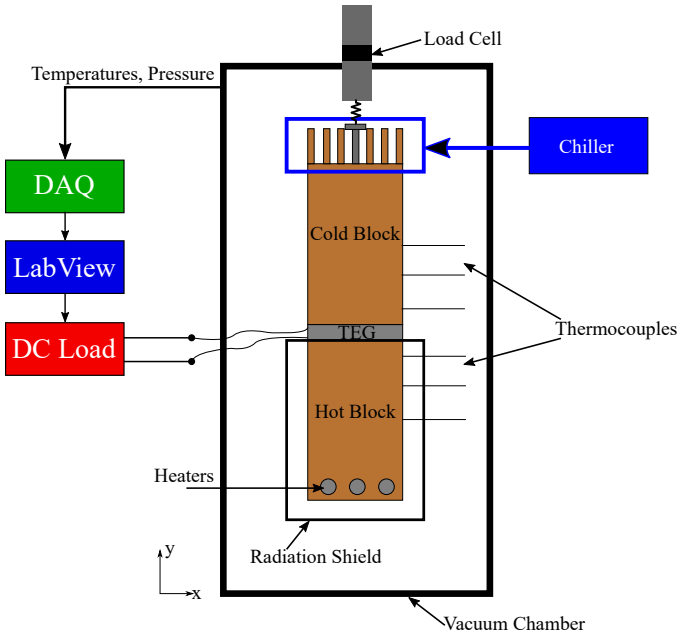

Figure 4.5: Schematic of experimental setup for electro-thermal characterization (not drawn-to-scale).

placed around the block to reduce thermal losses in vacuum. Thermocouples (TCs) are placed along the axial direction (y-axis in Figure 4.5) of both copper blocks to record the temperature gradient. A TC is not placed between the blocks and the TEG module to directly measure T_H and T_C as this creates a hot spot and incorrect temperature measurements may result. At steady-state, a temperature distribution exists only in the axial direction and T_H is derived from

$$T_H = T - \frac{L}{kA}Q \tag{4.13}$$

where T is the temperature reading of the closest TC to the TEG module, L is the distance between the TC and the TEG, k is the thermal conductivity of the copper block, and A is the cross-sectional area of the block which is equal to that of the

TEG module. Q is the heat flux through the block which is calculated from the other TC readings at steady-state. The same calculation is done to calculate the TEG cold side, T_C. When there is no current flowing through the TEG, Q_H should be equal to Q_C or similarly the heat rate through the hot copper block should be equal to the heat rate through the cold copper block. Experiments performed in this test rig showed that this is true within 5% error depending on the temperature across the TEG module.

A DC load is connected to the TEG module to vary the current for the characterization. A DAQ interfaced with LabView is used to control the current imposed on the TEG, as well as the temperature difference across the TEG. The experimental characterization was performed as follows: 1) Set current, 2) PID control of heaters to fix T_H, 3) chiller setpoint is changed to achieve desired T_C, 4) wait until steady-state is achieved and record data. This is repeated until the full V-I from the TEG module is achieved. From the tester the following can be measured: T_H, T_C, R_E, K_{TEG}, and α, the effective properties for a TEG module as well as the power produced as function of electrical current. The characterization results for a Bismuth Telluride module and the model validation are presented next.

4.2.1.1 Validation– Bismuth Telluride Modules

An off-the-shelf TEG module TEG1-12610-5.1 was characterized from TECTEG MFR. The experimental results of V-I curve are presented in Figure 4.6 below and are plotted against the TEG module model results. The material properties for Bismuth Telluride are well known, however the contact resistance needed to be interpreted.

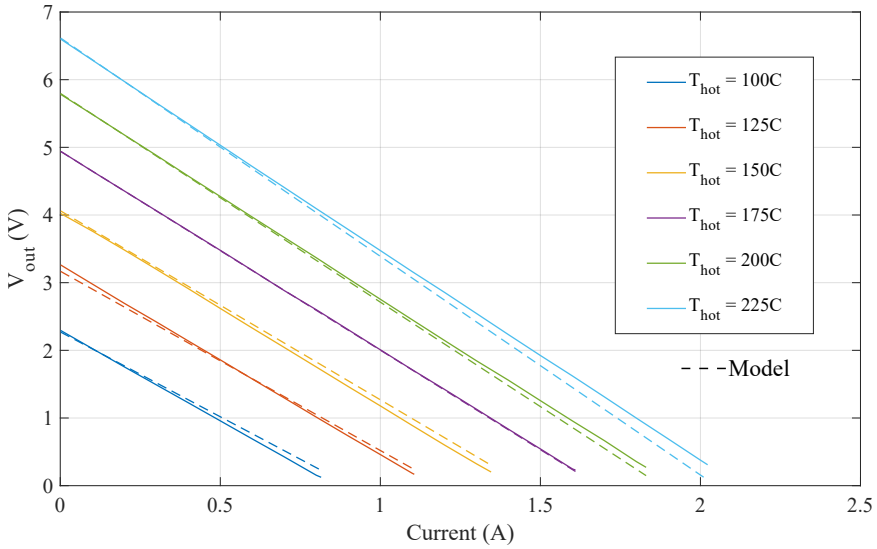

Figure 4.6: Comparison of experimental results for V-I curve to prediction by module model for varying T_H with a fixed T_C=35°C.

As can be observed from the plot, at higher temperature and current, the error increases. This may be because the internal electrical contact resistances are not known and a value was used within the range of what is reported in the literature. At higher current and higher T_H, more heat is conducted through the module and it was previously reported that the TEM tester has an error of 5% at these higher heat fluxes. Therefore there is validity in the developed TEG module model and it can be used proceeding forward.

4.3 System Modeling– Steady-State

A steady-state electro-thermal model was developed for a typical TEG WHR system design. Most common designs have a hot HEX in the center with TEGs on the top and bottom surface to increase the heat transfer area. A cold heat exchanger is mounted on the top and bottom to complete the thermal circuit as shown in Figure 4.7 (a). The

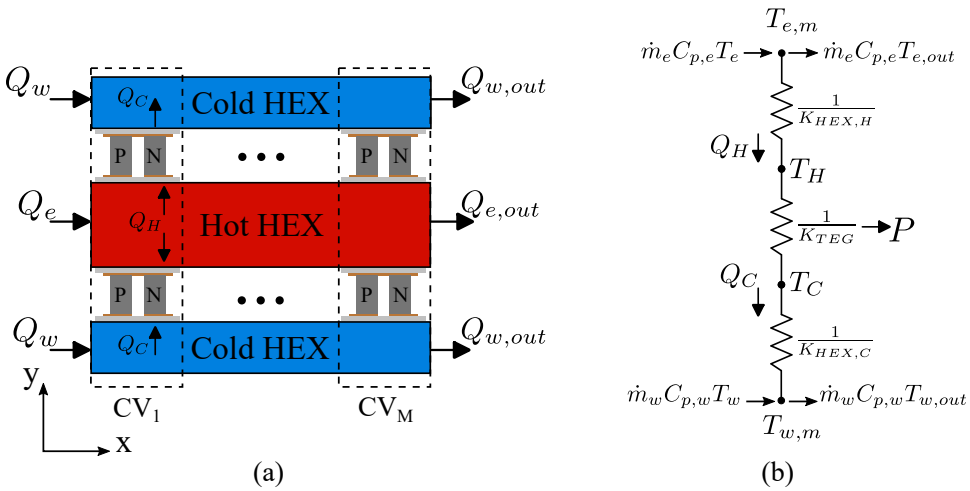

Figure 4.7: (a) Schematic of typical TEG WHR system layout (b) Equivalent thermal network model for TEG WHR system.

equivalent thermal network for heat transfer in the y-direction is shown in Figure 4.7 (b). A 2-D thermal model can be developed by considering heat transfer in the x-direction as well; as the exhaust gases travel downstream, less energy is available for the TEGs in this location.

Considering a simplified thermal network, 4 nodes can be used to represent the TEG WHR system in the y-direction: the average exhaust temperature, $T_{e,m}$, the average coolant temperature, $T_{w,m}$, and the TEG temperatures T_H and T_C. The thermal network can then be expanded in the x-direction depending on the number of TEG rows, M, in the direction of exhaust flow. Therefore, the total number of nodes in the system is $4 \times M$. The number of TEG modules in the z-direction is N and it is assumed that they are all the same temperature, hence the model considers only 2D heat transfer.

Performing an energy balance on the exhaust gases in the first control volume

(CV_1) in Figure 4.7, results in

$$\dot{m}_e C_{p,e} \left(T_e - T_{e,out}\right) = K_{HEX,H} \left(T_{e,m} - T_H\right) = Q_H \tag{4.14}$$

where Q_H is defined by (4.3a) and $T_{e,m} = {}^1\!/_2 \left(T_e + T_{e,out}\right)$. The inlet temperature of the next CV will be the exit temperature of the first one and so on. The same approach is taken by performing an energy balance on the coolant node

$$\dot{m}_w C_{p,w} \left(T_{w,out} - T_w\right) = K_{HEX,C} \left(T_C - T_{w,m}\right) = Q_C \tag{4.15}$$

where Q_C is defined by (4.3b) and $T_{w,m} = {}^1\!/_2 \left(T_w + T_{w,out}\right)$. Therefore T_H and T_C can be solved for any desired current value. The power output is then calculated from (4.4) where the TEG current is determined based on the electrical connection of the TEGs: series or parallel.

4.3.1 Validation–TEG POWER

The TEG POWER system developed in Professor Cotton's research laboratory is used to validate the developed steady-state model. The TEG POWER system was designed to harvest energy from the exhaust gases of a pizza oven and to convert part of that energy to electricity, while the rest of the exhaust heat is used for heating water. The TEG POWER system consists of 4 modular units as shown in Figure 4.8 (a) and (b). A flat-plate fin heat exchanger is implemented to extract thermal energy from the exhaust gases. 6 TEGs are placed on the top and bottom of each HEX unit, consisting of two TEG rows in the exhaust flow direction (3 per row) as shown in Figure 4.8 (c) for a total of 48 TEGs. A jet-impingement cooling design is used as

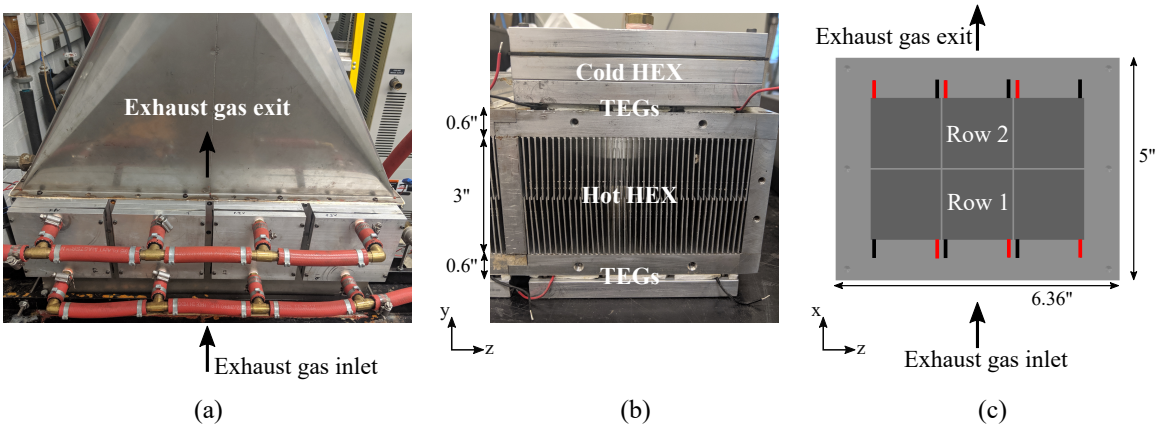

Figure 4.8: (a) TEG POWER system installed on pizza oven (b) modular unit of TEG POWER system. (c) top view of TEG POWER unit

the cold side HEX and is mounted on top and bottom of the modular unit.

Experiments were performed on the TEG POWER system at various exhaust flow rates and temperatures to examine the power produced. The TEG hot side and cold side temperature were measured during the experiments as well as the exhaust gases exiting the HEX and the coolant temperature in the outlet manifold. The TEGs in the system are connected in a combination of both series and parallel electrical configuration. The first and second row of TEGs are connected electrically in series and those 24 TEGs are then connected in parallel with the bottom 24 TEGs as depicted in Figure 4.9. A DC load is connected to the TEGs to control the power output of the system. More in-depth information regarding the test setup of the TEG POWER system as well as the uncertainty of the experimental data can be found in [118].

The developed steady-state thermal model in Section 4.3 was updated to include additional nodes to model the base of both HEXs since the TEG POWER system has a thick base of 0.6” as shown in Figure 4.8 (b). The updated thermal network for the

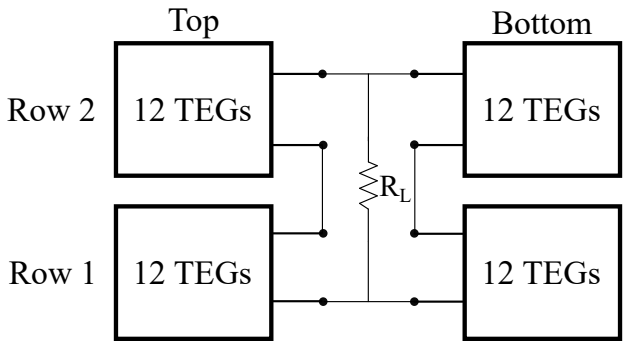

Figure 4.9: Electrical configuration of TEG POWER. Row 1 and Row 2 are connected in series and are then connected in parallel to the symmetric bottom part of TEGs.

TEG POWER system is shown in Figure 4.10, heat conduction is modeled in both the x and y direction for the HEX bases. The boundary conditions to validate the developed thermal model, which were experimentally measured on the TEG POWER system, are given in Table 4.1.

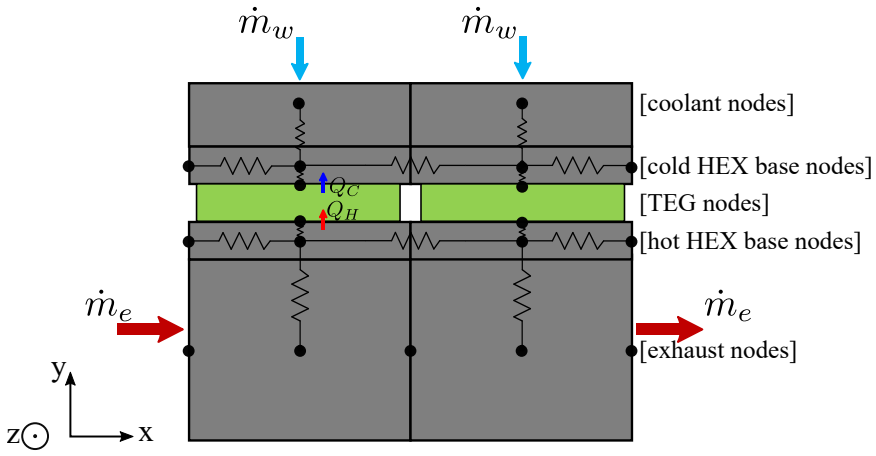

Figure 4.10: Node network for TEG POWER system

Due to symmetry in the TEG POWER system, only a single unit of the modular system was modeled and the power output calculation is manipulated accordingly. Therefore, the exhaust flow rate that was measured during the experiments is divided by 4 when used as a boundary condition for the model. By assuming that the exhaust

flow splits evenly across each of the parallel flat plates in the hot HEX, the thermal conductance can be calculated by using a heat transfer correlation for flow through a rectangular duct. To determine which type of correlation to proceed forward with, the Reynolds, Re, number must be evaluated

$$\mathrm{Re} = \frac{\rho V D_h}{\mu} \tag{4.16}$$

with the exhaust properties calculated at $T_{e,m}$. V is the velocity of the fluid entering a single channel in the parallel plate HEX, D_h is the hydraulic diameter of the duct and is defined as $D_h = \frac{4A_c}{P}$. For all the flow rates given in Table 4.1, the flow is calculated as laminar in each channel: Re<2300. The average Nusselt number, Nu, is constant and equal to 6.4 for laminar flow through a rectangular duct with a uniform surface calculated at the aspect ratio of the channels [119].

The heat transfer coefficient, h can now be calculated by

$$\mathrm{Nu} = \frac{hD_h}{k_e} = 6.4 \tag{4.17a}$$

$$h = \frac{6.4k_e}{D_h} \tag{4.17b}$$

and the thermal conductance of the hot side HEX is calculated as

$$K_{HEX,H} = \eta_o h A_H. \tag{4.18}$$

The overall surface efficiency, η_o, of the HEX is calculated as

$$\eta_o = 1 - \frac{N_f A_f}{A_H}\left(1 - \eta_f\right). \tag{4.19}$$

N_f is the total number of fins in the HEX unit, A_f is the total area of the fins and the total heat transfer area of the hot HEX, A_H, includes the base area of the HEX as well: $A_H = N_f A_f + A_b$. The fin efficiency, η_f, of a single fin is defined as

$$\eta_f = \frac{tanh(mL_c)}{mL_c} \tag{4.20a}$$

$$L_c = L_f + \frac{t_f}{2} \tag{4.20b}$$

$$mL_c = \left(\frac{2h}{k_{HEX} t_f}\right)^{1/2} L_c. \tag{4.20c}$$

L_f is the length of the fin, t_f the thickness of the fin and k_{HEX} is the thermal conductivity of the hot HEX, which in this case is made out of Aluminum.

The cold-side HEX consists of water jets impinging on top of each TEG, therefore there are 48 jet orifices, each has a diameter of 3mm. The heat transfer coefficient for a single impinging jet in this system can be calculated from the Nusselt correlation [120]

$$\mathrm{Nu} = 0.3276\,\mathrm{Re}^{0.4225}\,\mathrm{Pr}^{1/3} \tag{4.21a}$$

$$h = \frac{\mathrm{Nu}\,k_w}{D_h} \tag{4.21b}$$

where the hydraulic diameter in this case is the jet diameter. The thermal properties of the coolant, water, are calculated at $T_{w,m}$. The thermal conductance of the cold side is then calculated as

$$K_{HEX,C} = hA_C \tag{4.22}$$

where A_C is the area of the cold side heat exchanger perpendicular to the jet impingement. The coolant flow rate measured in Table 4.1 splits across all 48 jets, so

the appropriate boundary condition is applied to the model.

Now that $K_{HEX,H}$ and $K_{HEX,C}$ have been calculated for the TEG POWER system, these values can be plugged back into (4.14) and (4.15), respectively. The final variables required to solve for the temperature distribution of the TEG POWER system are the TEG module properties. The TEM tester, discussed in Section 4.2.1, was used to measure the thermal conductance, internal electrical resistance and Seebeck coefficient for the average value of T_H and T_C, respectively, in Table 4.1. K_{TEG} is 0.614 W/K, R_E is equal to 3Ω and α is equal to 0.0345 V/K at the average temperature values measured. Inputting all these values into the system model, T_H and T_C can be solved for and therefore the power produced by the system as a function of current ((4.4)). During the steady-state experiments on the TEG POWER system,

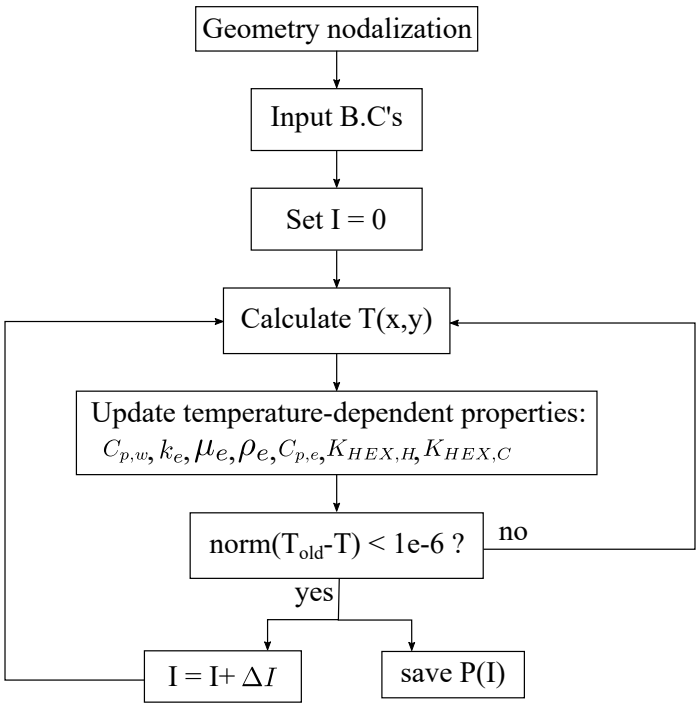

Figure 4.11: Flow chart for steady-state thermal model solution scheme.

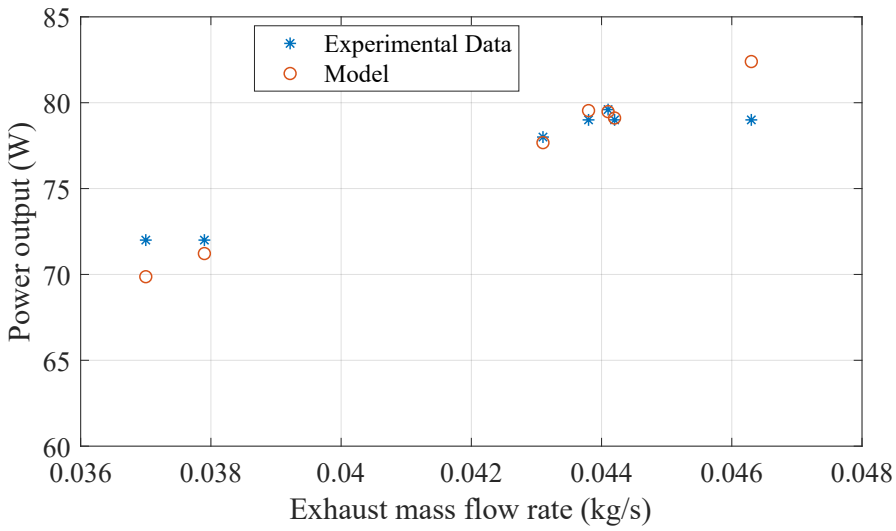

Figure 4.12: Steady-State power output model prediction compared to experimental power measured as function of exhaust mass flow rate.

the DC load was adjusted until the maximum power was outputted by the system. Therefore, the model accordingly sweeps through different current values solving for the temperature distribution within the system and the power produced. A flow chart indicating how the solution is programmed into MATLAB is produced in Figure 4.11. The maximum power from this array of solutions is chosen as the solution to compare to the experimental results.

The results for the predicted maximum power of the developed steady-state thermal model are compared with the experimental results in Figure 4.12 as a function of the exhaust mass flow rate. The results match well and there is a maximum error between the model and the measured experimental power output of 4.3% for the maximum flow rate case. The predicted temperature of the TEG modules at the electrical current value which maximizes the power produced is plotted in Figure 4.13 and compared to the measured TEG temperatures, T_H and T_C. The maximum error is 0.86% for T_H and 3.3% for T_C.

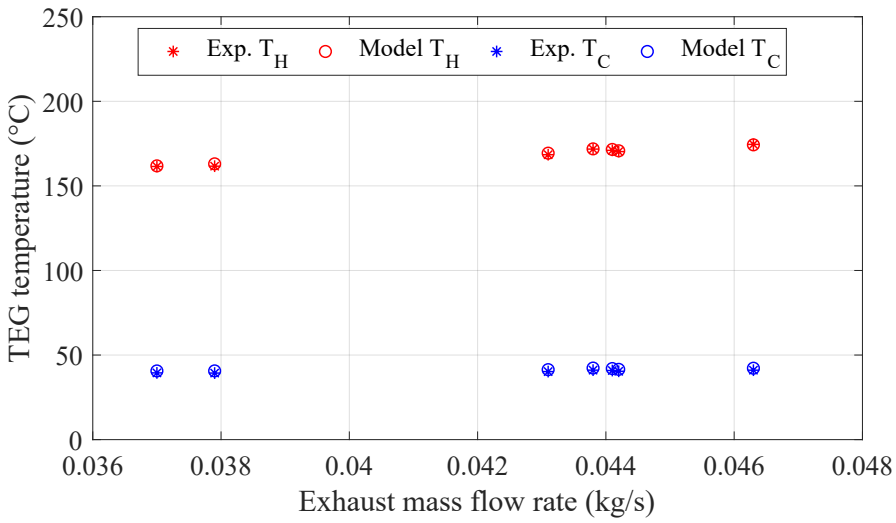

Figure 4.13: Steady-state model prediction of TEG temperature, T_H and T_C, compared to experimental results.

Finally, the temperature of the exhaust gases exiting the hot HEX were measured as well as the coolant temperature in the outlet manifold of the impinging jets. The predicted temperature of the exhaust exiting the hot HEX is compared to the experimental results in Figure 4.14 and the maximum error is 5.78%. Similarly, the results of the coolant temperature exiting the jet manifold compared to the measurements is found in Figure 4.15, where the maximum error is 6.05%. The tabulated errors for model compared to the experiments is found in Table 4.1 for all the measured data points.

Since the model results agree well with the experimental data, the maximum error is 6% for all parameters compared, the validated model can be used to study different effects. Particularly, how the system size and the implementation of MPPT affects the power produced. In the TEG POWER system the maximum power was found for the entire system, rather than bundling the TEG modules into subsystems based on those that operate electrically more closely to each other.

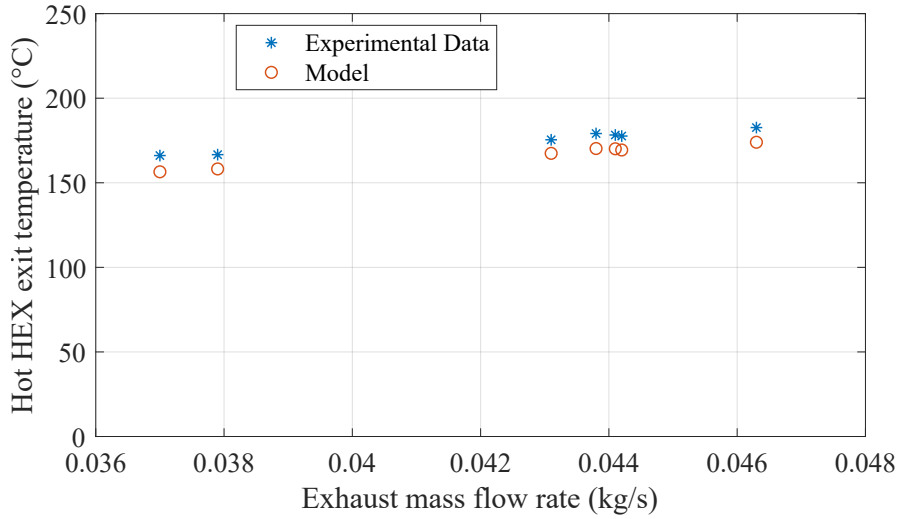

Figure 4.14: Steady-state model prediction of Hot HEX exhaust exit temperature compared to experimental results.

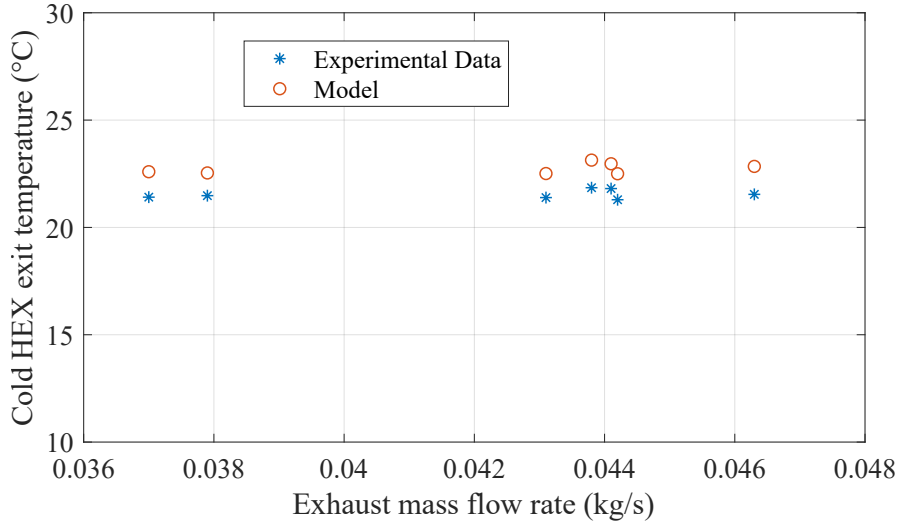

Figure 4.15: Steady-state model prediction of Cold HEX coolant exit temperature compared to experimental results.

Table 4.1: Boundary conditions for TEG WHR system model and comparison of model results to experimental data.

Boundary Conditions				Power	T_H	T_C	$T_{e,out}$	$T_{w,out}$
T_e $[°C]$	$\dot{m}_e$ $[kg/s]$	T_w $[°C]$	$\dot{m}_w$ $[kg/s]$	error [%]	error [%]	error [%]	error [%]	error [%]
265.70	0.0463	8.00	0.07	4.30	0.15	2.85	4.75	6.05
265.58	0.0438	8.09	0.07	0.68	0.07	3.00	4.95	5.88
264.75	0.0441	8.32	0.07	0.15	0.31	2.86	4.56	5.30
263.61	0.0442	7.80	0.07	0.14	0.28	2.82	4.64	5.69
263.19	0.0431	7.96	0.07	0.42	0.54	2.87	4.57	5.24
262.81	0.0379	8.61	0.07	1.09	0.86	3.30	5.07	4.93
262.73	0.0370	8.52	0.07	2.96	0.22	2.94	5.78	5.53

4.3.2 System Size Investigation

The validated steady-state TEG WHR system model is used to investigate the effect of number of TEG modules on the power produced by the system, as well as the effect of implementing MPPT. The TEG POWER system presented in the previous section consisted of 4 modular units made up of two TEG rows (Figure 4.8) and in this study the same configuration is kept, but additional TEG modules are added in both the z-direction (isothermal) and x-direction of Figure 4.10.

The boundary conditions used in this investigation are $T_e = 264.7$°C, $\dot{m}_e$ =0.0441 kg/s, T_w=25°C, and $\dot{m}_w$=.07 kg/s. These boundary conditions are the same as one of the experiments in the TEG POWER system and are chosen because they had the lowest error in the validation.

As more TEG modules are added to the system, the electrical configuration is kept the same as the original TEG POWER system, where all the rows are connected electrically in series and the top and bottom units are connected in parallel (Figure 4.9) with a single MPPT for the entire system. The original system had 4 modular units and in this investigation the power of the system is predicted for a single unit up

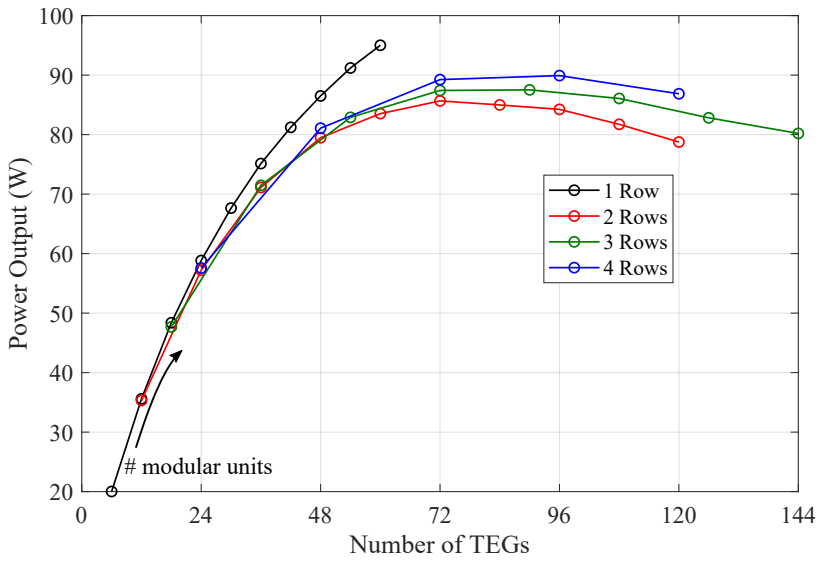

Figure 4.16: The power output by a TEG WHR system as more TEG modules are added in the direction of exhaust flow (x-direction) and perpendicular to the exhaust inlet (z-direction).

to 10 units in the z-direction. Since the model is 2D, considering heat transfer in the x and y-direction only, it is assumed that the exhaust flow splits evenly across the z-direction between all the hot HEX units. As more TEG rows are added in the x-direction, the hot HEX length gets longer to accommodate for more TEG modules and more impinging jets must be added as well. The results for the electrical power produced as the number of TEG modules increases for 1-4 TEG rows is plotted in Figure 4.16. Each data point on a line of rows represents the addition of another modular unit.

As can be observed, from Figure 4.16, the power produced for a single row of TEGs with at least 5 modular units is greater than the configurations with more than one row. The single row configuration has a higher power output because all the TEGs in that row have the same temperature. However, the TEGs in the multirow system are at different temperatures (downstream ones have lower ΔT), but they are

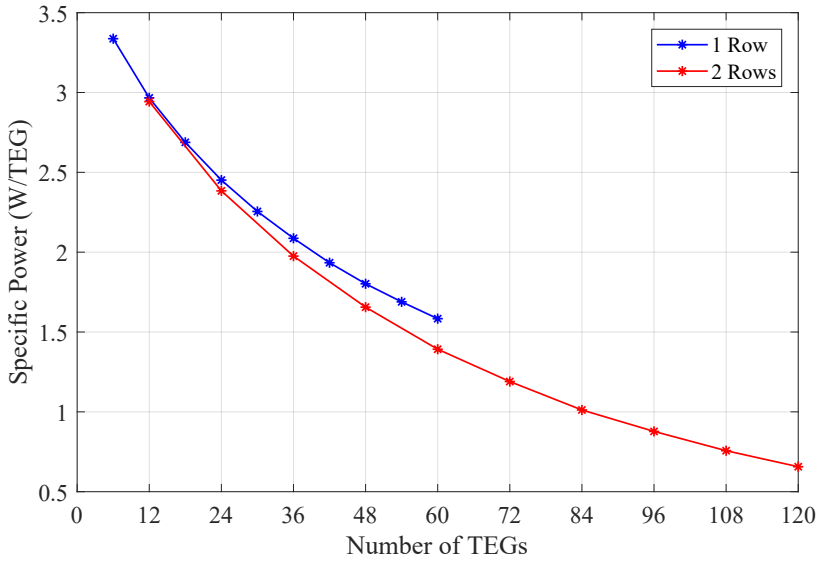

Figure 4.17: The specific power of each TEG module as more TEG modules are added to the system.

still connected electrically in series. Furthermore, the specific power per module can be plotted to understand the degradation in power produced by the system as more rows are added, which is seen for two TEG rows in Figure 4.17. It should be noted though, that it may not be ideal to keep increasing the number of TEG WHR units in the z-direction (perpendicular to exhaust flow) since this would entail a large inlet manifold and the model does not consider any entrance effects.

Typically, the available space where a TEG WHR system needs to be installed, such as the undercarriage of a vehicle, is limited. Therefore the cross-sectional area of the inlet should be fixed (z-direction) and it is of interest to understand how the power is affected only as the number of TEG rows increases. Therefore, Figure 4.18 may be observed where the power curves are instead created for a fixed number of modular units and only the TEG rows are allowed to increase.

Thus far, the power produced by the system has been considered with all the

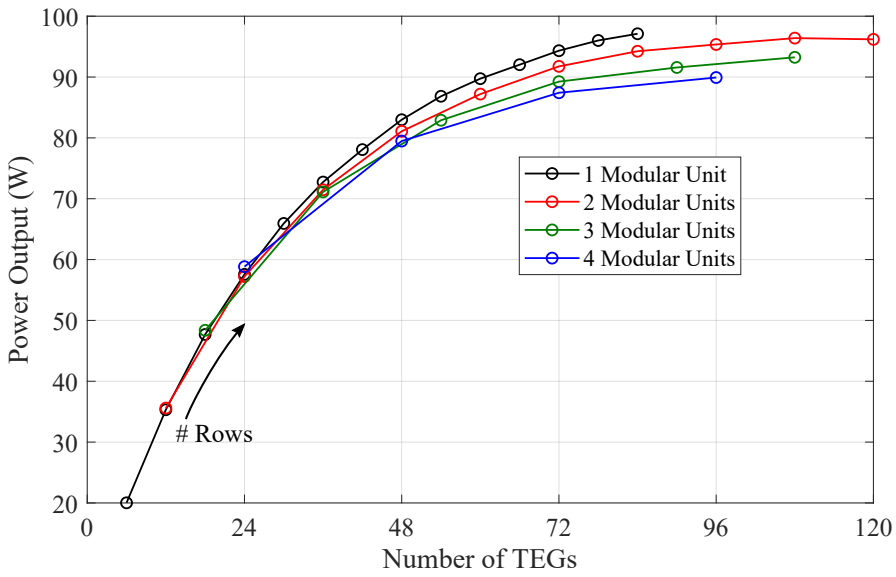

Figure 4.18: A degradation in power output is observed as more units are added to the system in the direction perpendicular to exhaust flow.

TEG rows connected in series and a single MPPT, but the TEG modules can now be separated into different bundles each with their own MPPTs to optimize their electrical operating condition. For clarity, the following example will only focus on comparing the performance of a system with 2 and 4 modular units, where only the number of TEG rows keeps increasing. The reference case for the TEG WHR system with 2 and 4 modular units with a single MPPT is shown in Figure 4.19. Each data point on the curve represents an additional TEG row, for a total of 8 TEG rows.

As more TEG rows are added to the system, the TEG modules operate at different temperatures since less energy is available in the exhaust gases due to heat transfer to the upstream TEGs first. Therefore, it is worth investigating if the power output can be increased by having each TEG row operate with its own MPPT. Operating with its own MPPT equates to each row of TEGs operating at a specific electrical current value such that that maximum power is produced from that row compared

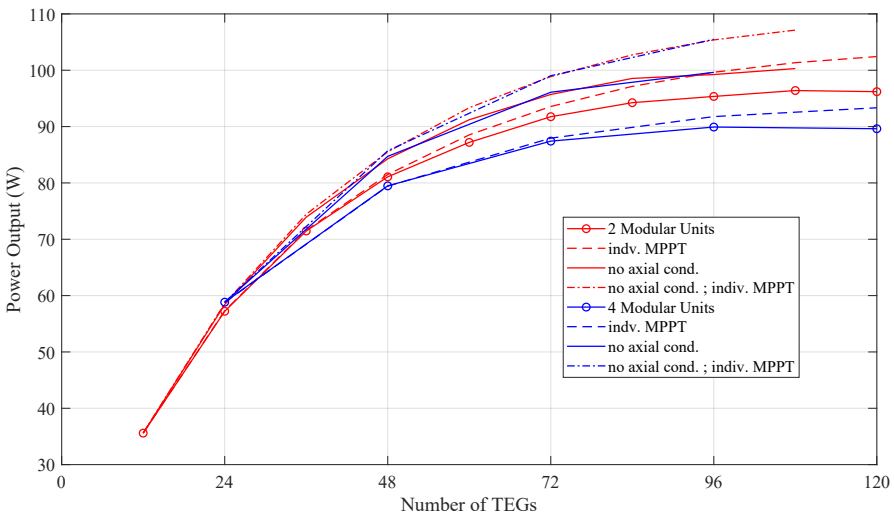

Figure 4.19: Comparison of power output: 1) Reference case with single MPPT for all rows, 2) MPPT is added per row, 3) axial conduction is turned-off 4) both axial conduction is off and an MPPT is added per row.

to the reference case where the same current is going through all the TEGs. In Figure 4.19, it can be seen that the power slightly increases for both systems when each row operates with its own MPPT. Next, consider turning-off axial conduction in the bases of the HEX's, which would prevent any heat from the first TEG row to conduct axially to the next TEG and hence, the first TEG row will operate at a hotter temperature. As can be observed in Figure 4.19, by the solid lines without any markers, the power significantly increases, especially for the larger 4 unit system. Lastly, the power produced by the system is observed if both axial conduction is turned-off and each row of TEGs operates with their own MPPT. It is observed that the power output is the equal for the same number of TEGs if both axial conduction and individual MPPTs are implemented.

In this particular configuration studied with the given boundary conditions, it would not make sense to operate each row with its own MPPT since the power

increase is minimal. Adding an MPPT for each TEG row would entail including an additional power converter which would increase cost and complexity and from the results presented in Figure 4.19, it is not practical. However, if it is possible to thermally isolate the TEG rows from one another such as implementing grooves in the HEX bases, then the power could potentially increase in this design by 7.6% in the 4 unit system with 48 TEGs.

It is also interesting to note that a new optimum is reached if axial conduction is turned off compared to the case where there is axial conduction in the HEX bases. A degradation in power output still exists in all the cases investigated because the coolant flow rate is fixed, which means that as more TEG modules are added, the coolant flow rate needs to be divided by a larger number of jets so the TEG cold side temperature increases with the addition of each TEG. Now that a degradation in power has been observed by studying different system sizes and indicating that an optimum system design point exists, a transient model of the system will be developed. The TEG WHR system which will be installed in a vehicle will operate under real driving conditions such as drive cycles which are transient in operation.

4.4 System Modeling- Transient Model

Now that the steady-state model has been developed and validated through experiments, a further step is taken to develop a transient model which considers thermal capacity of the WHR system. A transient model is necessary to examine the power output during vehicle drive cycles, where the operating conditions are continuously changing and are realistic of real vehicle operation. The energy equation may be

written as

$$MC_p \frac{dT_i}{dt} = q_{x,in} - q_{x,out} + q_{y,in} - q_{y,out}. \tag{4.23}$$

for a control volume, CV, with mass M and specific heat, C_p. The thermal capacitance (MC_p) times the rate of change of temperature with respect to time, $\frac{dT}{dt}$, is equal to the difference in energy flowing into and out of the CV.

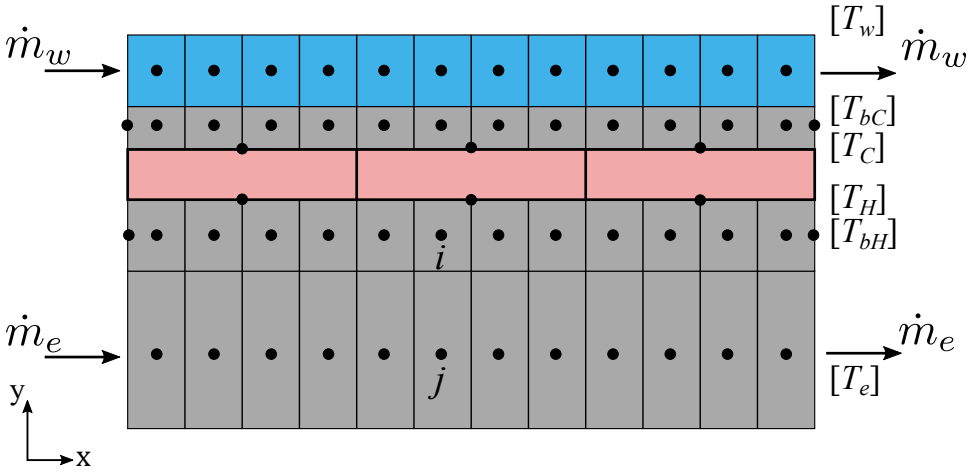

Figure 4.20: Schematic of nodalization in TEG WHR system for transient analysis.

The TEG WHR system was nodalized as shown in Figure 4.20 and a Finite Volume Method (FVM) approach was implemented to solve for the transient temperature response of the system. The unknown temperatures in the system are the exhaust temperature flowing through the HEX, in vector form $[T_e]$, the hot side and cold side HEX base temperatures $[T_{bH}]$, $[T_{bC}]$, respectively, the TEG modules temperatures $[T_H]$ and $[T_C]$, as well as the coolant temperature $[T_w]$ throughout the system. Consider performing an energy balance on the HEX base node, i, as seen in Figure 4.20 which results in

$$MC_p \frac{dT_i}{dt} = K_a \left(T_{i-1} - T_i\right) - K_a \left(T_i - T_{i+1}\right) + \left(T_j - T_i\right) K - \left(T_i - T_H\right) K_b. \tag{4.24}$$

Since the system is discretized in both the x and y direction, the mass of the CV is $M = \Delta x \Delta y z$, where z is fixed in this system since it is a 2D transient model. In this case, j represents a node in the exhaust gases, $[T_e]$. The thermal conductance in the x-direction for the HEX base, K_a is defined as

$$K_a = \frac{k_{HEX,H} A_x}{\Delta x}. \tag{4.25}$$

The thermal conductance in the y-direction, K, considers the thermal conductance from both the hot side HEX and the base of the HEX

$$K = \left(\frac{1}{K_b} + \frac{1}{K_{HEX,H}} \right)^{-1} \tag{4.26}$$

The thermal conductance, K_b from node i to node T_H is only the hot side HEX base conductance

$$K_b = \frac{2 k_{HEX,H} A_y}{\Delta y}. \tag{4.27}$$

By implementing the implicit method, the energy balance of (4.24) can be re-written as

$$\begin{aligned} MC_p \frac{T_i^{n+1} - T_i^n}{\Delta t} =& K_a \left(T_{i-1}^{n+1} - T_i^{n+1} \right) - K_a \left(T_i^{n+1} - T_{i+1}^{n+1} \right) \\ &+ \left(T_j^{n+1} - T_i^{n+1} \right) K - \left(T_i^{n+1} - T_H^{n+1} \right) K_b \end{aligned} \tag{4.28}$$

where n is the old time step and $n+1$ is the current time step. Combining like terms

to get the following equation:

$$\left(\frac{MC_p}{\Delta t} + 2K_a + K + K_b\right) T_i^{n+1} - K_a T_{i-1}^{n+1} - K_a T_{i+1}^{n+1} = \frac{MC_p}{\Delta t} T_i^n + T_j^{n+1} K + T_H^{n+1} K_b \tag{4.29}$$

Using an adiabatic boundary condition for the HEX base sides, $q_x = 0$ for the first node as well as the last node, i.e. $i = 1$ and $i = N$.

$$k_{HEX,H} A_x \frac{(T_1 - T_2)}{\frac{\Delta x}{2}} = 0 \tag{4.30}$$

therefore

$$T_1 - T_2 = 0 \tag{4.31}$$

the same applies for the last node

$$T_{N-1} - T_N = 0. \tag{4.32}$$

Let $K_T = \frac{MC_p}{\Delta t} + 2K_a + K + K_b$, then 4.29 can be rewritten as

$$K_T T_i^{n+1} - K_a T_{i-1}^{n+1} - K_a T_{i+1}^{n+1} = \frac{MC_p}{\Delta t} T_i^n + T_j^{n+1} K + T_H^{n+1} K_b, \tag{4.33}$$

and hence (4.33) can be written for every node in the hot side HEX base such that a system of equations is formed in the form of $[A][T_{bH}^{n+1}] = [f(T_{bH}^n, T_e^{n+1}, T_H^{n+1})]$. Therefore, the temperatures of the hot HEX base, $[T_{bH}]$ at the current time step are a function of the old time step, n, and the current temperatures of both the exhaust

gases $[T_e]$ and the TEG hot side $[T_H]$:

$$\begin{bmatrix} 1 & -1 & 0 & 0 & \dots & 0 \\ -K_a & K_T & -K_a & 0 & \dots & 0 \\ 0 & -K_a & K_T & -K_a & \dots & 0 \\ \vdots & \vdots & \ddots & \ddots & \ddots & \vdots \\ \vdots & \vdots & \ddots & -K_a & K_T & -K_a \\ 0 & 0 & \dots & 0 & -1 & 1 \end{bmatrix} \begin{bmatrix} T_{bH,1} \\ T_{bH,2} \\ T_{bH,3} \\ \vdots \\ T_{bH,N-1} \\ T_{bH,N} \end{bmatrix}^{n+1} = \begin{bmatrix} 0 \\ \frac{MC_p}{\Delta t} T^n_{bH,2} + T^{n+1}_{e,2} K + T^{n+1}_{H,1} K_b \\ \frac{MC_p}{\Delta t} T^n_{bH,3} + T^{n+1}_{e,3} K + T^{n+1}_{H,1} K_b \\ \vdots \\ \frac{MC_p}{\Delta t} T^n_{bH,N-1} + T^{n+1}_{e,N-1} K + T^{n+1}_{H,2} K_b \\ 0 \end{bmatrix} \tag{4.34}$$

Next, performing an energy balance on the HEX exhaust node, j, (4.23) becomes

$$MC_p \frac{dT_j}{dt} = \dot{m}_e C_p \left(T_{j-1} - T_j\right) - \left(T_j - T_i\right) K \tag{4.35}$$

by implementing a fully upwind scheme and ignoring axial conduction in the exhaust gases. Once again implementing an implicit scheme to end up with the following

$$\left(\frac{MC_p}{\Delta t} + \dot{m}_e C_p + K\right) T^{n+1}_j - \dot{m}_e C_p T^{n+1}_{j-1} = \frac{MC_p}{\Delta t} T^n_j + T^{n+1}_j K. \tag{4.36}$$

Using the boundary condition of $T_{j=1} = T_{e,in}$ -the inlet condition of the hot side heat exchanger is the exhaust gas temperature of the vehicle. The system of equations can be written with (4.36) for the exhaust gases such that $[A][T^{n+1}_e] = [f(T^n_e, T^{n+1}_{bH})]$.

Now that the matrices for the exhaust gases and hot HEX base nodes have been derived, the temperature of the hot side of the TEG modules can be calculated. Since the electrical response is considered to be magnitudes faster than the temperature response of the TEG [22, 23], negligible thermal capacitance will be considered.

Considering the Peltier and Joule effects, the following is derived

$$NK_b\left(\overline{T}_{i,N} - T_H\right) = \alpha T_H I + K_{TEG}\left(T_H - T_C\right) - \frac{1}{2}I^2 R_E, \tag{4.37}$$

where $\overline{T}_{i,N}$ is the average temperature of the nodes below the hot side of the TEG module and N is the number of nodes. By combining like terms (4.37) becomes

$$\left(NK_b + \alpha I + K_T EG\right) T_H = NK_b \overline{T}_{i,N} + T_C K_{TEG} + \frac{1}{2}I^2 R_E. \tag{4.38}$$

The variable that is unknown in the system is the operating current of the TEGs, I. The model assumes that the maximum power is extracted at every time step, therefore a guess regarding the operating current must first be made and is then updated, iteratively. The short circuit current, I_{sc}, is evaluated from the solved temperature distribution across the TEG module such that $I_{sc} = \frac{\alpha(T_H - T_C)}{R_{int}}$ and then the operating current is set to $I_{sc}/2$. Therefore, the matrix A can be written for the hot side TEG as $[A][T_H^{n+1}] = [f(\overline{T}_{i,N}^{n+1}, T_C^{n+1}]$ with (4.38).

The same procedure can be followed to derive the system of equations for the cold side of the TEG, $[T_C]$, the cold side HEX base $[T_{bC}]$ and the coolant temperature $[T_w]$. Compiling all the governing equations for each component domain, the number of matrices equals the number of components in the system and the size of each matrix depends on how many nodes are chosen to represent each component. To speed up the solution for such a large system of equations, the Tridiagonal Matrix Algorithm (TDMA) is implemented in MATLAB to solve for the temperatures. Since all the equations are implicit, which means they depend on the solution of the current time step to solve for the current time step, i.e. $T_i^{n+1} = f(T_j^{n+1})$, the solution is iterative.

The solution is solved for a time step, dt, and continues to solve for $[T^{n+1}]$ until the solution converges. Convergence at each time step is determined by calculating the energy balance at each node; energy is conserved when (4.29) is balanced, i.e. left-hand side of the equation is equal to the right-hand side of the equation. Once the solution has converged, the temperature values are saved as the old temperature values (T^n), and the solver starts once again. The power produced from the system is calculated based on the temperatures of the TEG modules using (4.4). An overview of how the temperature solution is solved for all the components in the TEG WHR system is shown in Fig. 4.21.

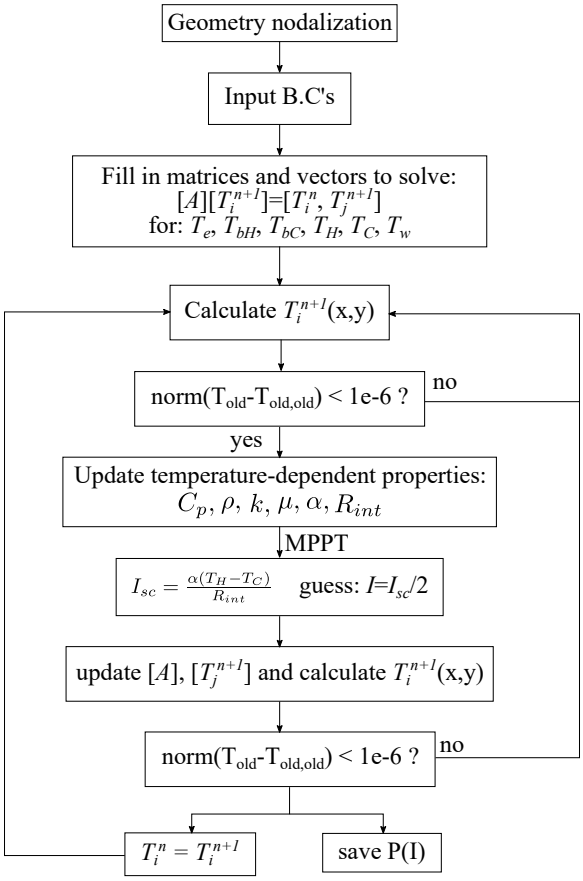

Figure 4.21: Transient model flow diagram explaining how solution is solved.

Determining the appropriate time step, dt, solve the system of equations is based off the Courant number, C, such that

$$C = \frac{u\Delta t}{dx} < 1 \tag{4.39}$$

where u is the velocity of the fluid, either the exhaust gas or the coolant and dx is the size of a single node selected in the discretization of the domain. The selected dt value was checked before starting the computation and was chosen such that even at the highest flow rate in the drive cycle, it would be small enough to satisfy (4.39). This criteria ensures that the fluid particle only transverses one node within one time step.

4.4.1 Model Validation

The developed transient model of the TEG WHR system was validated using the experimental data from [103]. A TEG WHR system with 4 TEG modules was tested in the EGR path of a 6.6L boosted diesel engine and the power output was recorded over a Non-Road Transient Cycle (NRTC) drive cycle. The boundary conditions for validating the model are shown in Figure 4.22, where the exhaust gas temperature and mass flow rate entering the hot side HEX are recorded over time. The 4 TEGs are sandwiched between a hot side HEX and a cold plate as shown in Figure 4.23.

First, the TEG modules, GM250-127-28-10, which were installed in the system were validated against the transient data that was provided in [103]. The TEG module model that was earlier developed in Section 4.2, was used with the experimentally measured T_H and T_C to predict the module voltage output over time. The comparison of the TEG module model prediction versus the experimental data is shown in

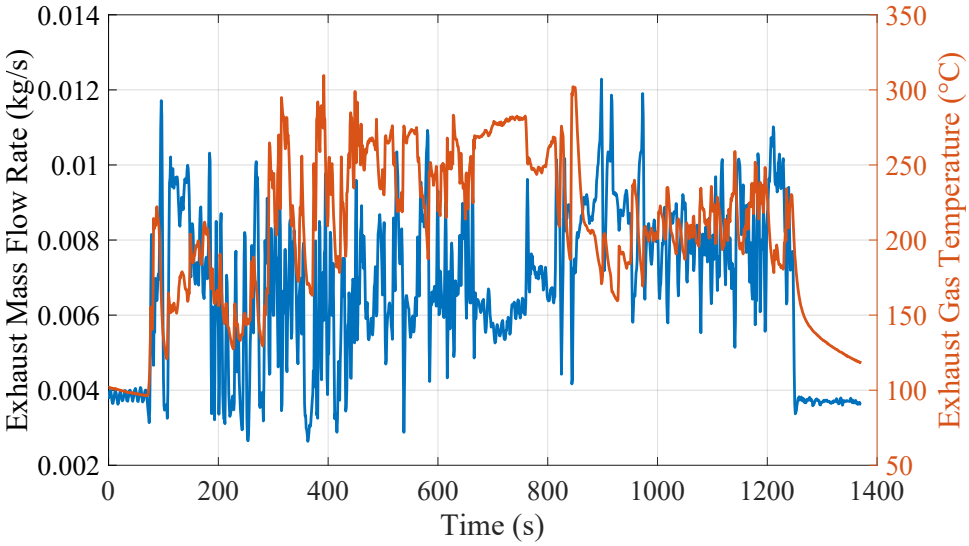

Figure 4.22: Experimental data of the exhaust gases and exhaust temperature at inlet of hot side HEX during the NRTC drive cycle.

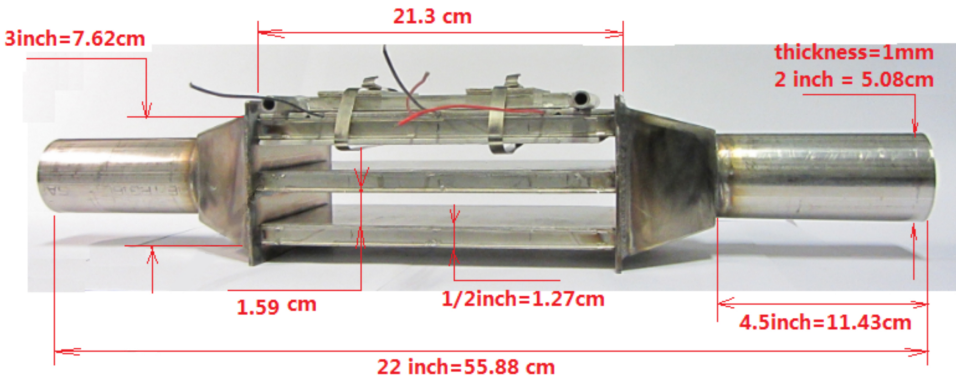

Figure 4.23: Test section for transient tests conducted on engine. The TEG modules are sandwiched between a hot side HEX and two cold side HEXs.

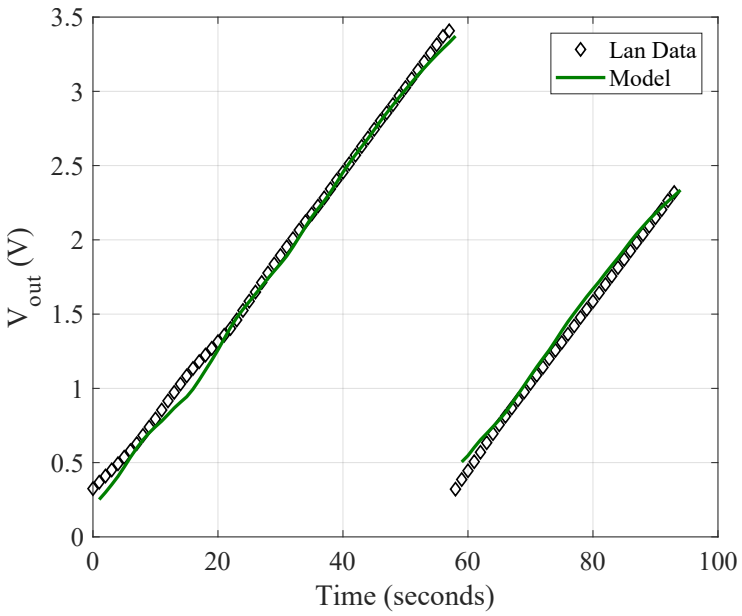

Figure 4.24: Comparison of experimental data from [103] compared to the developed model of the TEG module.

Figure 4.24. The module model is able to predict the output voltage as a function of time for the tested module.

The developed transient model was adjusted based on the configuration of the tested TEG WHR system. In particular, the insulation material that was used between the TEG modules was modeled as shown in Figure 4.25 and the coolant was adjusted for counterflow relative to the exhaust flow. Using the boundary conditions from Fig. 4.22, the transient model predicts the power ouput over a nonroad transient drive cycle and the comparison to the measured power output is shown in Fig. 4.26. As can be observed, the model is able to predict the power output over the imposed drive cycle and the maximum error compared to the experimental data is 1W.

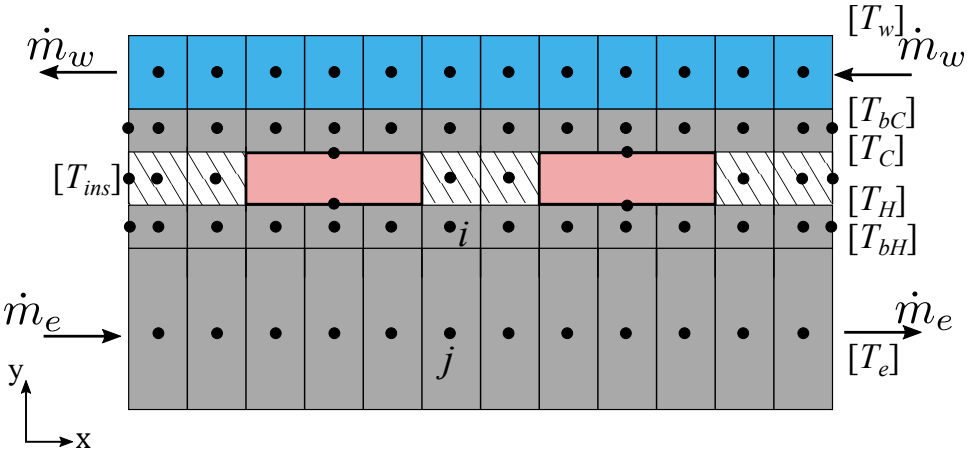

Figure 4.25: Nodalization of TEG WHR system model for validation in engine environment.

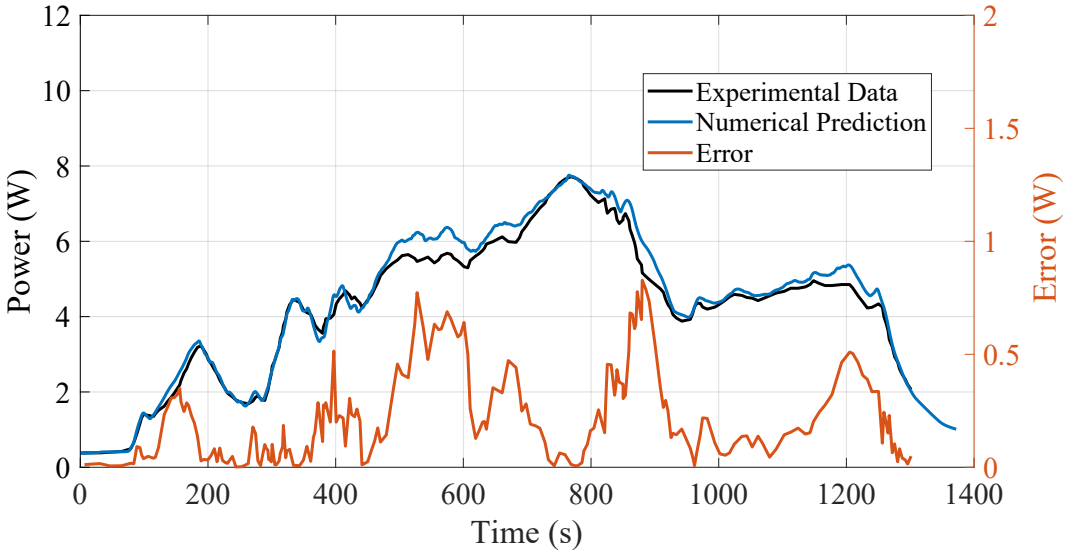

Figure 4.26: The error is reported as the absolute difference between the simulation and the experimental data, as can be observed the error is less than 1W.

Chapter 5

Maximum Power Point Tracking for TEGs

5.1 Motivation

The power produced by a TEG is not only dependent on the thermal operating conditions but also on the electrical load applied. Therefore, a power converter is usually interfaced with the TEGs that are connected either in series or parallel, depending on the desired voltage output of the system. To ensure that the maximum power is produced by the TEG during operation, a Maximum Power Point Tracking (MPPT) scheme is programmed to control the power converter. In waste heat recovery applications such as automotive, the waste heat sources are dynamic in operation, i.e. the exhaust fluids have variable temperature and mass flow rates which determine the amount of heat energy available for harvesting. Unlike other waste heat recovery technologies such as Rankine cycles (i.e. turbo-lag) [11], TEGs can operate robustly in these dynamic environments to recover energy. Consequently, MPPT algorithms

need to be employed that can quickly adapt to these variable operating conditions.

The most commonly used MPPT scheme for TEGs in the literature is the Perturb & Observe (P&O) scheme which works by altering the TEG operation setpoint, observing if the output power increased or decreased and making a decision based on this information [121–124]. The main disadvantage with this method is that the maximum power point (MPP) is not reached, but instead the power output of the TEG oscillates around the MPP. The Incremental Conductance (IncCond) method considers the derivative of the power (derivative is zero at MPP) and changes the setpoint based on this feedback [125–127]. In comparison to P&O, IncCond offers a more robust quantifier on the location of the operation point. Similarly to P&O, IncCond requires a sufficiently large step and keeps moving around the MPP. The fractional open-circuit voltage scheme is another commonly used MPPT method in the literature. It is implemented by setting the current to 0A, measuring the open-circuit voltage of the TEG, and then setting the electrical load to half this value [128–130]. One drawback with this scheme is that the TEG needs to be disconnected from the load to measure the open circuit voltage and hence the dynamics, i.e. the operating condition of the TEG is affected.

This chapter proposes a new MPPT scheme, the High Frequency Injection (HFI) scheme, where a high frequency signal is injected into the system and the perturbation observed is used as feedback to control the operating condition of the TEG and arrive at the MPP, without inducing oscillations to the system. The HFI scheme requires only measurement of the TEG power, hence no additional sensors are needed such as thermocouples and the MPPT can quickly adapt to changes in the system without prior characterization. The proposed scheme is experimentally implemented and the

performance is evaluated through three different experiments, including transient operation. The scheme is also experimentally compared to the most commonly used MPPT scheme, P&O. The following section provides a literature review of the MPPT schemes used on TEGs.

5.2 Review of MPPT Methods

Power converters interface a TEG system with an electric load. In conventional and mild-hybrid drivetrains, the load is the low voltage subsystem that is connected to a lead-acid battery. In hybrid vehicles, the TEG system can also be connected to the high voltage battery. In both cases, an energy storage element is available. Hence, TEG systems are operated independent of any load characteristic (Figure 3.4) and maximize the energy output of the TEG system (Figure 3.3). In rare events, e.g. when the battery is fully charged and the electric load is low, the power is limited by reducing the TEG current I [131, 132]. *Maximum power point tracking* (MPPT) strategies maximize the electric power output for given boundary conditions, that are the heat transfer rate of the hot side and cold side heat exchangers as well as the thermal resistances of the system. MPPT strategies adjust the TEG current I (or alternatively the TEG terminal voltage V_{TEG}) to maximize the electrical power $P = V_{TEG}I$.

The MPP is located at $I_S/2$ (or alternatively $V_{oc}/2$), where I_S is the short circuit voltage of the current, assuming that the open circuit voltage V_{oc} and the resistance R_E are independent of the current. Hence, strategies have been proposed that estimate I_S and the MPP from the measurements referred to as the fractional open-circuit voltage scheme [128–130]. However, the Seebeck coefficient α and the

electric resistance R_E have temperature dependencies as shown in Table 3.3. Hence, peak seeking strategies are gaining popularity. Examples are the *perturb and observe* (P&O) method [121, 124, 133–136], and *incremental conductance* (IncCond) method [125–127].

P&O operates inherently in discrete time where the sampling period T_s is chosen much larger than the electro-thermal time constants. At each time step, P&O varies the current setpoint I by a step ΔI either in positive or negative direction. If the power P has increased compared to the power of the last time step P^-, the setpoint is moved in the same direction. Alternatively, the setpoint is moved in the opposite direction. It is possible to write the concept in compact form as

$$I^+ = I + \text{sign}(P - P^-)\ (I - I^-), \tag{5.1}$$

where $\Delta I = I - I^-$, I^- is the current of the last time step, and I^+ is the setpoint applied in the next period. P&O (sometimes called hill-climb method) is a simple and effective strategy but requires trade-offs when choosing the parameters T_s and ΔI. A large T_s increases the time of convergence to the maximum power point. A small T_s increases the risk that electro-thermal dynamics distort the power measurement due to stored energy and prevent P&O from identifying the steady-state peak. Furthermore, a sufficiently large ΔI is required that prevents measurement noise from affecting the power measurement. Ultimately, P&O identifies the MPP with suitable parameters but keeps moving around the MPP. In practice, this operation is typically acceptable since the MPP is a flat optimum.

The IncCond method is based on considering that the derivative of power with respect to current $\frac{dP}{dI}$ vanishes at the MPP, is positive on the left hand side of the

MPP, and negative on the right hand side of the MPP. The derivative is

$$\frac{dP}{dI} = \frac{d(V_{TEG}I)}{dI} = V_{TEG} + I\frac{dV_{TEG}}{dI} \approx V_{TEG} + I\frac{\Delta V_{TEG}}{\Delta I}, \tag{5.2}$$

where the last approximation corresponds to a discretization with sampling time T_s with $\Delta V_{TEG} = V_{TEG} - V_{TEG}^{-}$ and $\Delta I = I - I^{-}$. Hence, the following qualifiers are obtained

$$\frac{dP}{dI} > 0 \;\Rightarrow\; \frac{\Delta V_{TEG}}{\Delta I} > -\frac{I}{V_{TEG}}, \tag{5.3a}$$

$$\frac{dP}{dI} = 0 \;\Rightarrow\; \frac{\Delta V_{TEG}}{\Delta I} = -\frac{I}{V_{TEG}}, \tag{5.3b}$$

$$\frac{dP}{dI} < 0 \;\Rightarrow\; \frac{\Delta V_{TEG}}{\Delta I} < -\frac{I}{V_{TEG}}. \tag{5.3c}$$

where (5.3a), (5.3b), (5.3c) corresponds to an operation point on the left hand side of the MPP, at the MPP, and on the right hand side of the MPP, respectively. Consequently, the current operation point I^{+} is moved accordingly. In comparison to P&O, IncCond offers a more robust quantifier on the location of the operation point. Similarly to P&O, IncCond requires a sufficiently large step and keeps moving around the MPP.

Other schemes which have been presented in the literature entail electro-thermal characterization of the TEG module to implement look-up tables for the MPP. The location and mounting of the thermocouples in the MPPT method proposed by [137] adds complexity to the TEG harvesting system and introduce possible errors when finding the accurate MPP of a larger TEG system (more than one TEG module), since it depends on accurate measurements of the temperature differences. Although, [138] proposed a simpler method to find the MPP of a TEG, a setback is that the

TEG system needs to be characterized prior to implementation since a pre-programed setpoint of MPPs is used by the algorithm. As the operating conditions change rapidly in waste heat recovery application such as those in the exhaust system of a vehicle [139], calibrating the system for every possible setpoint would be cumbersome. It should also be noted that the majority of the MPPT algorithms' performance is evaluated at steady-state which is not indicative of what occurs during the operation of TEGs in waste heat recovery applications.

5.3 Maximum Power Point Tracking

This section presents a new MPPT scheme called High Frequency Injection (HFI) for thermoelectric generators. The first subsection introduces the theory of the proposed scheme, HFI and the second presents the most commonly-used TEG MPPT scheme, P&O to evaluate and compare the performance of the proposed scheme.

The TEG module can be electrically modeled as shown in Figure 3.3 (b). Considering the electrical circuit, the power produced from the TEG may also be described as

$$P = I^2 R_l, \tag{5.4}$$

where R_l is the electrical load resistance connected to the TEG terminals. The TEG current, I, is therefore equal to

$$I = \frac{V_{oc}}{R_E + R_l}, \tag{5.5}$$

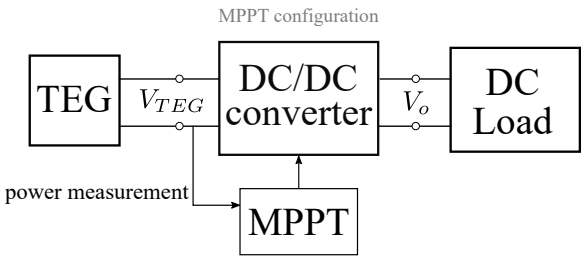

Figure 5.1: TEG MPPT configuration.

and (5.4) can be rewritten as

$$P = \frac{V_{oc}^2}{(R_E + R_l)^2} R_l. \tag{5.6}$$

The maximum power may now be found by taking the derivative with respect to R_l

$$\frac{dP}{dR_l} = \frac{V_{oc}^2 (R_E - R_l)}{(R_E + R_l)^3} = 0. \tag{5.7}$$

Thus, $R_l = R_E$ when the TEG power is maximized and results in

$$V_{TEG} = \frac{1}{2} V_{oc}. \tag{5.8}$$

The power output is maximized when the load resistance is equal to the TEG internal resistance as shown by (5.4)-(5.8). The MPPT configuration is presented in Figure 5.1, where a DC/DC converter is programmed to be interfaced between the TEG module and DC load, to control the TEG power output. At maximum power, the load resistance will equal the internal resistance of the TEG, thus (5.6) becomes

$$P_{max} = \frac{V_{oc}^2}{(R_E + R_E)^2} R_E = \frac{V_{oc}^2}{4R_E} = \frac{\alpha^2 \Delta T^2}{4R_E}. \tag{5.9}$$

5.3.1 Proposed MPPT

Simulations for the proposed MPPT scheme were presented in IECON'15 [140]. The following paragraphs describe the mathematical formulation behind the method. The High Frequency Injection (HFI) MPPT method adds a high frequency sinusoidal signal to the operating condition of the TEG which results in a perturbation that can be controlled directly, thus choosing the operation point of the TEG. A schematic of the operation for the HFI scheme is shown in Figure 5.2.

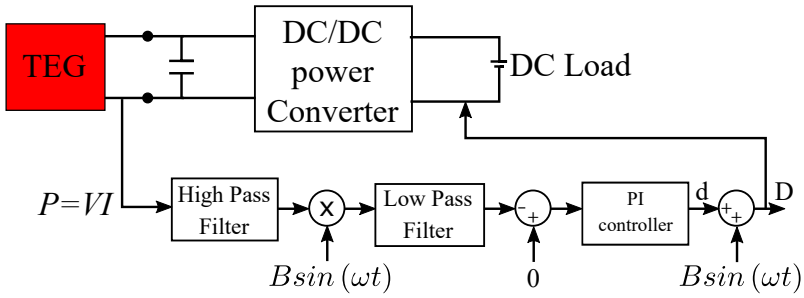

Figure 5.2: High Frequency Injection MPPT scheme.

Consider, a boost converter used in the MPPT configuration of Figure 5.1. The TEG output voltage, V_{TEG}, can be described as function of the DC load voltage, V_o, as

$$V_{TEG} = V_o(1 - D) \tag{5.10}$$

where D is the duty cycle of the switch in the power converter [141]. The output power of the TEG is then

$$P = IV_{TEG} \tag{5.11}$$

and I can be written as

$$I = \frac{V_{oc} - V_{TEG}}{R_E}. \tag{5.12}$$

Substituting (5.10) and (5.12) into (5.11) and simplifying with only known values (D, V_{oc}, V_o)

$$P = IV_o(1-D) \tag{5.13a}$$

$$= \frac{V_{oc}V_o - V_{oc}V_oD - V_o^2 + 2V_o^2D - V_o^2D^2}{R_E}. \tag{5.13b}$$

Assume a sine signal with angular frequency ω and amplitude B is injected into the duty cycle such that $d = D + Bsin(\omega t)$. Substitute d into (5.13a), the power output of the TEG, and the derivation is the same as (5.13b) except d is the new duty cycle. The power output, p, due to the duty cycle, d is now

$$\begin{aligned} p =& IV_o(1-d) \\ =& \frac{V_{oc}V_o - V_{oc}V_oD - V_o^2 + 2V_o^2D - V_o^2D^2}{R_E} \\ &+ \frac{Bsin(\omega t)\left(2V_o^2 - 2DV_o^2 - V_{oc}V_o\right)}{R_E} \\ &- \frac{B^2sin^2(\omega t)V_o^2}{R_E}. \end{aligned} \tag{5.14}$$

Rearranging (5.14), results in

$$p = P + \frac{Bsin(\omega t)[V_o(2V_{TEG} - V_{oc})]}{R_E} - \frac{B^2sin^2(\omega t)V_o^2}{R_E}, \tag{5.15}$$

by identifying that the first term is the power, P, from (5.13b), and the second term is a function of $(2V_{TEG} - V_{oc})$. It is interesting to note that this term has popped up, since the maximum power of a TEG occurs when the load voltage is equal to the internal voltage, i.e. $V_{TEG} = \frac{1}{2}V_{oc}$, as stated in (5.8).

Now consider only observing the high frequency terms, which are the second and third term of (5.15). A high-pass filter is used on p so that only the last two terms of (5.15) are left, since P is a low frequency term (does not have a sine term). However, since the last term is a sin^2 function, the high-pass filter will extract an offset since this function has an average value. Refer to this offset, or average value as C, which is defined as

$$C = \frac{1}{\omega t}\int_0^{\omega t} \frac{B^2 sin^2(\omega t)V_o^2}{R_E} d(\omega t) = \frac{B^2 V_o^2}{2R_E}. \tag{5.16}$$

Now (5.15) is rewritten after a high-pass filter has been applied to p as p_{hp} described by

$$\begin{aligned} p_{hp} &= p_1 + p_2 + C \\ p_1 &= \frac{Bsin(\omega t)V_o(2V_{TEG} - V_{oc})}{R_E} \\ p_2 &= -\frac{B^2 sin^2(\omega t)V_o^2}{R_E}. \end{aligned} \tag{5.17}$$

Multiply p_{hp} by $Bsin(\omega t)$ to get p_{sin} to determine whether the term $(2V_{TEG} - V_{oc})$ can be isolated

$$p_{sin} = Bsin(\omega t)p_1 + Bsin(\omega t)p_2 + Bsin(\omega t)C, \tag{5.18}$$

and apply a low pass filter to p_{sin}, which will again result in an offset, P_{lp} described as

$$P_{lp} = \frac{1}{\omega t}\int_0^{\omega t} p_{sin} d(\omega t). \tag{5.19}$$

By evaluating the average value, (5.19), P_{lp} is reduced to

$$P_{lp} = \frac{1}{\omega t}\int_0^{\omega t} Bsin(\omega t)p_1 d(\omega t) = \frac{B^2 V_o(2V_{TEG} - V_{oc})}{2R_E} \tag{5.20}$$

since the average value of sin^3 and sin is always zero over an entire number of periods. The offset, (5.20), can be negative or zero depending only on the sign of $(2V_{TEG} - V_{oc})$ since the constants $\frac{B^2 V_o}{R_E}$ are always positive.

By observing the offset from the power after the low pass filter, P_{lp} (5.20), three different cases arise. *Case 1*: $V_{TEG} = V_{oc}/2$, which makes P_{lp} zero and indicates that the MPP is reached. *Case 2*: $V_{TEG} > V_{oc}/2$ which signifies that the load voltage is higher than $V_{oc}/2$ and results in a positive offset. *Case 3*: $V_{TEG} < V_{oc}/2$ due to the load voltage being lower than $V_{oc}/2$ and equates to a negative offset. The offset, can now be controlled to zero using a PI controller and hence P_{lp} is used as feedback for a proportional integral controller to correct the duty cycle D of the power converter.

The injection frequency is chosen such that it can be resolved well in presence of the power electronic sampling times, e.g. one order of magnitude slower. The high and low pass filter are designed to operate on signals at injection frequency. Hence their bandwidth is chosen at least one order of magnitude lower than the injection frequency. When the HFI scheme is implemented, the power electronic sampling frequency is chosen as f_{sw}=200kHz, the injection frequency is 1kHz, the bandwidth of the high pass filter is 100Hz, and the bandwidth of the low pass filter is 10Hz. The injection amplitude, B, is .05V which is 1.25% of the operating TEG voltage. The losses in the converter are estimated to be negligible due to the low magnitude and frequency of the injection signal.

5.3.2 Perturb & Observe

The Perturb & Observe (P&O) scheme works by observing how the power output of the TEG shifts once a perturbation or setpoint change is made to the operating conditions. The sampling period, T_s, must be much larger than the electro-thermal time constants to ensure electro-thermal dynamics do not distort the power measurement. A flowchart explaining how the algorithm works is in Figure 5.3.

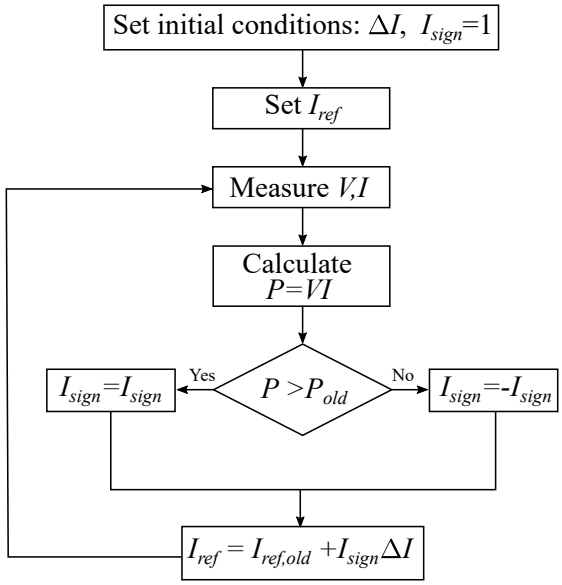

Figure 5.3: Perturb & Observe MPPT algorithm.

Initially, the current reference for the converter is set to some initial value, I_{ref}, then every T_s the power is measured (the TEG power as shown in Figure 5.1) and the current reference is either increased or decreased by ΔI according to either an increase or decrease in power. For the experimental validation, ΔI was chosen as 0.08A and T_s was 10ms. Although there exists adaptive P&O schemes such that ΔI varies as the MPP is approached [142], in this work a constant ΔI was chosen for simplicity and to have a baseline reference scheme for comparison.

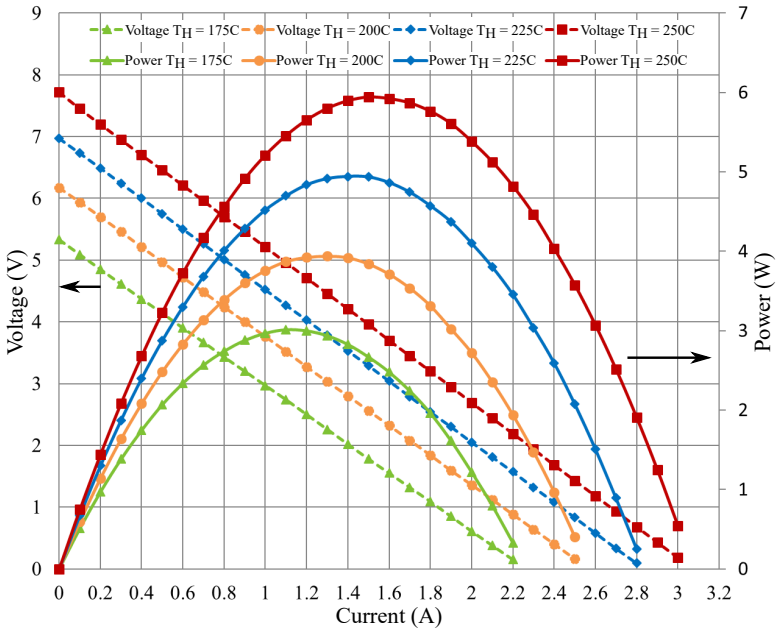

Figure 5.4: Experimental electrical characterization of commercial TEG module for T_C=35°C.

5.4 Experimental Validation

5.4.1 Electro-Thermal Characterization

To test the proposed HFI MPPT method as well as compare the performance to the mostly commonly used TEG MPPT scheme, P&O- the schemes need to be implemented on a TEG system. A TEG module from TECTEG MFR was experimentally characterized for various T_H, while maintaining T_C at 35°C in the TEM tester presented in Section 4.2.1. The characterization results are shown in Figure 5.4. As can be observed from the graph, there exists one maximum power point (MPP) per curve and it occurs at $V_{oc}/2$. The parameters, V_{oc}, R_E and α are tabulated in Table 5.1.

Taking the parameters from Table 5.1, (2.15b) was used to generate the power

Table 5.1: TEG module parameters

ΔT	$V_{oc}[V]$	R_E [Ohm]	α [V/K]
140	5.33	2.35	0.0381
165	6.17	2.40	0.0374
190	6.97	2.46	0.0367
215	7.72	2.51	0.0359

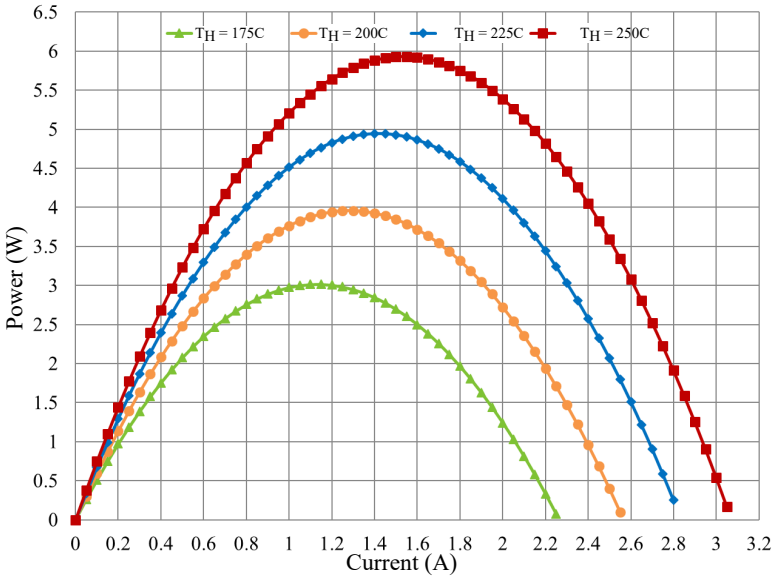

Figure 5.5: TEG power output model results for various T_H with T_C=35°C.

profiles in Figure 5.5. The maximum error between the experimental data in Figure 5.4 and the model in Figure 5.5 is 1.7%, but the maximum error only considering the MPP is 0.2%. Hence the parameters from Table 5.1 can be used to predict the maximum power as a function of temperature difference.

5.4.2 MPPT Experimental Setup

The converter utilized for the experiments was an off-the-shelf evaluation kit from Texas Instruments and the microcontroller is the C2000 TMS320F28377S. The experimental setup for the MPPT experiments is shown in Figure 5.6, which has the

same electrical configuration as shown in Figure 5.1. The TEG module is in the vacuum testing chamber described in Section 4.2.1 during the MPPT tests performed. For the Perturb & Observe scheme, the closed loop parameters for the current control were $k_p = 0.02$ and $k_i = 7.3 \times 10^{-5}$. For the HFI scheme, the parameters to control the offset, P_{lp} from the low pass filter, to zero were $k_p = 0.05$ and $k_i = 0.01$.

The converter efficiency was also evaluated for various input current and voltages, with the results shown in Table 5.2.

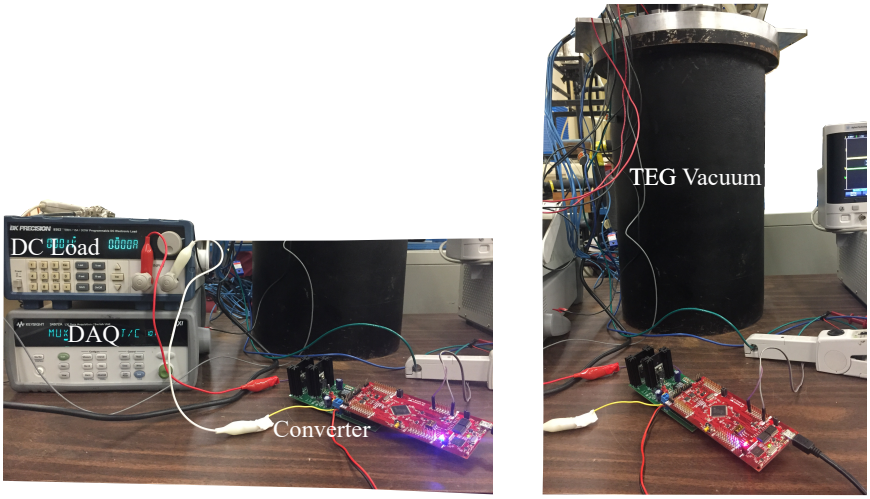

Figure 5.6: MPPT experimental setup.

Table 5.2: Converter efficiency.

$I_{in}\,(A)$	$V_{in}\,(V)$	$P_{in}\,(W)$	$P_{out}\,(W)$	$\eta\,(\%)$
0.50	9.01	4.51	3.70	82.2
1.10	9.01	9.91	8.29	83.7
1.90	9.01	17.12	14.92	87.2
0.50	12.0	6.0	4.86	80.9
0.95	12.0	11.4	10.15	89.0
1.35	12.0	16.2	14.87	91.7

5.5 Experimental Results

The following sections present the results from the experiments which were completed to evaluate the performance of the proposed HFI MPPT scheme as well as the most-commonly used P&O MPPT scheme. The MPPT experiments were performed with the TEG module that was characterized in Section 5.4. The experimental setup was previously discussed and is shown in Figure 5.6.

The experiments were performed to not only compare the HFI scheme to the P&O scheme, but also to compare the HFI results to other experimental work found in the literature. The three experiments conducted were similar to those found in [143], which include thermal transients. The first experiment is a steady-state test which is commonly used to evaluate how well the MPPT scheme finds the MPP. The second experiment is designed to test the response time of the algorithm. The TEG module is at open-circuit and has a fixed temperature difference and suddenly, the tracking scheme is turned-on. This is done to observe how fast the MPPT scheme can find the MPP or half the open circuit voltage. The third experiment is to evaluate how the MPPT scheme performs when the TEG experiences temperature changes (ΔT is not constant). This is a more realistic test, as the TEG will experience temperature fluctuations when implemented in any waste heat recovery applications as previously discussed in Section 5.1.

5.5.1 Steady-State Performance

The purpose of this steady-state test is to evaluate whether the proposed MPPT scheme- HFI, can accurately track the MPP of the TEG at fixed temperature differences. The MPPs of the TEG module were previously characterized in Section 5.4 for

various temperature differences. The P&O scheme was also implemented and tested to have a performance comparison. The steady-state tests were performed as follows: 1) Use the TEG testing facility to reach the desired temperature difference across the TEG, 2) Turn-on the desired tracking scheme (HFI or P&O) and wait for the MPP to be reached while maintaining a fixed temperature difference across the TEG, 3) Wait to reach electro-thermal steady-state and measure the voltage across the TEG module as well as the current flowing through the TEG.

The results of the steady-state tracking performance for both HFI and P&O are shown in Table 5.3. The first column tabulates the characterization results. The second column presents the operating TEG voltage and power produced by the TEG module for both schemes. Since the P&O scheme oscillates around the MPP, the operating range is presented. The final column shows the error compared to the expected operating TEG voltage and TEG power output (from characterization). The MPPT scheme errors from Table 5.3 are also presented in graphical form in Figure 5.7.

At steady-state the HFI scheme has a tracking efficiency, defined as operating

Table 5.3: Steady-state results: (1) Characterization results for various temperature differences, (2) Experimental MPPT Results for both schemes: V_{MP}, Voltage at max power (MP), P_{MP} power output at MP (3) MPPT performance error compared to characterization.

	Charact. Results		MPPT Results				MPPT Performance			
			HFI		P&O		HFI		P&O	
ΔT [C]	V_{MP} [V]	P_{MP} [W]	V_{MP} [V]	P_{MP} [W]	V_{MP} [V]	P_{MP} [W]	V_{MP} [%]	P_{MP} [%]	V_{MP} error [%]	P_{MP} error [%]
140	2.67	3.02	2.57	3.01	2.92 - 3.24	2.68 - 2.74	3.56	0.27	9.57 - 21.58	9.12 - 11.11
165	3.09	3.95	2.97	3.94	3.35 - 3.68	3.49 - 3.54	3.73	0.26	8.59 - 19.29	10.38 - 11.65
190	3.49	4.94	3.38	4.93	3.89 - 4.19	4.43 - 4.48	3.01	0.17	11.62 - 20.23	9.37 - 10.38
215	3.86	5.93	3.76	5.92	4.14 - 4.86	5.33 - 5.38	2.59	0.15	7.25 - 25.91	9.24 - 10.09

point of the MPPT scheme (P_{op}) divided by the available max power (MP)

$$\eta_{tracking} = \frac{P_{op}}{MP} \tag{5.21}$$

of 99.73%. However, the tracking efficiency of the P&O scheme is approximately 90% which has previously been found by other researchers [144]. Although more adaptive P&O schemes can be implemented to achieve higher tracking efficiencies such as variable step sizes when approaching the MPP, the purpose of these experiments was to validate the hypothesis that the proposed HFI scheme can accurately track the MPP. The HFI tracking efficiency for various temperature differences is compared to the P&O tracking efficiency in Figure 5.7 (c). Further work could be done in designing the DC/DC converter to further reduce losses, however this is out of the scope of this paper.

5.5.2 Fast Transient Performance

A fast transient test was performed by maintaining the TEG module at a fixed temperature difference and observing the response when the MPPT scheme was turned on. When the HFI scheme is turned on, as seen in the oscilloscope capture of Figure5.8, the TEG voltage changes from 5.68V and reaches half the open circuit voltage (MPP) of 2.8V in 2.4ms. Compared to similar performance evaluations, [143] completed a similar experiment and their MPPT response time was 8ms, while the researchers [127] had a response of 300ms. To the best of the authors' knowledge, 2.4ms is the fastest settling time that has been reported in the literature. The P&O scheme results are not shown since the sampling time of the scheme is 10ms, as previously mentioned. The electro-dynamics need to reach steady-state before the power

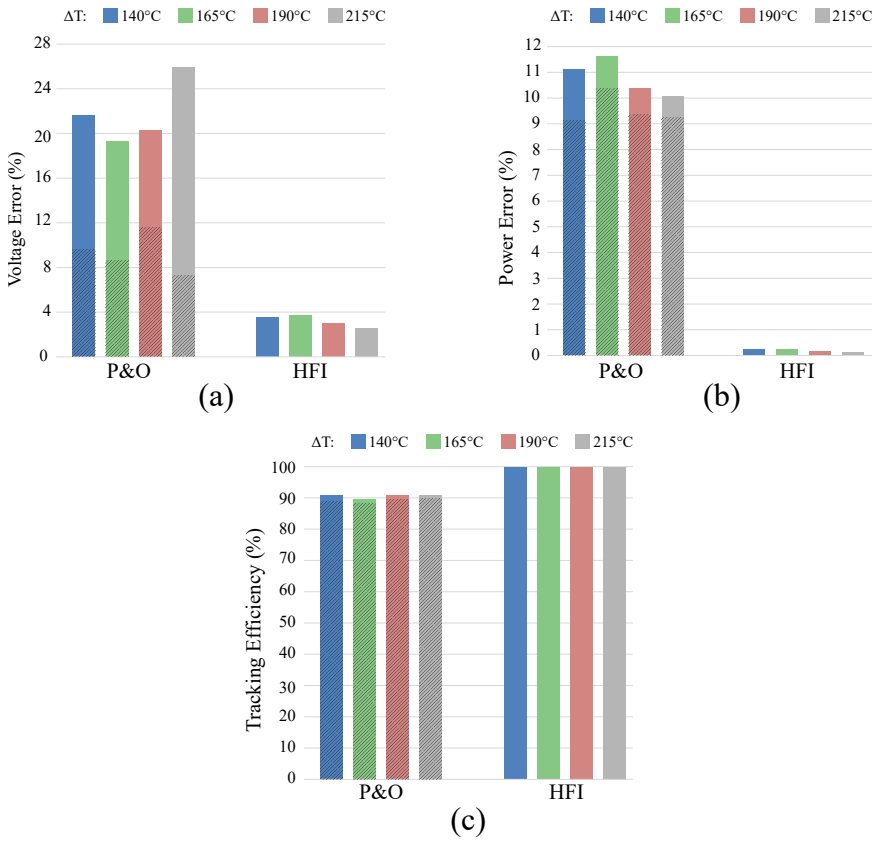

Figure 5.7: Steady-State performance from Table 5.3 represented in graphical form. (a) Voltage error (%) (b) Power error (%) for various temperature differences (ΔT) (c) Comparison of tracking efficiency for the P&O scheme and HFI scheme.

is measured for the P&O scheme, hence the settling time would be much higher than the HFI scheme.

5.5.3 Thermal Transient Performance

The final test to evaluate the performance of the HFI scheme was observing the MPP tracking while the TEG operated under thermal transients. When TEGs harvest energy from waste heat sources such as the exhaust system of a vehicle, they experience

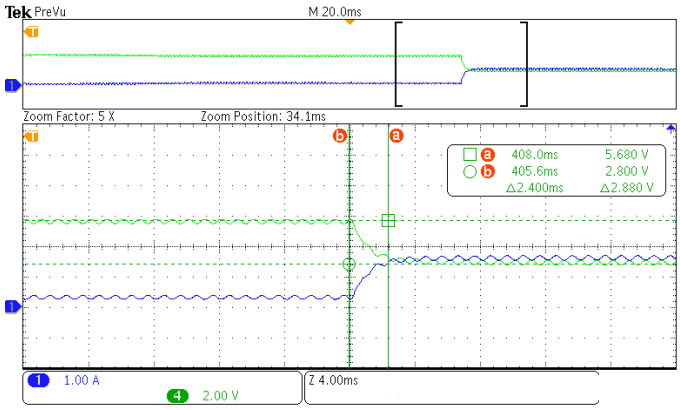

Figure 5.8: Transient Evaluation: TEG output voltage changes from V_{oc} to $V_{oc}/2$ when HFI MPPT scheme is turned on. Response time is 2.4ms.

variable temperature differences, therefore the MPPT scheme was tested in a transient setting. The test was performed as follows: 1) the TEG module is initially at one temperature difference, 2) the heater power is increased, simultaneously turning on the MPPT scheme, 3) the temperature difference across the TEG is recorded as a function of time, 4) the test is stopped once the temperature stops varying. The temperature difference across the TEG is plotted in green in Figure 5.9 (b) as a function of time during the tracking of the HFI scheme. The power produced by the HFI scheme is plotted in blue in Figure 5.9 (b), as well as the theoretical maximum power of the TEG module (red). The theoretical maximum power output of the TEG is calculated from (5.9) with the parameters from Table 5.1, since the temperature difference is known every second. The voltage, current, and power generated by the HFI scheme are also shown in the oscilloscope screenshot in Figure 5.9 (a).

As observed in Figure 5.9, the HFI scheme performs well at tracking the MPP over time. The maximum error over the entire time length is 1.3% which makes the tracking efficiency during transient operation 98.7%. The authors in [143] reported the same tracking efficiency during their thermal transient test. Although [145] completed

a transient test, their tracking efficiency was not reported and a 0.05W power output difference was presented over 60 mins of tracking.

The P&O scheme was also evaluated during a thermal transient and the results are shown in Figure 5.10. As previously discussed, the P&O scheme does not find an exact operating point but instead oscillates around the MPP. Hence, oscillations in the power are observed in Figure 5.10 (b). The maximum error between the power produced by the P&O MPPT scheme and the expected maximum power is 10%.

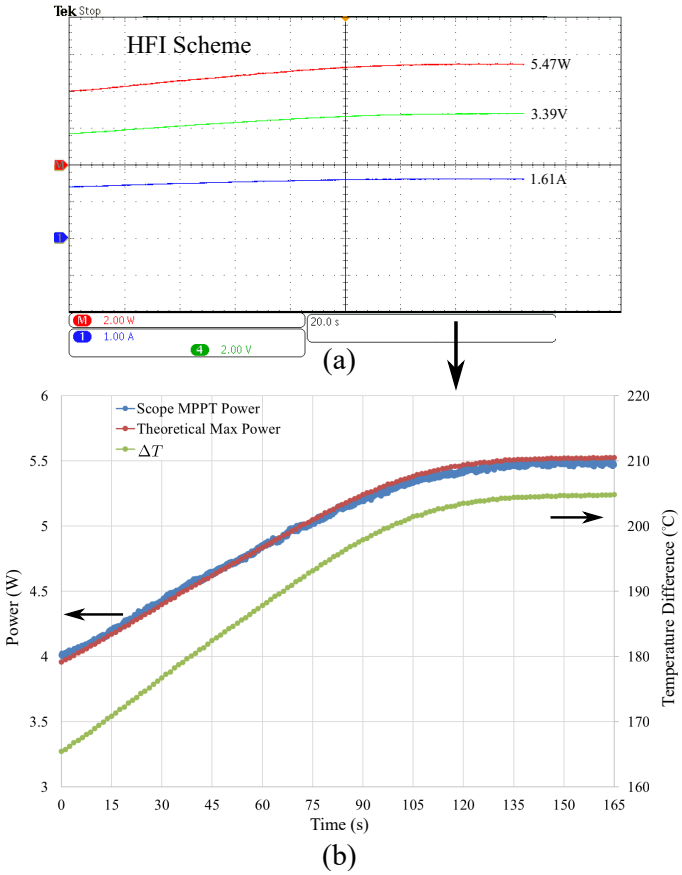

Figure 5.9: Thermal transient: (a) Scope screenshot of TEG voltage and current measurement during HFI tracking (b) Comparison of expected power output as a function of temperature difference (ΔT) of the TEG module versus HFI MPPT power.

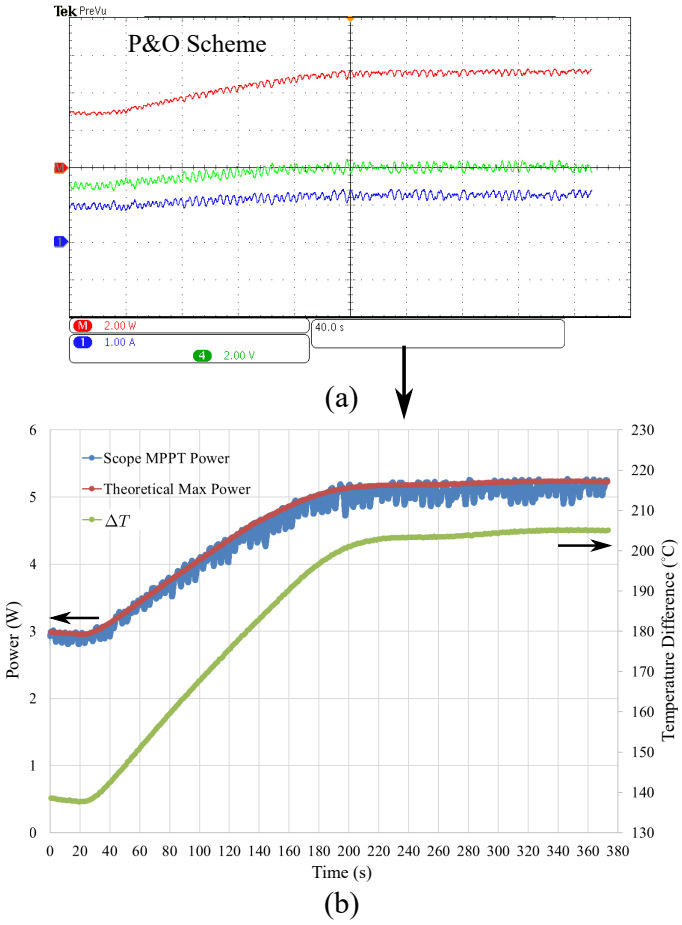

Figure 5.10: Thermal transient: (a) Scope screenshot of TEG voltage and current measurement during P&O tracking (b) Comparison of expected power output as a function of temperature difference (ΔT) of the TEG module versus P&O MPPT power.

5.6 Summary

Although thermoelectric generators may be implemented for energy harvesting in waste heat recovery applications, the system efficiency is improved through power converters to ensure the maximum power is generated by the TEG. Since waste heat sources such as the exhaust system of a vehicle vary rapidly in their operating conditions, a maximum power point scheme must be employed to track the varying

power output by the TEG system.

In this chapter, a High Frequency Injection (HFI) maximum power point tracking scheme was proposed and experimentally validated through three different experiments, as well as compared to the most commonly used MPPT scheme in the literature, P&O. The High Frequency Injection scheme works by adding a high frequency signal to the operation of the TEG, which results in an offset that can be controlled to directly arrive at the TEG's MPP. The experimental results showed that the response time of the proposed MPPT scheme is 2.4ms which is 3 times faster than any scheme presented in the literature. An advantage of the proposed scheme is that the algorithm can be implemented into current MPPT hardware, i.e. no additional sensors. The HFI scheme was implemented with an off-the-shelf converter and achieved a tracking efficiency at steady state of 99.73%, comparable to the best steady-state tracking schemes while achieving the fastest recorded dynamics. During thermal transients the HFI MPPT exhibited an efficiency of 98.7%.

Chapter 6

Vehicle Exhaust Model

6.1 ADVISOR Vehicle Model

The operating condition of a TEG WHR system depends on the vehicle's exhaust system behavior since this is the waste heat source for energy harvesting. In particular, the mass flow rate and temperature of the exhaust gases are of particular interest since they define the boundary conditions of the hot side heat exchanger. During operation of an ICE vehicle, the mass flow rate of the exhaust gases varies rapidly and the expected temperature range varies depending on the location in the exhaust system as shown in Figure 6.1. Therefore, a model was developed that could predict these parameters for different driving cycles. The open source vehicle software, Advanced Vehicle Simulator (ADVISOR) which was developed by the US Department of Energy (DOE) was utilized [146]. The software is built in the MATLAB/Simulink environment and all the component models were developed empirically from test data.

The vehicle model was created for a 190kW SI engine car and the exhaust gas

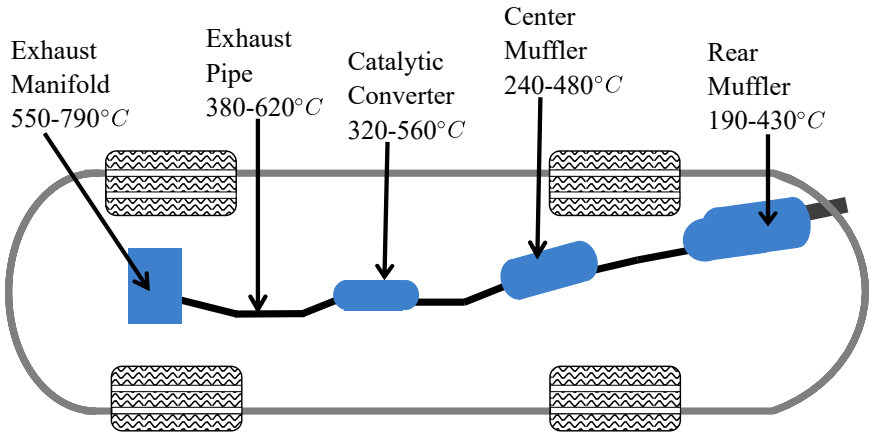

Figure 6.1: Exhaust temperature distribution for a 100kW SI engine [44].

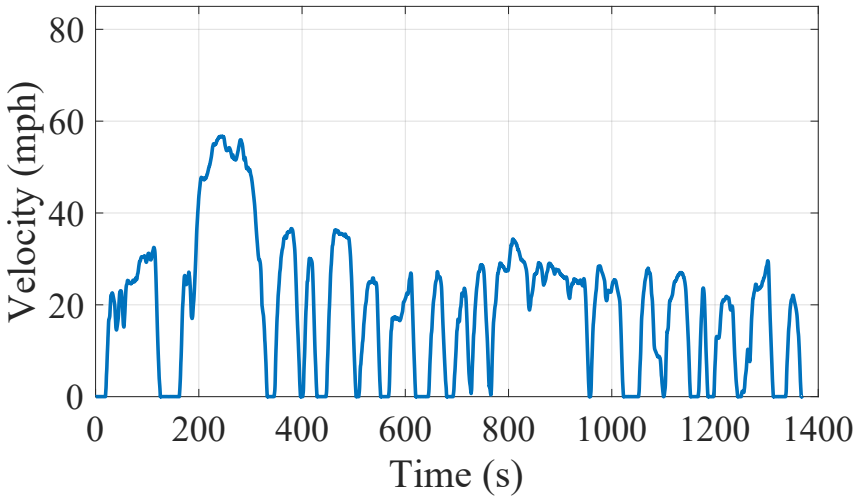

Figure 6.2: Vehicle speed over a UDDS drive cycle.

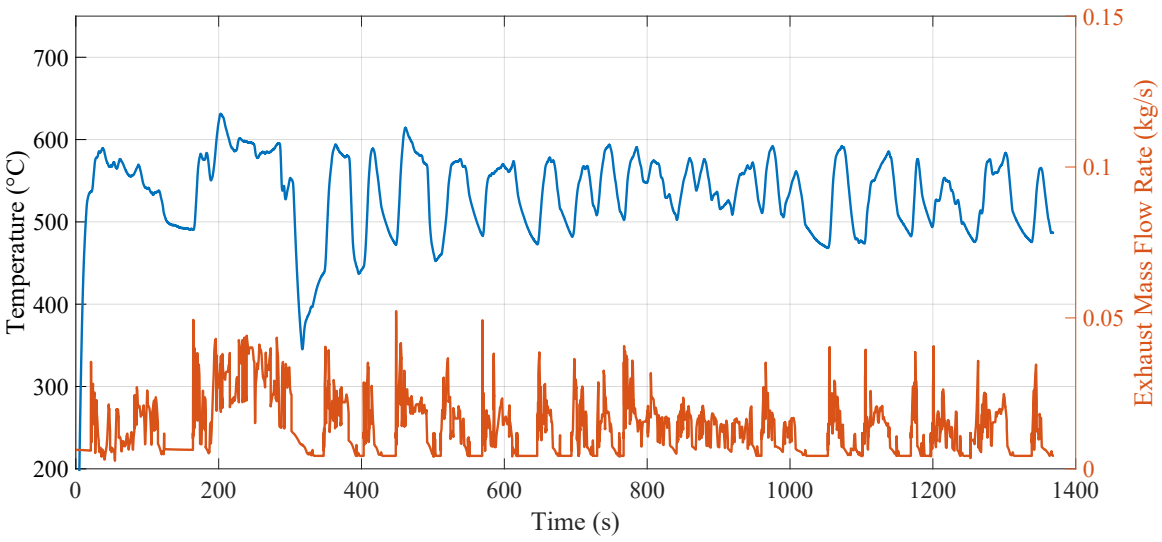

Figure 6.3: Exhaust gas temperature and mass flow rate over a UDDS drive cycle.

temperature and mass flow rate at the exit of the engine exhaust port was simulated for various drive cycles. An urban dynamometer drive schedule (UDDS) drive cycle is shown in Figure 6.2 and is simulated to obtain the engine exhaust behavior. The exhaust temperature is plotted on the left y-axis of Figure 6.3 and the mass flow rate is plotted on the right axis. As explained in Section 3.5, the DOE has conducted research for WHR in vehicles utilizing TEGs and the work from [44] reports the typical temperature distribution of the exhaust gases throughout the exhaust system which is shown pictorially in Figure 6.1. For a 100kW SI engine, the exhaust gases at the exhaust manifold are between 550-790°C depending on partial to full engine load and the temperature decreases as the exhaust gases move downstream to the rear muffler to 190-430°C.

The TEG WHR system will be investigated for installation after the CC, therefore the temperature predicted by the ADVISOR vehicle model at the exhaust port was reduced by 230°C to match the lower temperatures expected after the CC. Both city

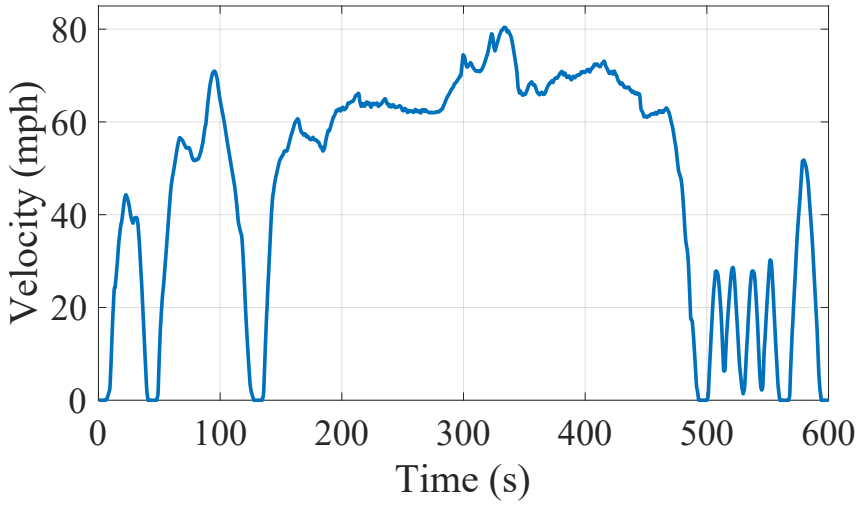

Figure 6.4: Vehicle speed over time for a US06 drive cycle.

drive cycles like the UDDS drive cycle and more aggressive vehicle drive cycles such as the US06 were simulated as depicted in Figure 6.4. The expected exhaust flow rates during a US06 drive cycle are shown in Figure 6.5 and the exhaust temperature plotted on the left y-axis was decreased by 230°C when used as an input to the transient TEG WHR system model.

6.1.1 Vehicle Exhaust Model Verification

The exhaust temperatures and mass flow rates predicted by the developed ADVISOR vehicle model were used to investigate the transient power output of the TEG WHR system for various drive cycles. However, the vehicle model needed to be verified to understand whether the predicted temperatures and mass flow rates are within range of the expected values under real driving conditions. Therefore, the ADVISOR model was modified to simulate the BMW 530i, 190kW gasoline engine and the results were compared to the experimental results published by BMW in [58].

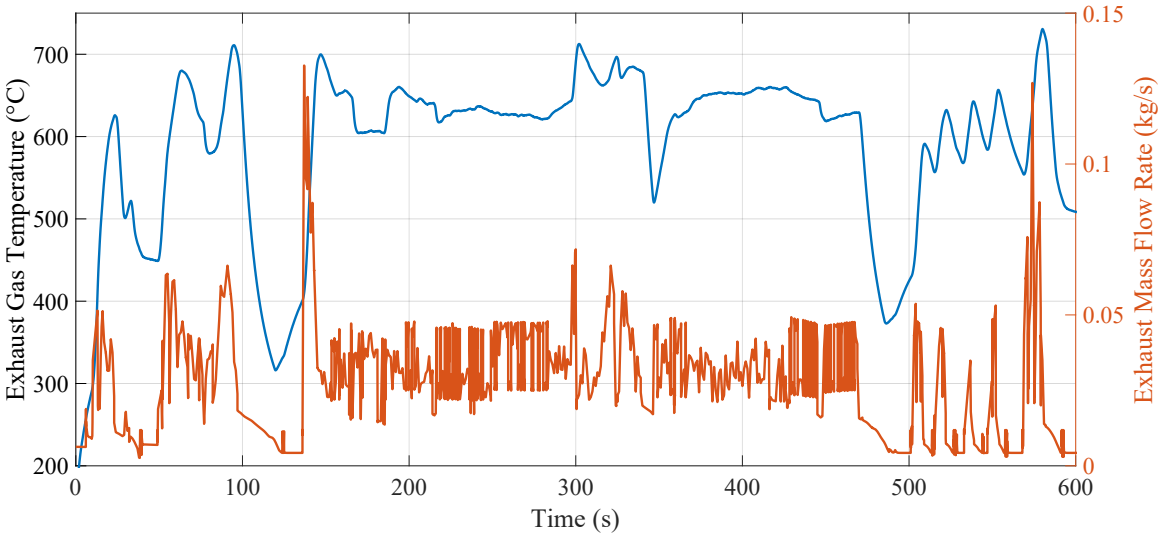

Figure 6.5: Exhaust gas temperature and mass flow rate over a US06 drive cycle.

The predicted exhaust temperature at the exit of the three-way catalytic converter (TCC) from the developed ADVISOR vehicle model is plotted in black ('Vehicle Model') in Figure 6.6. The authors in [58] measured the exhaust temperature over a New European Drive Cycle (NEDC) drive cycle and developed their own vehicle model to predict the operating exhaust conditions. The measured exhaust temperature ('Exp') is plotted in blue and their simulation results ('Sim') are shown in dashed blue. As can be observed, the vehicle model predicts the exhaust temperature within range of the measured experimental data and captures the overall transient behavior. The exhaust mass flow rate from the ADVISOR model is plotted in Figure 6.7 and compared to the experimentally measured data over an NEDC drive cycle. Once again, the predicted values from the model are within range of the real vehicle exhaust mass flow rate values and the overall transient behavior is captured.

The results shown are a verification of the developed vehicle model rather than a

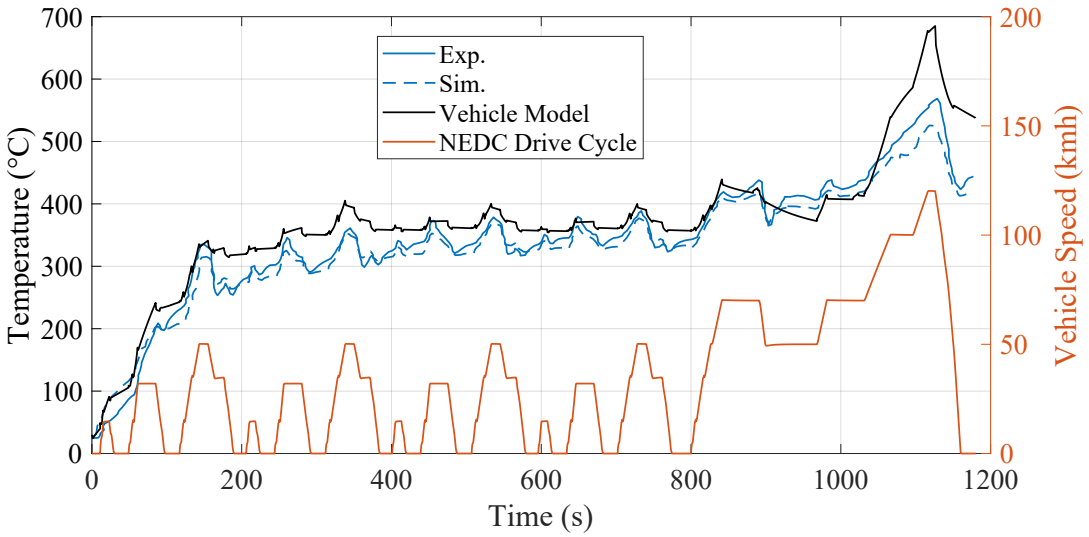

Figure 6.6: Comparison of exhaust temperature at exit of three-way catalytic converter predicted by vehicle model to experimental data from [58] over an NEDC drive cycle.

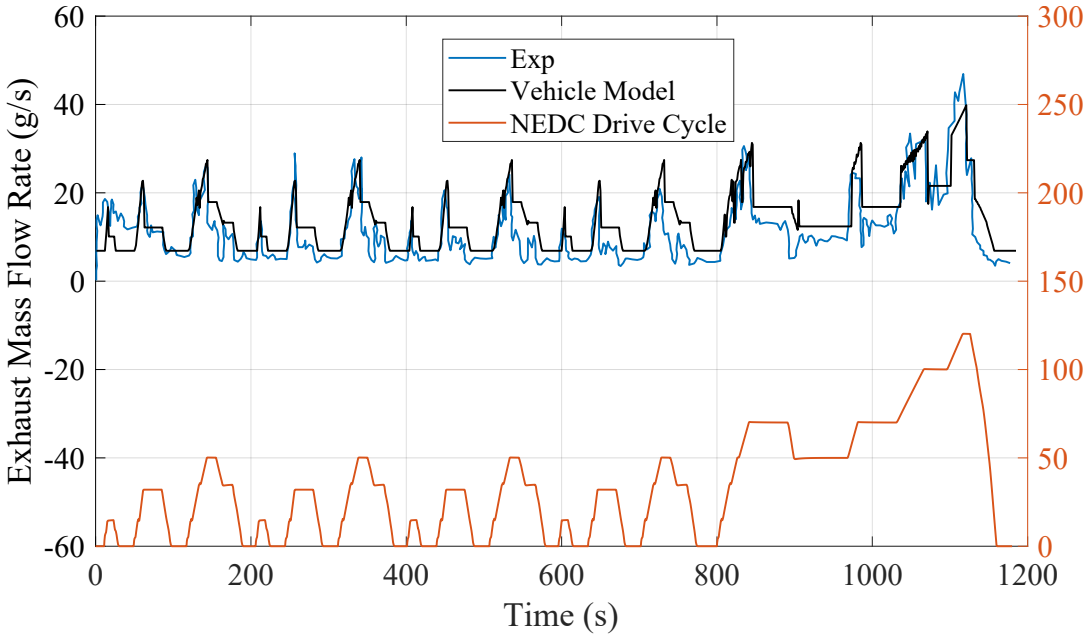

Figure 6.7: Comparison of exhaust mass flow rate predicted by vehicle model to experimental data from [58] over an NEDC drive cycle.

validation because the goal is not to model the engine investigated by BMW, specifically. The objective of the model is to simulate the exhaust temperatures and mass flow rates expected in a real vehicle to gain a deeper understanding of the effects that a transient environment would have on waste heat recovery and system design. Certain engineering assumptions were made to simulate the BMW engine and had more information been given regarding the vehicle, more accurate simulations would have been achieved. However, the model verification shows that reasonable exhaust temperature and mass flow rates are reproduced, therefore the developed vehicle model results can be used as an input to the transient TEG WHR system model to investigate which effects affect system performance in a transient thermal environment.

Chapter 7

Maximizing TEG Energy Recovery

7.1 Literature Review

The vast majority of research around thermoelectric generators used in the recovery of waste heat in automotive applications has focused on maximizing the power produced by a system and optimizing the TEG module design at a single operating point. As reviewed in Section 3.5, TEG WHR systems are tested and built for maximum engine load conditions where the exhaust temperature and mass flow rate is the highest during operation, hence the design point is where the thermal losses are greatest. However, as was observed in Figure 6.3, there are only instantaneous times during the drive cycle where a larger amount is available for recovery (i.e. higher mass flow rate), while at most other times during the drive cycle the exhaust temperatures and flow rates are lower than the peak.

To investigate energy recovery in a dynamic environment such as the exhaust system of a vehicle, a transient system model needed to be developed to observe the transient power output over a drive cycle. Further, investigation of the total

energy recovered versus instantaneous power generated was of interest. Although a few transient models have been presented in the literature as shown by the Table 7.1, the majority of them have focused on the predicting the power from a single TEG module without considering the thermal capacity of the heat exchangers. Although [39] did investigate how the power output changed under steady-state conditions versus transient conditions, the focus was on a single TEG WHR system design and the impact of system size was not considered. Their work showed that the wrong TEG module (TE properties) was selected since the design was based on the highest expected working temperatures (maximum engine load), while the drive cycle mostly operates at lower temperatures, and hence the module performance was degraded at lower temperatures. In this chapter, the validated TEG WHR system model is used to investigate power generation as well as total energy recovered (integral of power with time) to investigate the effect of different operating conditions on total energy recovery.

Table 7.1: Review of transient models found in the literature.

Model Type	Purpose	Reference
finite difference, TEG module	investigate improvement in HEX	[28]
3D FEA model, TEG module	transient power output f(ΔT)	[23]
TRNSYS TEG module	transient power output f(ΔT)	[147]
TEG module thermal network	investigate $P = f(v_{vehicle})$	[21]
ANSYS Fluent, system model	compare power output SS vs. transient	[39]
Lumped Capacitance System	HEX exit temperature control	[103]

7.2 Effect on Heat Transfer

The transient model was implemented to predict the power output using the time-varying boundary conditions of exhaust gas temperature and mass flow rates from the

vehicle model. A flow chart with an overview of the overall transient model and the submodels developed in the previous chapters is shown in Fig. 7.1. The power output from the TEG system is maximized at every time step and each row (ΔT=constant) of TEG modules is assumed to have it's own MPPT.

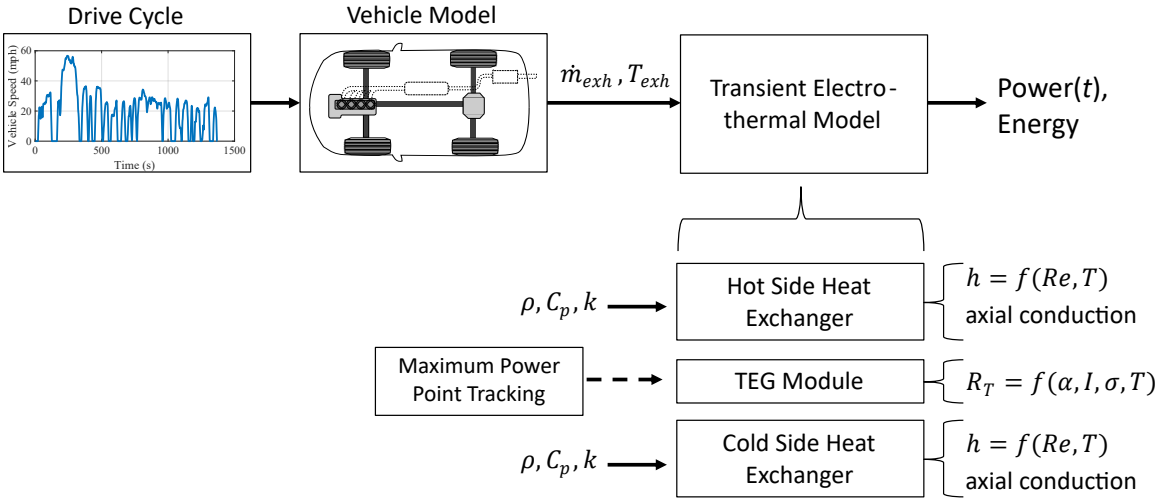

Figure 7.1: Overview of transient model to investigate power output over various drive cycles.

A case is first simulated of a TEG WHR system with 48 TEG modules installed downstream of the CC of a 190kW SI engine vehicle. The power output from the system over two UDDS drive cycles is plotted in Figure 7.2. The thermal capacity effects can be observed at the start of the drive cycle, as the power slowly ramps up and reaches its 'steady-state' after 2 drive cycles. The peak power output of the system over the drive cycle is about 375 W and occurs at one instantaneous time in the drive cycle where the exhaust mass flow rate is maximum. The high mass flow rate (compared to the rest of the drive cycle) at this point is 0.04 kg/s, while the majority of the time it is $\sim$ 0.01kg/s.

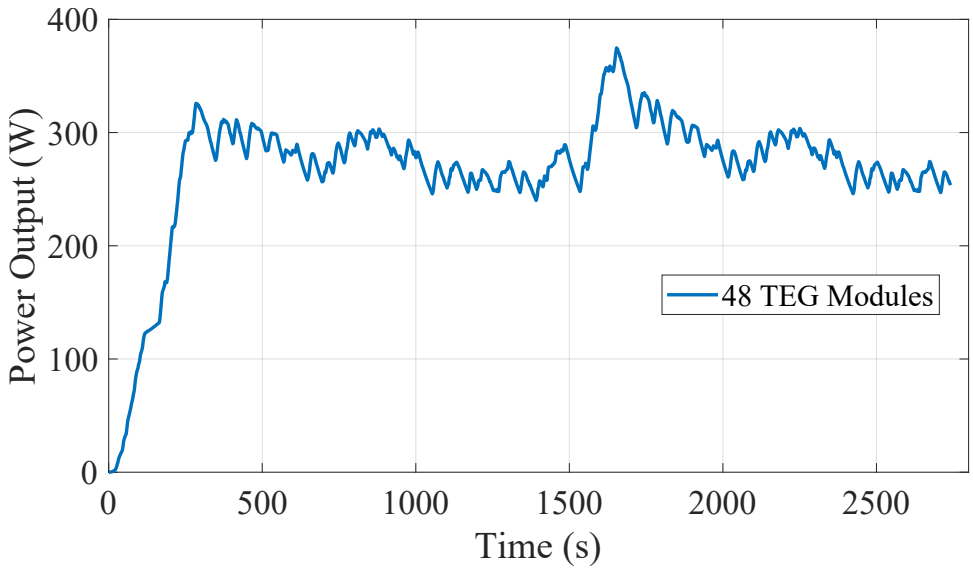

Figure 7.2: Power output of a TEG WHR system with 48 TEGs over a UDDS drive cycle.

Different TEG WHR system sizes are investigated to see the effect on the maximum power generated, as well as the total energy recovered over a vehicle drive cycle. As more TEG modules are added to the system, the hot side and cold side HEX surface areas need to increase to accommodate for these additional modules. The power output, assuming the system has operated over a couple of drive cycles is plotted for a UDDS drive cycle in Figure 7.3 for two systems sizes: one with 48 TEG modules and the other with 24 TEG modules. The 48 TEG module system is double the size of the system with 24 TEG modules. As expected from literature, the larger TEG WHR system (the 48 module system) generates the highest instantaneous power output which occurs around 250 seconds in the UDDS drive cycle. However, it is interesting to note that at other times in the drive cycle, the smaller system generates more power than the larger system. When the system was doubled from 24 TEGs to 48 TEGs, an extra row of TEGs in the direction of exhaust flow was added.

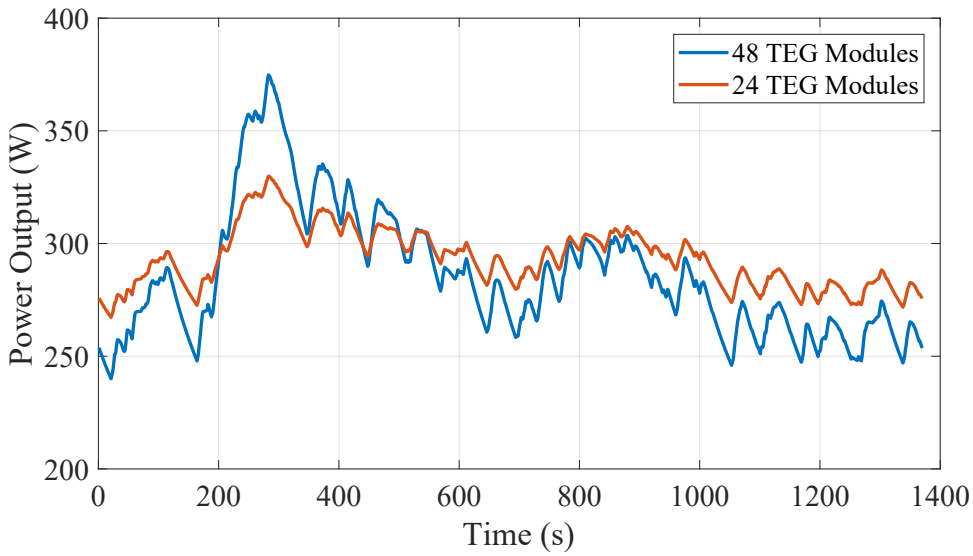

Figure 7.3: Power output comparison of a TEG WHR system of two sizes: 48 TEG modules and 24 TEG modules.

The temperature T_H, which determines the power output of the system, is plotted in Figure 7.4 for the first row of TEGs of both systems. The temperature of the first TEG row of the smaller system (24) is higher than the temperature of the larger system (48), hence the smaller system can generate a higher power output. To better understand the power degradation due to the addition of a second row, the axial temperature distribution of the hot side heat exchanger is plotted in Fig. 7.5 for an exhaust flow rate of 0.04kg/s and inlet temperature of 310°C. When the heat exchanger length is doubled, the hot side temperature of the TEG decreases due to heat being transferred axially through the HEX base in the direction of exhaust flow. It is also observed in Fig. 7.5, that the temperature difference between the exhaust gases and the hot side of the TEG decreases, therefore there is less energy to recover downstream. The temperature drop due to axial conduction is intensified at lower

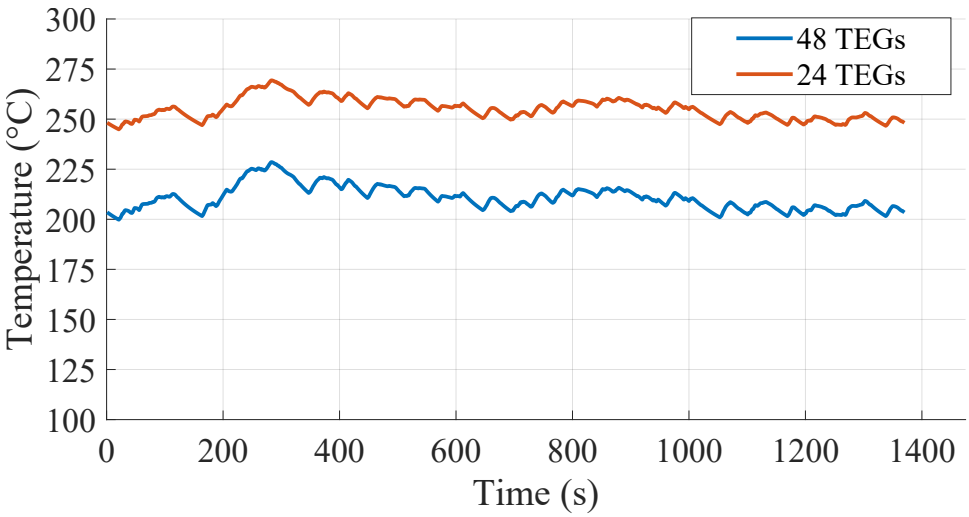

Figure 7.4: Comparison of the TEG hot side temperature of the first row of TEG modules in two systems.

flow rates and since the average flow rate of the vehicle is ∼0.015 kg/s, the power degradation effect is more prevalent. If the exhaust flow rate was higher (more energy available for recovery), the temperature change due to the addition of one more row would not be as great.

Using the developed model to study different TEG WHR system sizes, the power generated over a drive cycle for the 190kW SI engine can be integrated to calculate the total energy recovered during operation. The total electrical energy recovered for a UDDS drive cycle is seen in Figure 7.6 and as can be observed, an optimum system size exists. In this particular case, the energy recovered is maximized if a total of 24 TEG modules are installed in the system. Although the maximum instantaneous power of 380 W is generated with a 72 module system, the energy recovered is maximized with a smaller system. As more TEG modules are added to the system, the downstream TEGs negatively affect the temperature drop, ΔT, across the TEG module which directly affects the power produced.

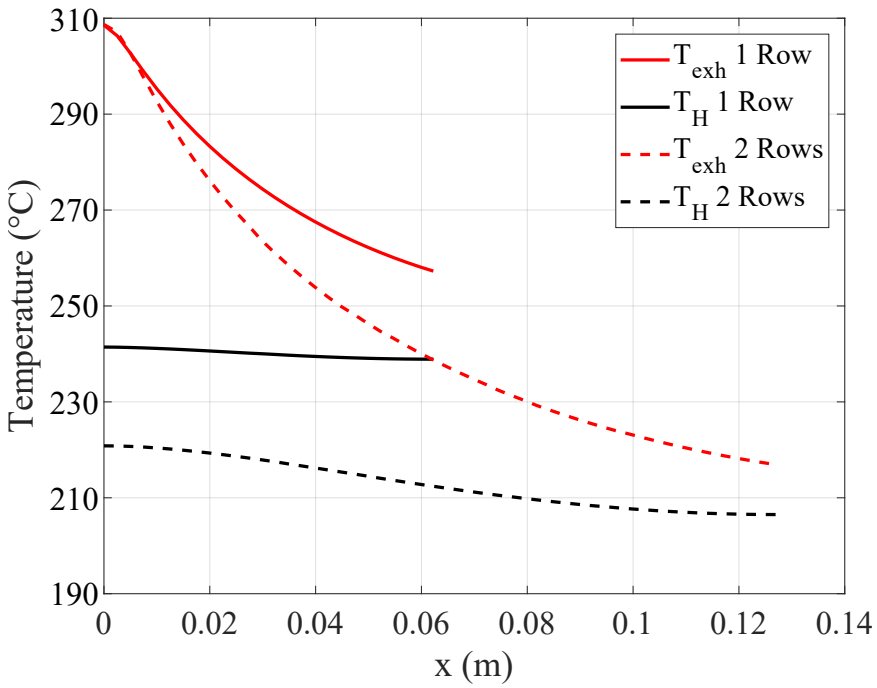

Figure 7.5: Temperature distribution of exhaust and TEG hot side for 1 and 2 Row system.

The analysis was repeated for the same vehicle but rather assuming a more aggressive, long-haul type of driving. Imposing a US06 drive cycle, the total energy recovered for different system sizes is calculated and plotted in Figure 7.7. Once again an optimum design point is found, which in this case is 72 TEG modules since the vehicle is operating at higher engine loads. Since the optimum point for the system changes based on the chosen vehicle drive cycle, a standard drive cycle should be used such as the the Worldwide Harmonised Light Vehicle Test Procedure (WLTP) drive cycle for light-duty passenger vehicles. Also, before designing a TEG WHR system for a vehicle, it should first be determined if the vehicle will be used for more city-type driving or for long-haul driving. The aim of the analysis was not to choose

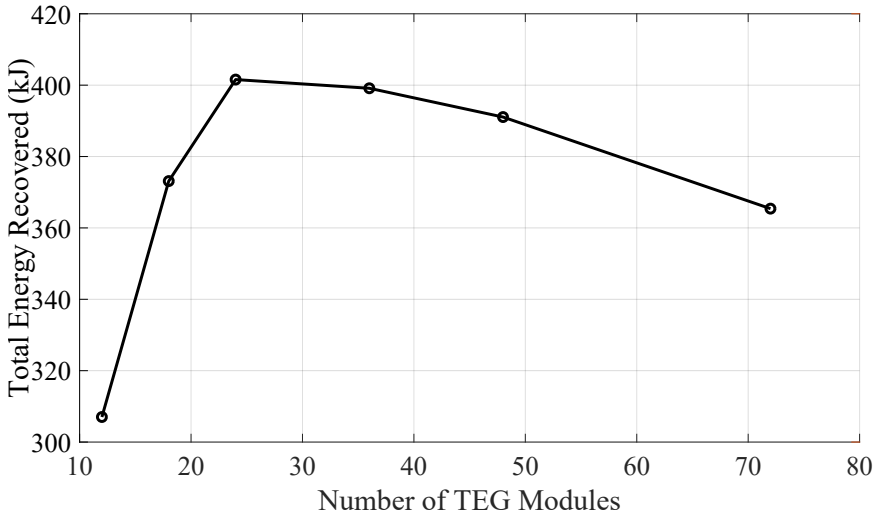

Figure 7.6: Total energy recovered over a UDDS drive cycle vs. the total number of TEG modules in a system.

a specific system size, as the optimum changes depending on the engine size and location of installation in the exhaust system. Rather, the goal is to demonstrate that a larger TEG WHR system is not the optimum design point and neither is peak power output, which has been used prevalently in the literature as the performance metric for TEG WHR systems.

Designing a TEG WHR system for peak power output results in an over-designed system that can potentially reduce the total energy recovered by the system. To further understand this phenomenon, a study was performed for the same 190kW SI vehicle with TEG WHR systems made up of a modular unit, shown in Fig. 7.8, investigated for city-type driving. The modular unit consists of 6 TEG modules, one hot side HEX and two cold side HEXs. As the system gets larger, the modular units can be added perpendicular to the exhaust flow (number of 'Columns' increases, Fig. 7.8(a)) or in the direction of exhaust flow (number of 'Rows' increases, Fig. 7.8(b)).

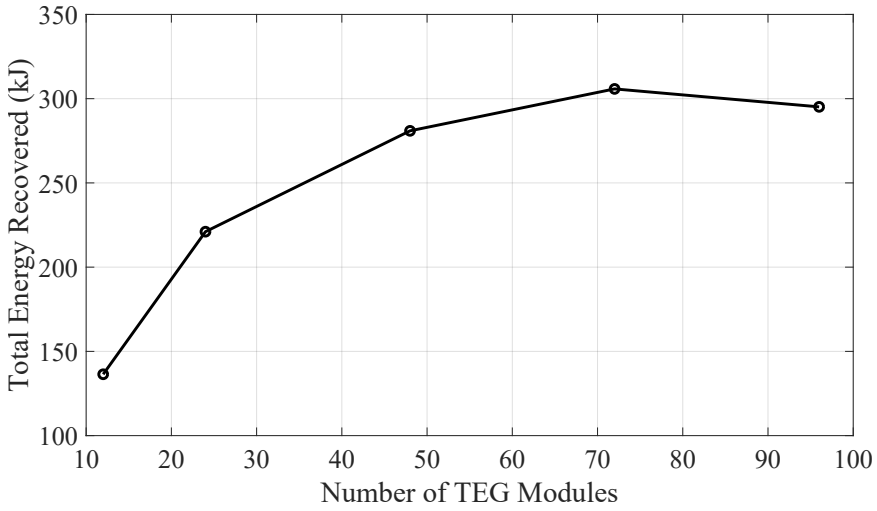

Figure 7.7: Total energy recovered over a US06 drive cycle vs. the total number of TEG modules in a system.

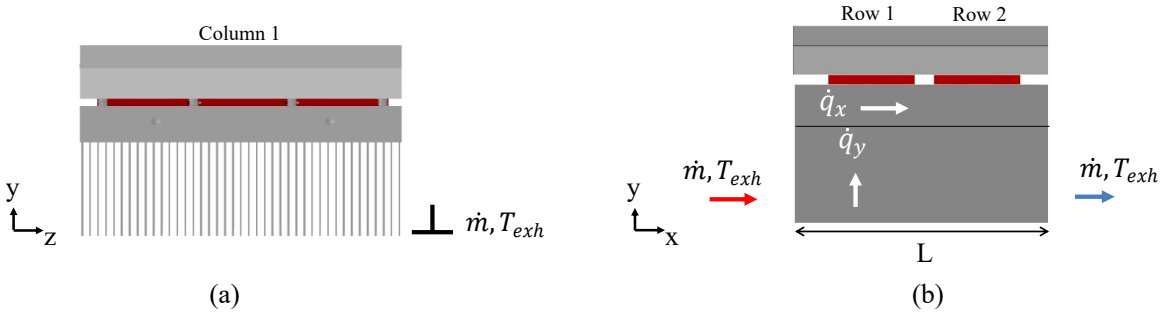

Figure 7.8: TEG WHR modular unit, as the system size gets bigger TEG modules are added either (a) perpendicular to exhaust flow 'Column' or (b) in the direction of exhaust flow 'Rows'.

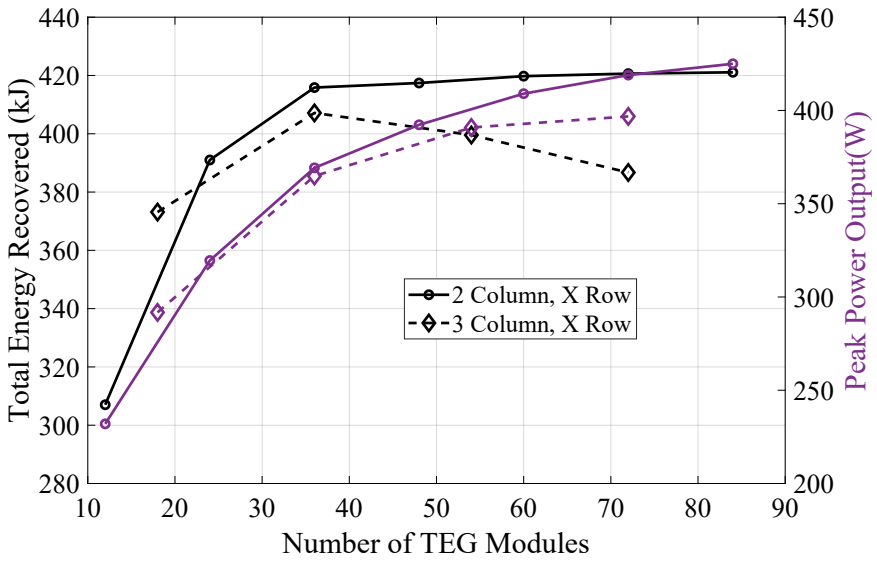

Figure 7.9: Total energy recovered and peak power output when the number of columns is fixed to 2 and 3 modular units, and the additional units are added only in the direction of exhaust flow.

The results for a case study when the number of Columns was fixed and only the number of Rows was increased is shown in Fig. 7.9. For the case when the number of Columns is fixed to two modular units, and the units keep increasing in the direction of exhaust flow, the total energy recovery reaches an asymptote around 36 TEG modules. The total energy recovered does not increase significantly if more TEG modules are added after this value. However, if the peak power output is observed on the second y-axis of Fig. 7.9, the power generated continues to increase as more TEG modules are added. Hence, if peak power output is used as the design metric, an 84 TEG module system would be designed rather than a 36 module system. For the case of 3 Columns, as more TEG rows are added, the total energy recovered decreases when the system changes from 36 TEG modules to 48 TEG modules due to axial conduction as explained previously.

Now, consider a system where the number of Rows is fixed and modular units

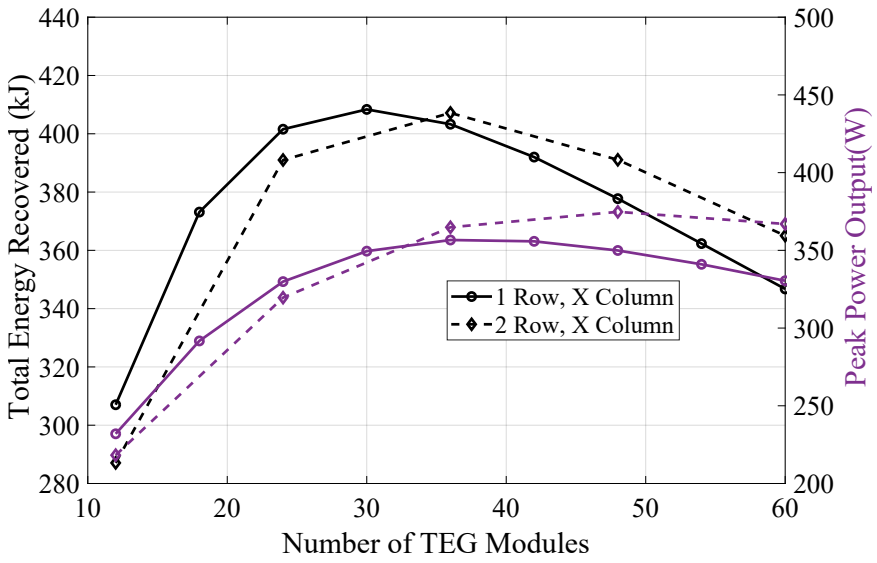

Figure 7.10: Total energy recovered over a US06 drive cycle vs. the total number of TEG modules in a system.

are added only in the perpendicular direction (to exhaust flow). The results for the total energy recovered and peak power output by the TEG WHR system is plotted in Fig. 7.10. For the case where the system has 1 Row and only the number of Columns varies, the total energy recovered decreases after 30 TEG modules. This reduction is observed since the TEG modules are added in the direction perpendicular to exhaust flow, hence less energy is available to each TEG module as more TEGs are added. The same reason explains why the peak power output is also reduced. Similar results are observed for the case where the system has two Rows and the number of Columns varies. Comparing the cases of 1 Row and 2 Row systems, the optimum number of TEG modules shifts as expected, but it is better to design the system with a single row due to axial conduction.

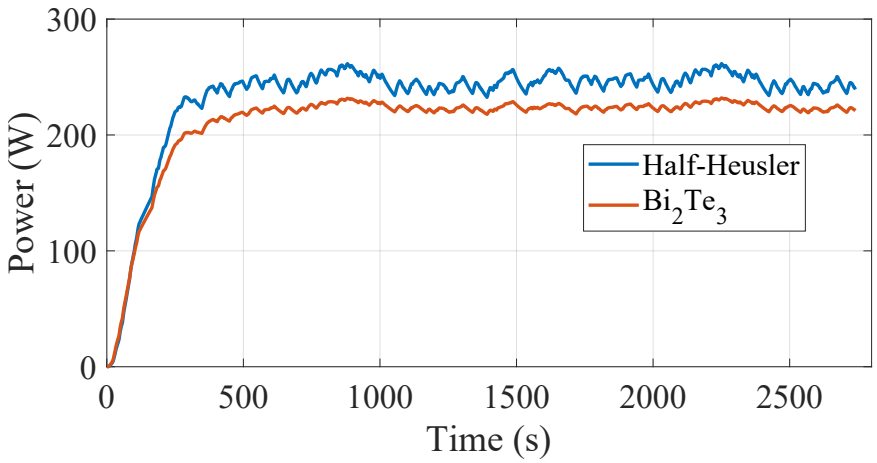

Figure 7.11: Power output comparison utilizing Half-Heusler modules vs. Bismuth Telluride modules over two drive cycles.

Finally, investigating different TEG materials is also performed through the validated transient model. The previous case studies showed the results with the minimum number of TEG modules being 12 because if fewer TEG modules were used, the maximum operating temperature would be exceeded. Half-Heulser material properties were used to simulate TEG modules that can operate at higher temperatures, hence 6 TEG modules can be simulated for the same city-type driving. The results for the power generated for 6 TEG modules over a UDDS drive cycle is shown in Fig. 7.11. As can be observed, the power output is increased when Half-Heusler TEG modules are used rather than Bismuth Telluride.

7.3 Electrical Connection Effects

Typically, in the literature all the TEG modules are connected electrically in series even in simulation when models are used to predict the power output of a bigger system. However, as has been shown in the previous section, as more modules are

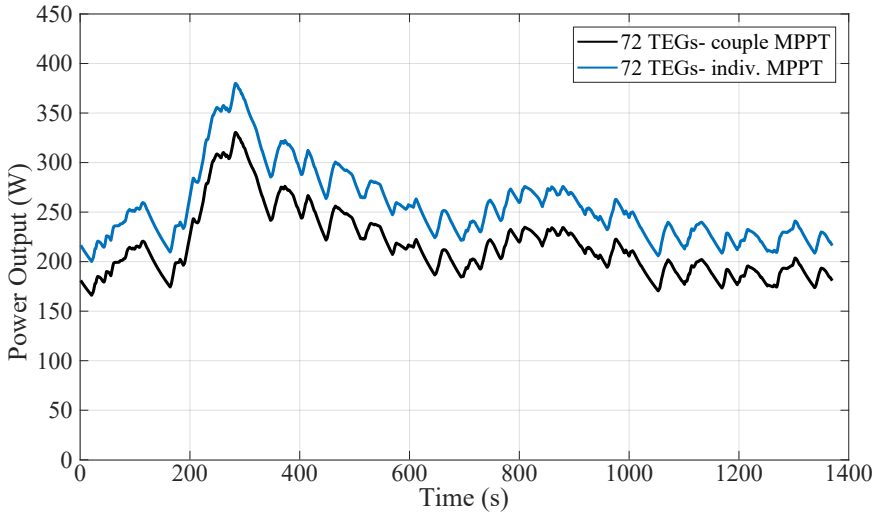

Figure 7.12: The power output for 72 TEGs consisting of 3 TEG rows with a single MPPT and each row containing its own MPPT.

added in the direction of exhaust flow, their performance will be degraded and the temperature difference across all the modules will not be uniform. Therefore, it is of interest to investigate the trade-off between implementing an individual MPPT per TEG Row (isotherm) versus the potential gain in energy recovered.

A 72 TEG module system, which consists of three Rows of TEGs in the direction of exhaust flow, is simulated. Each row operates with its own MPPT and is compared to a system which has only 1 MPPT for all 3 Rows. Figure 7.12 plots the power output over a UDDS cycle for the system with a single MPPT versus using 3 MPPTs. As can be observed from the plot, there is a power degradation when a single MPPT is used for all three Rows and considering the total energy recovered, there is a 10.7% reduction in energy recovered through the use of a single MPPT. When designing TEG WHR systems, the electrical configuration must be investigated to understand whether it is feasible to implement more than one MPPT for the entire system.

Chapter 8

Conclusion

Waste heat recovery in automotive applications has gained attention over the past decades since the efficiency from tank-to-wheel is only about 15% for vehicles with internal combustion engines. Since over 40% of the future vehicle fleet will continue to run on internal combustion engines, waste heat recovery technologies have been highly researched. Since thermoelectric generators are small solid state devices, they have been investigated as a potential solution to recovering thermal energy in the exhaust system of vehicles and converting it to electrical energy for use by the car's auxiliary system.

In the past, the performance metric for TEG waste heat recovery systems has been the maximum power produced. However, there has been a recent trend in observing the total energy recovered by the system rather than the instantaneous power produced. TEG operation in vehicles is a dynamic process where the energy available for recovery, which is governed by the exhaust gas temperature and mass flow rate, is highly dynamic during real driving scenarios. Therefore, this thesis developed a complete TEG WHR system model considering thermal capacitance in

the subcomponents to better understand the effect on power generation and total energy recovered by investigating the optimum system size from a dynamic point of view.

A design methodology was presented for designing a waste heat recovery system that maximized total energy recovered rather than peak power output. The maximum energy design point was shown to be different than the peak power design point and furthermore that larger TEG WHR systems exhibit a degradation in power generation due to axial conduction effects. An MPPT method was also proposed that achieved a tracking efficiency of 98% and was proven to be more accurate than the most-commonly-used tracking scheme implemented in the literature.

Bibliography

[1] U.S. Energy Information Administration, "International Energy Outlook 2017 Overview," U.S. Energy Information Administration, Tech. Rep. DOE/EIA-0484(2017), 2017.

[2] ——, "International Energy Outlook 2014," U.S. Energy Information Administration, Tech. Rep. DOE/EIA-0484(2014), 2014.

[3] ——, "Annual Energy Outlook 2018 with projections to 2050," U.S. Energy Information Administration, Tech. Rep., 2018.

[4] BNEF, "Electric vehicle outlook 2017," Bloomberg Finance, Tech. Rep. July, 2017.

[5] J. B. Heywood, *Internal Combustion Engine Fundamentals*. McGraw-Hill, 1988, vol. 21.

[6] Y.-Q. Zhang, Y.-T. Wu, G.-D. Xia, C.-F. Ma, W.-N. Ji, S.-W. Liu, K. Yang, and F.-B. Yang, "Development and experimental study on organic Rankine cycle system with single-screw expander for waste heat recovery from exhaust of diesel engine," *Energy*, vol. 77, pp. 499–508, dec 2014.

[7] T. Wang, Y. Zhang, Z. Peng, and G. Shu, "A review of researches on thermal exhaust heat recovery with Rankine cycle," *Renewable and Sustainable Energy Reviews*, vol. 15, no. 6, pp. 2862–2871, 2011.

[8] C. Sprouse and C. Depcik, "Review of organic Rankine cycles for internal combustion engine exhaust waste heat recovery," *Applied Thermal Engineering*, vol. 51, no. 1-2, pp. 711–722, mar 2013.

[9] A. a. Boretti, "Transient operation of internal combustion engines with Rankine waste heat recovery systems," *Applied Thermal Engineering*, vol. 48, pp. 18–23, dec 2012.

[10] B. Xu, D. Rathod, S. Kulkarni, A. Yebi, Z. Filipi, S. Onori, and M. Hoffman, "Transient dynamic modeling and validation of an organic Rankine cycle waste heat recovery system for heavy duty diesel engine applications," *Applied Energy*, vol. 205, pp. 260–279, 2017.

[11] R. Saidur, M. Rezaei, W. K. Muzammil, M. H. Hassan, S. Paria, and M. Hasanuzzaman, "Technologies to recover exhaust heat from internal combustion engines," *Renewable and Sustainable Energy Reviews*, vol. 16, pp. 5649–5659, 2012.

[12] Z. Petranović, M. Sjerić, I. Taritaš, M. Vujanović, and D. Kozarac, "Study of advanced engine operating strategies on a turbocharged diesel engine by using coupled numerical approaches," *Energy Conversion and Management*, vol. 171, pp. 1–11, 2018.

[13] A. J. Feneley, A. Pesiridis, and A. M. Andwari, "Variable Geometry Turbocharger Technologies for Exhaust Energy Recovery and Boosting-A Review," *Renewable and Sustainable Energy Reviews*, vol. 71, pp. 959–975, 2017.

[14] J. C. Conklin and J. P. Szybist, "A highly efficient six-stroke internal combustion engine cycle with water injection for in-cylinder exhaust heat recovery," *Energy*, vol. 35, no. 4, pp. 1658–1664, 2010.

[15] O. Kellogg-Smith, "Internal combustion and steam engine," U.S. Patent 4,143,518, 1979.

[16] G. J. Larsen, "Engine with a six-stroke cycle, variable compression ratio, and constant stroke," U.S. Patent 4,736,715, 1988.

[17] S. Singh, "computer controlled multi-stroke cycle power generating assembly and method of operation," U.S. Patent 7,021,272, 2006.

[18] B. H. Crower, "Method and apparatus for operating an internal combustion engine," U.S. Patent 2007/0 022 977, 2007.

[19] D. J. Lewis, J. D. Russel, and J. O. Michelini, "Valve selection for an engine operating in a multi-stroke cylinder mode," U.S. Patent 7,255,066, 2007.

[20] P. O. Jung, "High thermal efficiency six stroke internal combustion engine with heat recovery and water injection," U.S. Patent 2016/0 369 750, 2016.

[21] S. Yu, Q. Du, H. Diao, G. Shu, and K. Jiao, "Start-up modes of thermoelectric generator based on vehicle exhaust waste heat recovery," *Applied Energy*, vol. 138, pp. 276–290, Jan 2015.

[22] L. Chen, D. Cao, Y. Huang, and F. Z. Peng, "Modeling and power conditioning for thermoelectric generation," in *2008 IEEE Annual Power Electronics Specialists Conference*, Rhodes, Greece, June 2008, pp. 1098–1103.

[23] J. H. Meng, X. X. Zhang, and X. D. Wang, "Dynamic response characteristics of thermoelectric generator predicted by a three-dimensional heat-electricity coupled model," *Journal of Power Sources*, vol. 245, pp. 262–269, Jan. 2014.

[24] D. Rowe, *Modules, Systems, and Applications in Thermoelectrics*. CRC Press, 2012.

[25] A. F. Ioffe, *Semiconductor Thermoelements and Thermoelectric Cooling*. London: Infosearch Limited, 1957.

[26] N. Espinosa, M. Lazard, L. Aixala, and H. Scherrer, "Modeling a thermoelectric generator applied to diesel automotive heat recovery," *Journal of Electronic Materials*, vol. 39, no. 9, pp. 1446–1455, 2010.

[27] G. Liang, J. Zhou, and X. Huang, "Analytical model of parallel thermoelectric generator," *Applied Energy*, vol. 88, no. 12, pp. 5193–5199, 2011.

[28] X. Gou, S. Yang, H. Xiao, and Q. Ou, "A dynamic model for thermoelectric generator applied in waste heat recovery," *Energy*, vol. 52, pp. 201–209, April 2013.

[29] S. Kumar, S. D. Heister, X. Xu, J. R. Salvador, and G. P. Meisner, "Thermoelectric Generators for Automotive Waste Heat Recovery Systems Part I: Numerical Modeling and Baseline Model Analysis," *Journal of Electronic Materials*, vol. 42, no. 4, pp. 665–674, 2013.

[30] A. Montecucco, J. Siviter, and A. R. Knox, "Constant heat characterisation and geometrical optimisation of thermoelectric generators," *Applied Energy*, vol. 149, pp. 248–258, 2015.

[31] J. Chen, L. Zuo, Y. Wu, and J. Klein, "Modeling, experiments and optimization of an on-pipe thermoelectric generator," *Energy Conversion and Management*, vol. 122, pp. 298–309, 2016.

[32] G. Min, D. M. Rowe, and K. Kontostavlakis, "Thermoelectric figure-of-merit under large temperature differences," *Journal of Physics D: Applied Physics*, vol. 37, no. 8, pp. 1301–1304, 2004.

[33] M. Hamid Elsheikh, D. A. Shnawah, M. F. M. Sabri, S. B. M. Said, M. Haji Hassan, M. B. Ali Bashir, and M. Mohamad, "A review on thermoelectric renewable energy: Principle parameters that affect their performance," *Renewable and Sustainable Energy Reviews*, vol. 30, pp. 337–355, 2014.

[34] D. Rowe, *Thermoelectrics Handbook: Macro to Nano*. CRC Press, 2006.

[35] S. LeBlanc, "Thermoelectric generators: Linking material properties and systems engineering for waste heat recovery applications," *Sustainable Materials and Technologies*, vol. 1, pp. 26–35, Dec. 2014.

[36] S. W. Angrist, *Direct Energy Conversion*, 4th ed. Boston: Allyn and Bacon, Inc, 1982.

[37] International Energy Agency, "Global EV Outlook 2017: Two million and counting," International Energy Agency, Tech. Rep., 2017.

[38] N. Muralidhar, M. Himabindu, and R. V. Ravikrishna, "Modeling of a hybrid electric heavy duty vehicle to assess energy recovery using a thermoelectric generator," *Energy*, vol. 148, pp. 1046–1059, April 2018.

[39] A. Massaguer, E. Massaguer, M. Comamala, T. Pujol, L. Montoro, M. D. Cardenas, D. Carbonell, and A. J. Bueno, "Transient behavior under a normalized driving cycle of an automotive thermoelectric generator," *Applied Energy*, vol. 206, pp. 1282–1296, Nov. 2017.

[40] B. Li, K. Huang, Y. Yan, Y. Li, S. Twaha, and J. Zhu, "Heat transfer enhancement of a modularised thermoelectric power generator for passenger vehicles," *Applied Energy*, vol. 205, pp. 868–879, Nov. 2017.

[41] Y. Wang, C. Dai, and S. Wang, "Theoretical analysis of a thermoelectric generator using exhaust gas of vehicles as heat source," *Applied Energy*, vol. 112, pp. 1171–1180, Dec. 2013.

[42] Y. A. Cengel and M. A. Boles, *Thermodynamics: An Engineering Approach*, 5th ed. Boston: McGraw-Hill, 2006.

[43] F. P. Incropera, D. P. Dewitt, T. L. Bergman, and A. S. Lavine, *Fundamentals of Heat and Mass Transfer*, 6th ed. Hoboken, NJ: John Wiley & Sons, 2007.

[44] J. Lagrandeur, D. T. Crane, and B. Llc, "Vehicle Fuel Economy Improvement through Thermoelectric Waste Heat Recovery," in *DEER Conference*, Chicago, IL, August 2005.

[45] D. Crane, "Potential Thermoelectric Application in Diesel Engine," *9th Diesel Engine Emissions Reduction (DEER) Conference*, pp. 1–6, August 2003.

[46] M. Li, "Thermoelectric-Generator-Based DC-DC Conversion Network for Automotive Applications," Ph.D. dissertation, KTH, 2011.

[47] F. Charles, D. Ewing, J. Becard, J.-S. Chang, and J. Cotton, "Optimization of the exhaust mass flow rate and coolant temperature for Exhaust Gas Recirculation (EGR) cooling devices used in diesel engines," *SAE Technical Papers*, 2005.

[48] H. Wei, T. Zhu, G. Shu, L. Tan, and Y. Wang, "Gasoline engine exhaust gas recirculation - A review," *Applied Energy*, vol. 99, pp. 534–544, 2012.

[49] C. Brace, H. Burnham-Slipper, R. S. Wijetunge, N. D. Vaughan, K. Wright, and D. Blight, "Integrated Cooling Systems for Passenger Vehicles," *SAE Technical Paper*, 2001.

[50] D. T. Crane, "An introduction to system-level, steady-state and transient modeling and optimization of high-power-density thermoelectric generator devices made of segmented thermoelectric elements," *Journal of Electronic Materials*, vol. 40, no. 5, pp. 561–569, May 2011.

[51] T. A. Horst, W. Tegethoff, P. Eilts, and J. Koehler, "Prediction of dynamic Rankine Cycle waste heat recovery performance and fuel saving potential in passenger car applications considering interactions with vehicles' energy management," *Energy Conversion and Management*, vol. 78, pp. 438–451, Feb. 2014.

[52] K. Matsubara, "Development of a high efficient thermoelectric stack for a waste exhaust heat recovery of vehicles," in *Thermoelectrics, 2002. Proceedings ICT*

'02. Twenty-First International Conference on, Long Beach, CA, August 2002, pp. 418–423.

[53] D. Crane and J. Lagrandeur, "Automotive Waste Heat Conversion to Power Program- 2011 Vehicle Technologies Program Annual Merit Review," pp. 1–23, 2011.

[54] K. Biswas, J. He, I. D. Blum, C. I. Wu, T. P. Hogan, D. N. Seidman, V. P. Dravid, and M. G. Kanatzidis, "High-performance bulk thermoelectrics with all-scale hierarchical architectures," *Nature*, vol. 489, no. 7416, pp. 414–418, Sept 2012.

[55] A. U. Khan, K. Kobayashi, D. M. Tang, Y. Yamauchi, K. Hasegawa, M. Mitome, Y. Xue, B. Jiang, K. Tsuchiya, D. Golberg, Y. Bando, and T. Mori, "Nano-micro-porous skutterudites with 100% enhancement in ZT for high performance thermoelectricity," *Nano Energy*, vol. 31, no. July 2016, pp. 152–159, Jan. 2017.

[56] C. Fu, S. Bai, Y. Liu, Y. Tang, L. Chen, X. Zhao, and T. Zhu, "Realizing high figure of merit in heavy-band p-type half-Heusler thermoelectric materials," *Nature Communications*, vol. 6, pp. 1–7, Sept. 2015.

[57] W. Wei, C. Chang, T. Yang, J. Liu, H. Tang, J. Zhang, Y. Li, F. Xu, Z. Zhang, J. F. Li, and G. Tang, "Achieving High Thermoelectric Figure of Merit in Polycrystalline SnSe via Introducing Sn Vacancies," *Journal of the American Chemical Society*, vol. 140, no. 1, pp. 499–505, Jan. 2018.

[58] J. LaGrandeur, D. Crane, S. Hung, B. Mazar, and A. Eder, "Automotive waste heat conversion to electric power using skutterudite, tags, pbte and bite," in

2006 25th International Conference on Thermoelectrics, Vienna, Austria, Aug 2006, pp. 343–348.

[59] Y. Zhang, M. Cleary, X. Wang, N. Kempf, L. Schoensee, J. Yang, G. Joshi, and L. Meda, "High-temperature and high-power-density nanostructured thermoelectric generator for automotive waste heat recovery," *Energy Conversion and Management*, vol. 105, pp. 946–950, Sept. 2015.

[60] J. Lagrandeur and D. Crane, "Scientific and Technical Information (STI) for Financial Assistance and Non-M&O/M&l," Amerigon, Tech. Rep., 2012.

[61] G. Min and D. M. Rowe, "Ring-structured thermoelectric module," *Semiconductor Science and Technology*, vol. 22, no. 8, pp. 880–883, June 2007.

[62] A. Bauknecht, T. Steinert, C. Spengler, and G. Suck, "Analysis of annular thermoelectric couples with nonuniform temperature distribution by means of 3-D multiphysics simulation," *Journal of Electronic Materials*, vol. 42, no. 7, pp. 1641–1646, July 2013.

[63] A. Schmitz, C. Stiewe, and E. Müller, "Preparation of ring-shaped thermoelectric legs from PbTe powders for tubular thermoelectric modules," *Journal of Electronic Materials*, vol. 42, no. 7, pp. 1702–1706, July 2013.

[64] C. Hadjistassou, E. Kyriakides, and J. Georgiou, "Designing high efficiency segmented thermoelectric generators," *Energy Conversion and Management*, vol. 66, pp. 165–172, Feb. 2013.

[65] T. Ming, Y. Wu, C. Peng, and Y. Tao, "Thermal analysis on a segmented thermoelectric generator," *Energy*, vol. 80, pp. 388–399, Feb. 2015.

[66] D. T. Crane and L. E. Bell, "Progress Towards Maximizing the Performance of a Thermoelectric Power Generator," in *2006 25th International Conference on Thermoelectrics*, Vienna, Austria, Aug. 2006, pp. 11–16.

[67] M. Freunek, M. Müller, T. Ungan, W. Walker, and L. M. Reindl, "New physical model for thermoelectric generators," *Journal of Electronic Materials*, vol. 38, no. 7, pp. 1214–1220, July 2009.

[68] F. J. Lesage, É. V. Sempels, and N. Lalande-Bertrand, "A study on heat transfer enhancement using flow channel inserts for thermoelectric power generation," *Energy Conversion and Management*, vol. 75, pp. 532–541, Nov. 2013.

[69] J. Pandit, M. Thompson, S. V. Ekkad, and S. T. Huxtable, "Effect of pin fin to channel height ratio and pin fin geometry on heat transfer performance for flow in rectangular channels," *International Journal of Heat and Mass Transfer*, vol. 77, pp. 359–368, Oct. 2014.

[70] X. Liu, Y. Deng, K. , M. Xu, Y. Xu, and C. Su, "Experiments and simulations on heat exchangers in thermoelectric generator for automotive application," *Applied Thermal Engineering*, vol. 71, no. 1, pp. 364–370, Oct. 2014.

[71] Z. Niu, H. Diao, S. Yu, K. Jiao, Q. Du, and G. Shu, "Investigation and design optimization of exhaust-based thermoelectric generator system for internal combustion engine," *Energy Conversion and Management*, vol. 85, pp. 85–101, Sept. 2014.

[72] X. Wang and Y. Deng, "Research on and Thermal Performance of the Heat Exchanger in Automotive Exhaust- Based Thermoelectric Generator," *SAE Technical Paper*, pp. 1–9, 2014.

[73] Y. Wang, S. Li, Y. Zhang, X. Yang, Y. Deng, and C. Su, "The influence of inner topology of exhaust heat exchanger and thermoelectric module distribution on the performance of automotive thermoelectric generator," *Energy Conversion and Management*, vol. 126, pp. 266–277, Oct. 2016.

[74] X. Liu, Y. Deng, S. Chen, W. Wang, Y. Xu, and C. Su, "A case study on compatibility of automotive exhaust thermoelectric generation system, catalytic converter and muffler," *Case Studies in Thermal Engineering*, vol. 2, pp. 62–66, March 2014.

[75] T. Ma, X. Lu, J. Pandit, S. V. Ekkad, S. T. Huxtable, S. Deshpande, and Q. wang Wang, "Numerical study on thermoelectric-hydraulic performance of a thermoelectric power generator with a plate-fin heat exchanger with longitudinal vortex generators," *Applied Energy*, vol. 185, pp. 1343–1354, Jan. 2017.

[76] T. Wang, W. Wang, W. Luan, and S.-t. Tu, "Waste heat recovery through plate heat exchanger based thermoelectric generator system," *Applied Energy*, vol. 136, pp. 860–865, Dec. 2014.

[77] T. J. Hendricks, "Integrated Thermoelectric-Thermal System Resistance Optimization to Maximize Power Output in Thermoelectirc Energy Recovery Systems," in *Materials Research Society Symposium*, vol. 1642, May 2014.

[78] K. Oetringer, "Upgrading Hybrid-Vehicles with a Thermoelectric Generator," in *2014 Ninth International Conference on Ecological Vehicles and Renewable Energies (EVER)*, Monte-Carlo, Monaco, March 2014, pp. 1–5.

[79] A. Montecucco, J. Siviter, and A. R. Knox, "The effect of temperature mismatch on thermoelectric generators electrically connected in series and parallel," *Applied Energy*, vol. 123, pp. 47–54, June 2014.

[80] S. Wang, T. Xie, and H. Xie, "Experimental study of the effects of the thermal contact resistance on the performance of thermoelectric generator," *Applied Thermal Engineering*, vol. 130, pp. 847–853, Feb. 2018.

[81] U. Birkholz, E. Grob, U. Stohrer, and K. Voss, "Conversion of waste exhaust heat in automobiles using FeSi2 thermoelements," in *Proceedings of the 7th International Conference on Thermoelectric Energy Conversion*, Arlington, VA, 1988, pp. 124–128.

[82] A. Eder and M. Linde, "Efficient and Dynamic – The BMW Group Roadmap for the Application of Thermoelectric Generators." pp. 1–23, 2011.

[83] G. P. Meisner, "Skutterudite Thermoelectric Generator For Automotive Waste Heat Recovery," Baltimore, MD, pp. 1–19, 2012.

[84] M. Mori, T. Yamagami, M. Sorazawa, T. Miyabe, S. Takahashi, and T. Haraguchi, "Simulation of fuel economy effectiveness of exhaust heat recovery system using thermoelectric generator in a series hybrid," *SAE International Journal of Materials and Manufacturing*, vol. 4, no. 1, pp. 1268–1276, 2011.

[85] T. Y. Kim, J. Kwak, and B.-w. Kim, "Energy harvesting performance of hexagonal shaped thermoelectric generator for passenger vehicle applications: An experimental approach," *Energy Conversion and Management*, vol. 160, pp. 14–21, March 2018.

[86] V. G. Jovovic, "U.S. Department of Energy Scientific and Technical Information (STI) for Financial Assistance and Non-M&O/M&I Project Title:Thermoelectric Waste Heat Recovery Program for Passenger Vehicles," Gentherm LLC, Tech. Rep., 2016.

[87] J. C. Bass, N. B. Elsner, and F. A. Leavitt, "Performance of the 1 kW thermoelectric generator for diesel engines," in *Proceedings of the 13th International Conference on Thermoelectrics*, vol. 316, Kansas City, MO, 1995, pp. 295–298.

[88] K. Ikoma, M. Munekiyo, K. Furuya, M. Kobayashi, T. Izumi, and K. Shinohara, "Thermoelectric module and generator for gasoline engine vehicles," in *Seventeenth International Conference on Thermoelectrics*, Ngoya, Japan, May 1998, pp. 464–467.

[89] E. F. Thacher, B. T. Helenbrook, M. a. Karri, and C. J. Richter, "Testing of an automobile exhaust thermoelectric generator in a light truck," *Proceedings of the Institution of Mechanical Engineers, Part D: Journal of Automobile Engineering*, vol. 221, pp. 95–107, Jan 2007.

[90] S. Kim, S. Park, S. Kim, and S. H. Rhi, "A thermoelectric generator using engine coolant for light-duty internal combustion Engine-Powered Vehicles," *Journal of Electronic Materials*, vol. 40, no. 5, pp. 812–816, May 2011.

[91] X. Liu, Y. D. Deng, Z. Li, and C. Q. Su, "Performance analysis of a waste heat recovery thermoelectric generation system for automotive application," *Energy Conversion and Management*, vol. 90, pp. 121–127, 2015.

[92] T. Y. Kim, A. A. Negash, and G. Cho, "Waste heat recovery of a diesel engine using a thermoelectric generator equipped with customized thermoelectric modules," *Energy Conversion and Management*, vol. 124, pp. 280–286, Sept. 2016.

[93] X. Zhou, Y. Yan, X. Lu, H. Zhu, X. Han, G. Chen, and Z. Ren, "Routes for high-performance thermoelectric materials," *Materials Today*, pp. 1–15, April 2018.

[94] L.-D. Zhao, S.-H. Lo, Y. Zhang, H. Sun, G. Tan, C. Uher, C. Wolverton, V. P. Dravid, and M. G. Kanatzidis, "Ultralow thermal conductivity and high thermoelectric figure of merit in SnSe crystals," *Nature*, vol. 508, no. 7496, pp. 373–377, April 2014.

[95] R. Stobart and Z. Yang, "The Development of Skutterudite-Based Thermoelectric Generators for Vehicles," *SAE Technical Papers*, pp. 1–10, 2018.

[96] J. Szybist, S. Davis, J. Thomas, and B. Kaul, "Performance of a Half-Heusler Thermoelectric Generator for Automotive Application," *SAE Technical Papers*, pp. 1–9, 2018.

[97] Q. Zhang, J. Liao, Y. Tang, M. Gu, C. Ming, P. Qiu, S. Bai, X. Shi, C. Uher, and L. Chen, "Realizing a thermoelectric conversion efficiency of 12% in bismuth telluride/skutterudite segmented modules through full-parameter optimization

and energy-loss minimized integration," *Energy Environ. Sci.*, vol. 10, no. 4, pp. 956–963, April 2017.

[98] Q. H. Zhang, X. Y. Huang, S. Q. Bai, X. Shi, C. Uher, and L. D. Chen, "Thermoelectric Devices for Power Generation: Recent Progress and Future Challenges," *Advanced Engineering Materials*, vol. 18, no. 2, pp. 194–213, Feb. 2016.

[99] L. Yang, Z. G. Chen, M. S. Dargusch, and J. Zou, "High Performance Thermoelectric Materials: Progress and Their Applications," *Advanced Energy Materials*, vol. 8, no. 6, pp. 1–28, Feb. 2018.

[100] F. Kim, B. Kwon, Y. Eom, J. E. Lee, S. Park, S. Jo, S. H. Park, B. S. Kim, H. J. Im, M. H. Lee, T. S. Min, K. T. Kim, H. G. Chae, W. P. King, and J. S. Son, "3D printing of shape-conformable thermoelectric materials using all-inorganic Bi2Te3-based inks," *Nature Energy*, vol. 3, no. 4, pp. 301–309, 2018.

[101] Q. Cao, W. Luan, and T. Wang, "Performance enhancement of heat pipes assisted thermoelectric generator for automobile exhaust heat recovery," *Applied Thermal Engineering*, vol. 130, pp. 1472–1479, Feb. 2018.

[102] S. Lv, W. He, Q. Jiang, Z. Hu, X. Liu, H. Chen, and M. Liu, "Study of different heat exchange technologies influence on the performance of thermoelectric generators," *Energy Conversion and Management*, vol. 156, pp. 167–177, Jan. 2018.

[103] S. Lan, Z. Yang, R. Chen, and R. Stobart, "A dynamic model for thermoelectric generator applied to vehicle waste heat recovery," *Applied Energy*, vol. 210, pp. 327–338, 2018.

[104] T. Y. Kim and J. Kim, "Assessment of the energy recovery potential of a thermoelectric generator system for passenger vehicles under various drive cycles," *Energy*, vol. 143, pp. 363–371, Jan. 2018.

[105] A. Massaguer, E. Massaguer, M. Comamala, T. Pujol, J. R. González, M. D. Cardenas, D. Carbonell, and A. J. Bueno, "A method to assess the fuel economy of automotive thermoelectric generators," *Applied Energy*, vol. 222, pp. 42–58, July 2018.

[106] Z. Yang, R. Stobart, S. Lan, B. Mason, and W. Edward, "Towards Optimal Performance of a Thermoelectric Generator for Exhaust Waste Heat Recovery from an Automotive Engine," *SAE Technical Paper*, pp. 1–8, 2018.

[107] Y. D. Deng, T. Hu, C. Q. Su, and X. H. Yuan, "Fuel Economy Improvement by Utilizing Thermoelectric Generator in Heavy-Duty Vehicle," *Journal of Electronic Materials*, vol. 46, no. 5, pp. 3227–3234, May 2017.

[108] A. Z. Sahin and B. S. Yilbas, "The thermoelement as thermoelectric power generator: Effect of leg geometry on the efficiency and power generation," *Energy Conversion and Management*, vol. 65, pp. 26–32, Jan. 2013.

[109] J.-h. Meng, X.-x. Zhang, and X.-d. Wang, "Multi-objective and multi-parameter optimization of a thermoelectric generator module," *Energy*, vol. 71, pp. 367–376, July 2014.

[110] X. Liang, X. Sun, H. Tian, G. Shu, Y. Wang, and X. Wang, "Comparison and parameter optimization of a two-stage thermoelectric generator using high temperature exhaust of internal combustion engine," *Applied Energy*, vol. 130, pp. 190–199, Oct. 2014.

[111] C. Wu, "Analysis of waste-heat thermoelectric power generators," *Applied Thermal Engineering*, vol. 16, no. 1, pp. 63–69, Jan. 1996.

[112] Y. Hsiao, W. Chang, and S. Chen, "A mathematic model of thermoelectric module with applications on waste heat recovery from automobile engine," *Energy*, vol. 35, no. 3, pp. 1447–1454, March 2010.

[113] S. Vale, L. Heber, P. Coelho, and C. Silva, "Parametric study of a thermoelectric generator system for exhaust gas energy recovery in diesel road freight transportation," *Energy Conversion and Management*, vol. 133, pp. 167–177, Feb. 2017.

[114] R. J. Stevens, S. J. Weinstein, and K. S. Koppula, "Theoretical limits of thermoelectric power generation from exhaust gases," *Applied Energy*, vol. 133, pp. 80–88, Nov. 2014.

[115] E. Massaguer, A. Massaguer, L. Montoro, and J. R. Gonzalez, "Modeling analysis of longitudinal thermoelectric energy harvester in low temperature waste heat recovery applications," *Applied Energy*, vol. 140, pp. 184–195, Feb. 2015.

[116] W. He, S. Wang, Y. Zhao, and Y. Li, "Effects of heat transfer characteristics between fluid channels and thermoelectric modules on optimal thermoelectric performance," *Energy Conversion and Management*, vol. 113, pp. 201–208, April

2016.

[117] Q. E. Hussain, D. R. Brigham, and C. W. Maranville, "Thermoelectric Exhaust Heat Recovery for Hybrid Vehicles," *SAE International Journal of Engines*, vol. 2, no. 1, pp. 1132–1142, 2009.

[118] J. Girard, "The investigation of exhaust control strategies and waste heat recovery practices of naturally-ventilated exhaust streams," Master's thesis, McMaster University, 2016.

[119] S. Kakac, R. K. Shah, and W. Aung, *Handbook of Single-Phase Convective Heat Transfer*. Wiley-Interscience, 1987.

[120] Y. Hana, "A characterization Of flat-plate heat exchangers for thermal load management of thermoelectric generators," Master's thesis, McMaster University, 2014.

[121] H. Nagayoshi, K. Tokumisu, and T. Kajikawa, "Evaluation of multi MPPT thermoelectric generator system," in *2007 26th International Conference on Thermoelectrics*, Jeju Island, South Korea, 2007, pp. 318–321.

[122] C. Yu and K. Chau, "Thermoelectric automotive waste heat energy recovery using maximum power point tracking," *Energy Conversion and Management*, vol. 50, no. 6, pp. 1506–1512, jun 2009.

[123] H. Mamur and R. Ahiska, "Application of a DC - DC boost converter with maximum power point tracking for low power thermoelectric generators," *Energy Conversion and Management*, vol. 97, pp. 265–272, 2015.

[124] J. Park and S. Kim, "Maximum power point tracking controller for thermoelectric generators with peak gain control of boost DC-DC converters," *Journal of Electronic Materials*, vol. 41, no. 6, pp. 1242–1246, 2012.

[125] F. Liu, S. Duan, F. Liu, B. Liu, and Y. Kang, "A Variable Step Size INC MPPT Method for PV Systems," *IEEE Transactions on Industrial Electronics*, vol. 55, no. 7, pp. 2622–2628, 2008.

[126] R. Y. Kim and J. S. Lai, "Optimal design of adaptive maximum-power-point tracking algorithm for thermoelectric based battery energy storage system," in *2008 34th Annual Conference of IEEE Industrial Electronics*, Orlando, Fl, 2008, pp. 861–866.

[127] R.-Y. Kim, J.-S. Lai, B. York, and A. Koran, "Analysis and Design of Maximum Power Point Tracking Scheme for Thermoelectric Battery Energy Storage System," *IEEE Transactions on Industrial Electronics*, vol. 56, no. 9, pp. 3709–3716, 2009.

[128] H. Wu, K. Sun, M. Chen, and Y. Xing, "Evaluation of Power Conditioning Architectures for Energy Production Enhancement in Thermoelectric Generator Systems," *Journal of Electronic Materials*, vol. 43, no. 6, pp. 1567–1573, 2014.

[129] H. Yamada, K. Kimura, T. Hanamoto, T. Ishiyama, T. Sakaguchi, and T. Takahashi, "A MPPT Control Method of Thermoelectric Power Generation with Single Sensor," in *2013 IEEE 10th International Conference on Power Electronics and Drive Systems (PEDS)*, Kitakyushu, Japan, 2013, pp. 545–558.

[130] I. Laird and D. D. C. Lu, "High step-up DC/DC topology and MPPT algorithm for use with a thermoelectric generator," *IEEE Transactions on Power Electronics*, vol. 28, no. 7, pp. 3147–3157, 2013.

[131] R.-Y. Kim and J.-S. Lai, "A Seamless Mode Transfer Maximum Power Point Tracking Controller For Thermoelectric Generator Applications," *IEEE Transactions on Power Electronics*, vol. 23, no. 5, pp. 2310–2318, 2008.

[132] ——, "Aggregated modeling and control of a boost-buck cascade converter for maximum power point tracking of a thermoelectric generator," in *2008 Twenty-Third Annual IEEE Applied Power Electronics Conference and Exposition*, Austin, TX, Feb. 2008, pp. 1754–1760.

[133] H. Yamada, K. Kimura, T. Hanamoto, T. Ishiyama, T. Sakaguchi, and T. Takahashi, "A novel MPPT control method of thermoelectric power generation using state space averaging method," in *2011 IEEE Ninth International Conference on Power Electronics and Drive Systems*, Singapore, 2011, pp. 895–900.

[134] A. Hidaka, T. Tsuji, and S. Matsumoto, "A thermoelectric power generation system with ultra low input voltage boost converter with maximum power point tracking," in *2012 International Conference on Renewable Energy Research and Applications (ICRERA)*, Nagasaki, Japan, 2012, pp. 1–5.

[135] N. Kimura, "Dc-dc converter current measurement by using fet on-state resistance for low-cost maximum power point tracking," in *2013 IEEE 14th Workshop on Control and Modeling for Power Electronics (COMPEL)*, Salt Lake City, UT, June 2013, pp. 1–5.

[136] C. Vadstrup, E. Schaltz, and M. Chen, "Individual module maximum power point tracking for thermoelectric generator systems," *Journal of Electronic Materials*, vol. 42, no. 7, pp. 2203–2208, July 2013.

[137] J.-D. Park, H. Lee, and M. Bond, "Uninterrupted thermoelectric energy harvesting using temperature-sensor-based maximum power point tracking system," *Energy Conversion and Management*, vol. 86, pp. 233–240, 2014.

[138] A. Paraskevas and E. Koutroulis, "A simple maximum power point tracker for thermoelectric generators," *Energy Conversion and Management*, vol. 108, pp. 355–365, 2016.

[139] S. Yu, Q. Du, H. Diao, G. Shu, and K. Jiao, "Effect of vehicle driving conditions on the performance of thermoelectric generator," *Energy Conversion and Management*, vol. 96, pp. 363–376, 2015.

[140] R. Rodriguez, M. Preindl, A. Emadi, and J. Cotton, "Maximum Power Point Tracking for Thermoelectric Generators with High Frequency Injection," in *41st Annual Conference of the IEEE Industrial Electronics Society IECON15*, Yokohama, Japan, 2015, pp. 004 127–004 132.

[141] Daniel W.Hart, *Power Electronics*. McGrawHill, 2011.

[142] F. A. Aashoor and F. V. Robinson, "A variable step size perturb and observe algorithm for photovoltaic maximum power point tracking," in *2012 47th International Universities Power Engineering Conference (UPEC)*, London, UK, 2012, pp. 1–6.

[143] A. Montecucco, S. Member, A. R. Knox, and S. Member, "Maximum Power Point Tracking Converter Based on the Open-Circuit Voltage Method for Thermoelectric Generators," *IEEE Transactions on Power Electronics*, vol. 30, no. 2, pp. 1–12, 2015.

[144] I. Laird, H. Lovatt, N. Savvides, D. Lu, and V. Agelidis, "Comparative study of maximum power point tracking algorithms for thermoelectric generators," in *2008 Australasian Universities Power Engineering Conference*, Sydney, Australia, 2008, pp. 1–6.

[145] M. Bond and J. D. Park, "Current-sensorless power estimation and MPPT implementation for thermoelectric generators," *IEEE Transactions on Industrial Electronics*, vol. 62, no. 9, pp. 5539–5548, 2015.

[146] T. Markel, A. Brooker, T. Hendricks, V. Johnson, K. Kelly, B. Kramer, M. O'Keefe, S. Sprik, and K. Wipke, "ADVISOR: a systems analysis tool for advanced vehicle modeling," *Journal of Power Sources*, vol. 110, no. 2, pp. 255–266, 2002.

[147] E. Massaguer, A. Massaguer, L. Montoro, and J. R. Gonzalez, "Development and validation of a new TRNSYS type for the simulation of thermoelectric generators," *Applied Energy*, vol. 42, pp. 1004–1009, 2014.